Theses and Dissertations   Graduate School

2018

Heteroatom doped porous carbon for alternative energy conversion and storage systems

Fatema A. Choudhury

Heteroatom doped porous carbon for alternative energy conversion and storage systems

A dissertation submitted in partial fulfillment of the requirements for the degree of Doctor of Philosophy in Chemistry at Virginia Commonwealth University.

by

Fatema Akthar Choudhury

Bachelor of Science, Shahjalal University of Science and Technology, 2011

Director: Dr. Hani M. El-Kaderi

Associate Professor, Department of Chemistry

Virginia Commonwealth University

Richmond, Virginia

August 2018

I

Acknowledgement

First and foremost, I am grateful for all the blessings that Allah, the Almighty has bestowed upon me. Next, I would like to express my gratitude to my advisor, Dr. Hani M. El-Kaderi. It has been a privilege to receive his precious ideas, relentless guidance and continuous support throughout these last four years. Without his endless help and encouragement, this thesis would not be possible. I will always remain grateful for all the efforts he has made for my personal development as a researcher and will cherish the experiences gained in his research group. I would also like to appreciate the helpful comments and contribution from my committee members, Dr. Julio Alvarez, Dr. Indika U. Arachchige and Dr. Ram B. Gupta. I am very thankful to Dr. Dmitry Pestov, Dr. Carlos E Castano Londono and Dr. Joseph Turner for the training on different characterization instruments. Special thanks to Dr. Oussama El-Kadri. I learnt a lot from the discussions I had with him during his visit to VCU.

I would also like to thank the Chemistry Department of VCU for giving me the opportunity to be a teaching assistant which provided me the teaching skills and improved my self-confidence. I felt privileged to take courses under highly intellectual VCU faculties. I would always remember VCU particularly Chemistry Department and it definitely held a very special place in my heart.

I am thankful to all my previous and current colleagues in the lab, Ravi Kumar Arvapally, Zafer Kahveci, Timur Islamoglu, Pezhman Arab, Babak Ashourirad, Tsemre-Dengil Mesfin Tessema, Yomna Hosameldin Abdelmoaty, Nazgol Norouzi, Kumari Shamara Weeraratne, Ahmed Abdelkader, Michael Anhorn, Omniya Alomainy and Ahmed Alzharani for their continuous help and support with experiments and moral boosts. Special thanks to Dr. Yomna, Dr. Tsemre, Shamara and Nazgol for encouraging and helping me as a friend. It has been a pleasure to work with all of you.

Dedication

This work is dedicated to my mother, Latifa Akthar Choudhury (Ruby) for her unconditional love and all the sacrifices.

Abstract

HETEROATOM DOPED POROUS CARBON FOR ALTERNATIVE

ENERGY STORAGE AND CONVERSION SYSTEMS

By Fatema Akthar Choudhury, Ph.D.

A dissertation submitted in partial fulfillment of the requirements for the degree of
Doctor of Philosophy at Virginia Commonwealth University.

Virginia Commonwealth University, 2018.

Director: Dr. Hani M El-Kaderi
Associate Professor, Department of Chemistry

The electrocatalysis of oxygen plays a significant role in several electrochemical energy storage and conversion systems including metal−air batteries, fuel cells, electrocatalytic and photocatalytic water splitting. The sluggish kinetics and complex reaction mechanism of this cathodic oxygen reduction reaction (ORR) affect the performance and practical application of

such renewable energy technologies. To address this limiting factor, a suitable electrocatalyst is required for ORR. In general, platinum or highly dispersed Pt-based nanoparticles on carbon black are considered as the best ORR catalyst. But platinum being very scarce and expensive tends to increase the cost. Moreover, platinum-based catalysts are prone to several serious problems, including declining activity, the fuel-crossover, and poisoning effects. This has initiated overwhelming research attention towards the development of low cost ORR catalysts. Jasinski *et al.* pioneered in reporting that a N_4-chelate complex with a transition metal could be used for electrochemical oxygen reduction. Subsequently many nonprecious ORR catalysts have been investigated so far to replace platinum which include transition metal chalcogenides, nitrogen-doped carbon nanotubes or graphene, carbon nitride, and metal-N_4 chelate macrocycles (M-N_4-macrocycles). However, most of these current catalysts exhibited insufficient activity and low stability in corrosive environment of fuel cells. Thus, new strategies to develop catalysts which can meet the combined requirements of low cost, high catalytic activity and long-term durability still remains a challenge.

Recently our group has reported synthesis of heteroatom doped porous carbon through chemical activation of simple monomers. The facile synthetic route, high surface areas with abundant micropores, inherent presence of heteroatoms and tunable structure/composition at the molecular level make them potential for high-performance ORR electrocatalysts. To increase the catalytic performance in both acidic and basic media, it is important to incorporate or coordinate the doped heteroatom centers with 3d transition metals such as iron or cobalt. Herein, two different synthetic strategies will be presented to synthesize transition metal-based heteroatom doped porous carbon as ORR catalyst. In the first approach, iron (III) thiocyanate as iron salts was pyrolyzed with benzimidazole to introduce sulfur along with nitrogen and iron in the porous carbon. Another synthetic approach involved hydrothermal synthesis of cobalt oxide on the surface of benzimidazole derived porous carbon. ORR can proceed via either one

step four-electron reduction pathway producing water or two step two-electron reduction pathway producing HO_2^-, OH^- and H_2O_2. Both of these synthesized catalysts favored $4e^-$ reduction pathway which is energetically efficient and do not produce corrosive byproducts. The electrochemical performance of the synthesized catalyst will be analyzed by cyclic voltammetry, linear sweep voltammetry and amperometric i-t technique and compared with commercially available 20 wt% Pt based carbon in both acidic and basic media. The effect of pore size, nitrogen content, bonding configurations of nitrogen and sulfur, influence of cobalt and iron on ORR performance will also be discussed.

Table of Contents

Chapter 2

Study of oxygen reduction reaction **40**

Chapter 3

Rapid Synthesis of Fe Based S and N dual doped Benzimidazole derived Porous Carbon for Efficient Electrocatalytic Oxygen Reduction Reaction... **73**

Chapter 4

Co₃O₄ deposited N doped Benzimidazole derived Porous Carbon for Electrocatalysis of

Oxygen Reduction Reaction... 116

Chapter 5

Chapter 1

Introduction

1.1 Fuel Cells

Fuel cells are considered as the most promising solution for clean sustainable energy. They can be widely used in transportation, material handling, stationary, portable, and emergency backup power applications. They have outstanding advantages over conventional combustion-based technologies in energy conversion efficiencies. In addition, they are environmental friendly with lower pollutant gas emissions and generate less sound as they have fewer moving parts compared to thermal engines. They also work better than batteries as they do not require charging and can continuously produce energy as long as fuel is supplied. A fuel cell usually consists of two electrodes (anode and cathode) sandwiched around an electrolyte and fuel supplied to the anode are oxidized and the electron released go through an external circuit, creating a flow of electricity. Meanwhile, protons generated from the oxidation of the fuel migrate to the cathode via electrolyte and reduce the air (oxygen) fed at the cathode.
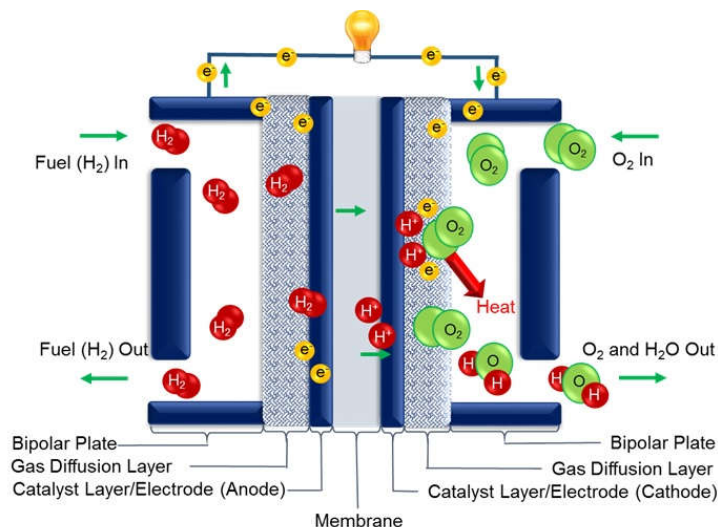
Figure 1.1: Typical fuel cell

At the cathode:

$$O_2 + 4H^+ + 4e^- \rightarrow 2H_2O$$
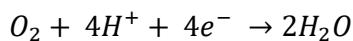
At the anode if the fuel is hydrogen:

$$2H_2 \rightarrow 4H^+ + 4e^-$$

Net reaction:

$$O_2 + 2H_2 \rightarrow 2H_2O$$
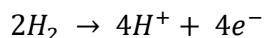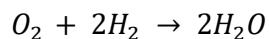
If the fuel is methanol, at the anode:

$$CH_3OH + 6OH^- \rightarrow 5H_2O + 6e^- + CO_2$$

At the cathode:

$$\frac{3}{2}O_2 + 3H_2O + 6e^- \rightarrow 6OH^-$$

Net Reaction:

$$CH_3OH + \frac{3}{2}O_2 \rightarrow 2H_2O + CO_2$$
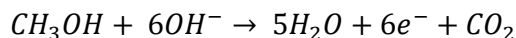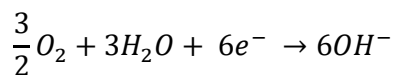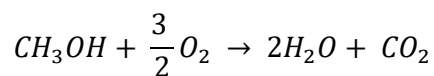
Both oxidation and reduction processes that occur in fuel cells require a suitable catalyst in order to deliver desirable performance. Typically, highly dispersed Pt-based nanoparticles on carbon black are used as catalyst to promote the rate of oxygen reduction reaction (ORR) and fuel oxidation reaction in respective electrodes. In case of the oxidation of fuel, the reaction kinetics is extremely fast and requires much less Pt loading at the anode which is approximately ~0.05 mg/cm². However, at the cathode ORR has sluggish reaction kinetics and requires at least eight times more catalyst loading than that of anode. Hence it is essential to develop a suitable electrocatalyst for ORR.

1.2 Role of platinum catalyst in proton exchange membrane fuel cells

1.2.1 Catalytic anodic reaction

In a proton exchange membrane fuel cell (PEMFC), hydrogen is used as a fuel and hydrogen oxidation reaction (HOR) occurs at the anode. Hydrogen adsorbs on the surface of catalytic Pt where hydrogen – hydrogen bond breaks giving adsorbed atomic hydrogen.[1]

$$\frac{1}{2} H_2 \rightarrow 2\, H^*$$
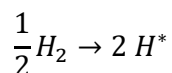
Each of these adsorbed atomic hydrogens undergoes subsequent electron loss to form proton which leaves the anode surface and passes through the membrane to the cathodic chamber.

$$H^* \rightarrow H^+ + e^-$$
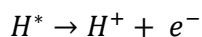
Net anodic reaction:

$$\frac{1}{2} H_2 \rightarrow 2\, H^+ + 2e^-$$
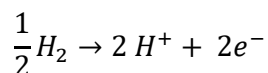
The rate of HOR in presence of platinum catalyst is relatively faster than the oxygen reduction occurring in the cathode. Moreover, the anode overpotential remained less than 3 mV for a loading of 0.05 mg/cm^2 of platinum catalyst when pure H$_2$ was used in PEMFC. Due to the minimum voltage loss and small loading of Pt catalyst for HOR in PEMFC, development of a suitable catalyst for ORR received more attention in the current research field.

1.2.2 Catalytic cathodic reaction

The complex proton coupled multi electron transfer ORR occurs at the cathode of fuel cells which can proceed either in a direct four electron reduction or two steps two electron reduction. Moreover, the difficulties in adsorption of O_2 molecule on the cathode surface, the activation or cleavage of O–O bond and the removal of oxides cause the sluggish kinetics of ORR.[2] This complicated reaction mechanism and slow kinetics of ORR poses serious challenges for PEMFCs.[3, 4] In order to overcome these challenges the catalyst must meet few requirements. It should be able to withstand the corrosive environment of PEMFCs while performing the activation of O_2 molecule. It should also allow prompt release of product typically water from the catalyst surface thereby exposing the active sites of catalyst for further ORR.[5] In general Pt catalyst meets all these requirements and is most commonly used ORR catalyst. However, the loading of Pt at cathode is much more in comparison to that at anode.[6] The cathodic ORR accounts for more than half of the voltage loss in a PEMFCs and thus it is essential to develop a low cost suitable ORR catalyst.[7]

1.3 Ideal characteristics of ORR catalyst

In order to be an effective ORR catalyst, it must excel in all four different categories mentioned below.[8]

  i.   **Activity:** The ability to adhere the reactant molecules i.e. O_2 on the active site of catalyst surface in order to facilitate the ORR reaction. However, the adhesion should not be too strong otherwise the active sites will be blocked by the reactant and product molecules.

  ii. **Selectivity:** The ability to choose the direct four electron ORR instead of two steps two electron ORR. This selectivity will allow an effective ORR catalysis with minimum production of undesirable intermediates and side products.

iii. **Stability:** The catalyst must be stable in the corrosive environment of fuel cells which include strong oxidants, reactive radicals, an acidic environment and high and rapidly fluctuating temperatures in presence of an applied potential.

iv. **Poison tolerance:** The catalyst must not be reactive towards the impurities probably present in the fuel cell itself and also in the feed gases.

1.4 Evaluations of Pt as electrocatalyst in the four categories

1.4.1 Activity

The heterogenous catalyst on a metal surface must have moderate binding energy to adsorb the reactant molecules on the active sites and also allow the facile release of product once the reaction is completed. If the binding energy is too strong, the active sites will be quickly occupied by the reactant molecules and also the reaction intermediates or product molecules will remain adhered to the active sites preventing further catalysis. On contrary, if the binding energy of the catalyst is too weak it will fail to bind the substrate molecules to the active sites and consequently there will either no reaction at all or the reaction will be too slow. According to Sabatier principle, there must be an optimum binding energy between substrate and the active site of the catalyst. Balandin's volcano diagram can visually demonstrates the Sabatier's principle. It includes plot of the binding energy of the reactant molecules versus the catalytic activity. When the binding energy of active site and substrate is either too strong or too weak, it corresponds to lower catalytic activity. Therefore, the activity peak in the volcano diagram reflects the ideal binding energy for effective catalysis of a reaction.

The rate of HOR in PEMFCs is much faster than ORR and also requires much less Pt loading. Since the kinetics of ORR is slow, it gained more focus in research field and extensive efforts are directed towards development of ORR catalysts. The Balandin volcano plot shown

in Figure 1.2 is a plot of ORR activity versus the binding energy of single oxygen atom with different metals.[9] From the plot, it can be clearly depicted that the activity peak is achieved by pure Pt metal with optimum binding interaction to single oxygen atom which is neither too strong nor too weak.
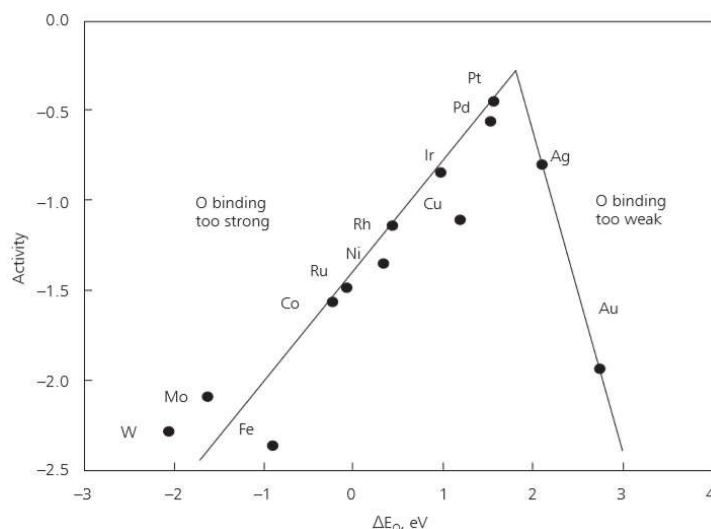
Figure 1.2: Trends in oxygen reduction activity plotted as a function of the oxygen binding energy. [9] (Copyright 2004 American Chemical Society)

However, the oxygen binding interaction with the active site of catalyst is not the sole parameter for ORR catalysis. The dissociative ORR mechanism involves two-step process in which initially the single oxygen atom binds to the active site of Pt catalyst and then reaction intermediates i.e. hydroxyl group. So, the binding interaction of OH group with active site is equally important. The surface bound hydroxyl group is reduced and protonated to form the product i.e. water which then leaves the metal surface In Figure 1.3, it is observed that the binding energy of both single oxygen and hydroxyl are somewhat linearly correlated. Pt also shows highest activity with optimum binding interaction with both oxygen atom and hydroxyl

group. When the single oxygen atom binding energy of metal is too strong, the catalytic activity of ORR is hampered due to the surface bound oxygen atom which prevents further catalysis. On the other hand, when the single oxygen atom binding energy is too weak, it is difficult to activate the dissociation of oxygen molecule since single O atom can only bind to the sites very weakly.[10] But there are many possibilities where these binding energies can be tuned and the binding energy of O and OH will not follow the same correlation and could lead to the development of completely new ORR catalysts.[9]
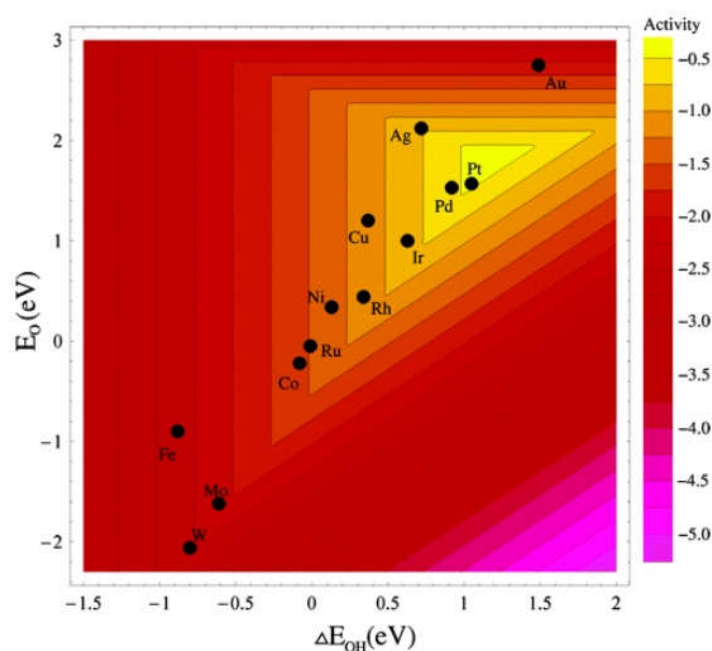
Figure 1.3: Trends in oxygen reduction activity plotted as a function of both the oxygen and the hydroxyl group binding energy. [9] (Copyright 2004 American Chemical Society)

1.4.2 Selectivity

Selectivity is another important parameter for catalysis. A catalyst must have the ability to prefer a reaction pathway with desired product and avoid formation of undesirable intermediates and side products. The ORR can proceed either in direct four electron reduction

pathway making water as the product or it can proceed via a two-step two electron reduction process which requires more energy and generates corrosive hydrogen peroxide.

The selectivity of the catalyst determines the pathway of the ORR which can follow either associative or dissociative mechanism. The activity of the catalyst was explained above on the basis of dissociative four electron ORR mechanism which produces the desired product i.e. water. But ORR can also occur in alternative two electron reaction associative mechanism which results in the formation of hydrogen peroxide. The presence of free H_2O_2 is considered as extremely detrimental in the fuel cell environment as it can lead to corrosion of electrocatalyst and also the chemical degradation of the separatory membrane in PEMFCs.[10] The associative ORR mechanism begins with the adsorption of oxygen molecule on the metal surface without the breaking of the double bond between them. The dissociative mechanism usually occurs when Pt is used as the catalyst. This happens due to the fact that the O=O bond is quickly broken down when it adheres on the Pt metal surface.

Scanning electrochemical microscopy was used by Sanchez group to quantify the amount of H_2O_2 produced when different metal electrocatalysts were used for ORR in 0.5 M H_2SO_4 electrolyte. The amount of H_2O_2 production was related to the number of electrons (n) involved in ORR. When the value of n equals 4, it signifies the four electron ORR and when n equals 2, it means two electron ORR leading to H_2O_2 formation. This study revealed that Pt and $Pd_{80}Co_{20}$ follow the desired dissociative ORR mechanism with the n value reaching almost 4 and on contrary, mercury (Hg) displayed associative ORR mechanism with the n value close to 2.[11] Therefore, Pt is considered as the most suitable ORR catalyst as it has the high selectivity towards energy efficient dissociative ORR mechanism over a wide range of applied potential.
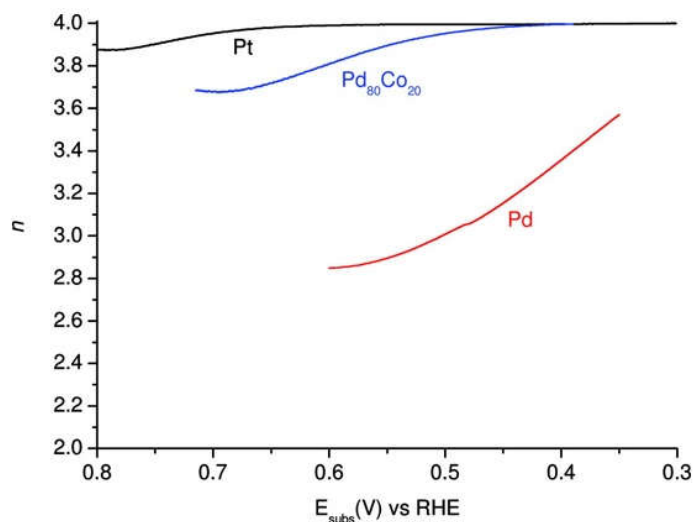
Figure 1.4: Number of electrons transferred (*n*) during ORR at Pt (black line), Pd (red line) and $Pd_{80}Co_{20}$ (blue line) as a function of applied potential in an oxygen saturated 0.5 M H_2SO_4 solution.[11] (Copyright @ 2009 American Chemical Society)

1.4.3 Stability

The fuel cell environment is considered quite harsh owing to the presence of strong oxidants, reactive reaction intermediates in highly acidic conditions. Moreover, fuel cells are usually operated at elevated temperatures with rapid fluctuations in the applied potential. So, the metal must have the ability to withstand the corrosive environment of fuel cells over a long period of time in order to qualify as a suitable ORR catalyst. Most metals are susceptible to dissolution at low pH conditions when subjected to either fluctuating or constant high potentials. Some metals can display long term stability by forming an oxide film which will inhibit metal dissolution, however the activity of catalyst will remarkably decrease.[10]

Pt metal with high ORR activity and four electron selectivity also cannot meet the long -term durability requirement of the electrocatalyst. When potential cycling occurs either in the form of varying loads on fuel cell stack or constant high potential during fuel cell stack idling

condition, Pt dissolution occurs.[12] Pt dissolved as particles in corrosive environment of fuel cells, these particles can form larger particles by depositing on existing Pt particles or diffuse into the electrochemically inaccessible portions of the membrane electrode assembly.[13, 14] As a result, there is a loss of electrochemically active surface area of cathode catalyst which is held responsible for the loss of ORR activity over a longer period of time.

1.4.4 Poison Tolerance

The catalytic activity of a material can be greatly affected by the presence of small amounts of poisons. Typically, in a fuel cell, catalyst poisoning can occur due to impurities present in the fuel cells or in the feed gases. Pt catalyst is susceptible to various poisons such as sulfur species, carbon monoxide or methanol. When fuel crossover occurs, which is the leaking of the fuel from the anodic to cathodic chamber of fuel cell, the catalytic activity is greatly hampered. When the fuel is methanol, it readily adsorbs on the active sites of Pt and results in methanol oxidation reaction (MOR). Since both ORR and MOR occur simultaneously at the cathode, there will be a reduction in cathode potential followed by additional water generation and increase in the required stoichiometric ratio of oxygen.[15-17] In addition, methanol oxidation reaction proceeds via carbon monoxide intermediates which can also poison the Pt surfaces. It can adsorb on the Pt surfaces thus inhibiting ORR and reducing the efficiency of fuel cells.[18] There are two potential solutions to overcome this poisoning issue in fuel cell applications: one is to develop a catalyst with better poison tolerance and higher electrocatalytic activity for ORR and the other method of protection is to keep poisons out of the system. Several research including alloying of the Pt with other metals has been done to improve the methanol tolerance of Pt without affecting its high ORR activity. Many binary, ternary and quaternary Pt alloys, Pt-based composites and organic metal complexes have been developed thereafter.[19-22]

1.4.5 Drawbacks of using Pt and Pt based alloys electrocatalyst

Even though Pt catalyst suffers from long term durability issue and poison intolerance, yet it is the most common electrocatalyst to overcome the sluggish kinetics of ORR. This is because of the fact that it has high ORR activity and four electron ORR mechanism selectivity. During the 1960s, the first practical application of alkaline fuel cells with platinum as an ORR electrocatalyst was in the Apollo lunar mission. However, the much-awaited rapid progress in large-scale practical application of fuel cells has not been achieved so far due to the high cost of the Pt catalysts, together with the limited reserves of Pt in nature. Toyota has recently started commercialization of fuel cell vehicles (FCVs), in 2014 they have introduced the '*Toyota Mirai*' in Japan and now these FCVs are available in America at a price of around 58500 US dollars. The high Pt loading in the fuel cell stacks is considered as one of the main reasons for the high sale price of the *Toyota Mirai*.[23] As can be seen in figure 1.5, the annual production of Pt is too low and it is quite expensive. Therefore, it would be beneficial if the Pt loading can be either reduced or completely replaced with an abundant and cheap metal.
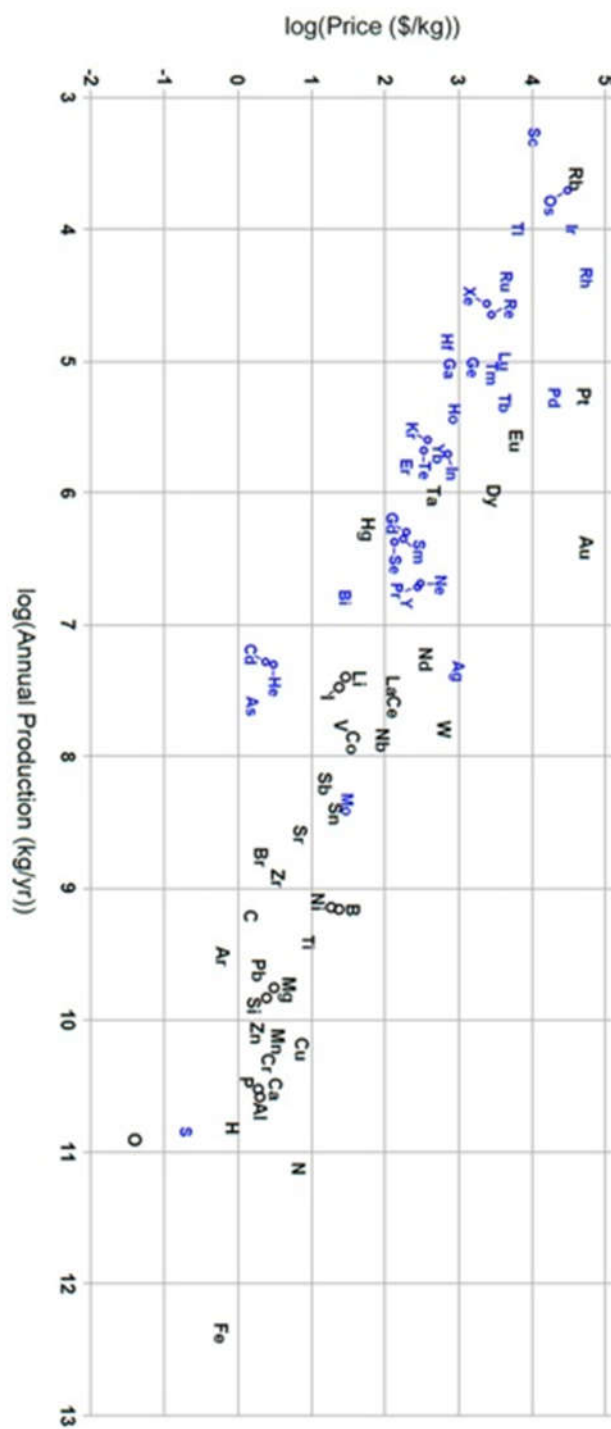
Figure 1.5: Price of the elements (in $/kg) versus their annual production (in kg/yr). [24] (Copyright @ 2012 Royal Society of Chemistry)

1.5   Platinum free ORR catalyst

1.5.1   Carbon based non–noble metal ORR catalyst from macrocycles

Among different non-precious metal ORR catalysts, transition metal–nitrogen–carbon (M–N–C) complexes or composites are considered as the most promising candidates due to their inexpensive price, high ORR activity, long term durability and good resistance to the methanol cross-over effect.[25, 26] Among the different transition metal, geologically abundant transition metals such as iron and cobalt are mostly used to develop M–N–C ORR catalyst. The annual production and the price of these metals are much less in comparison to Pt as observed in Figure 1.5. Research into carbon based non-noble metal ORR catalyst initiated in 1964 when Jasinski discovered that cobalt phthalocyanine showed higher ORR activity.[27, 28] Initially he employed the metal–N_4–macrocycles as ORR catalyst but later noticed a small increase in cell voltage when the cobalt phthalocyanine was polarized to H_2 evolution potentials. In 1981, Vanveen *et al.* reported that these phthalocyanine complexes were not very stable. Their catalytic activity decreases rapidly which might be due to the hydrolysis of the metal chelate.[29] However, it was established afterwards that the stability of these complexes increased remarkably when these complexes were subjected to heat-treatment (pyrolysis) in an inert atmosphere.[30] The pyrolyzed compound were much more stable in acidic electrolyte, but in the long term working conditions their ORR activity reduced. The reason behind this decomposition of the metal chelate could be initiated by the corrosive reaction intermediates such as hydrogen peroxide.[29]

Different researchers have suggested different theories behind the enhancement in activity and stability of these macrocycles after pyrolysis. Some researchers claimed that heat treatment of the complexes created an active carbon-nitrogen surface, which, along with the metal atom are held responsible for the enhanced catalytic ORR activity.[31, 32] While other

researchers claimed that after pyrolysis, M-N$_4$ moiety is retained in the structure which served as the catalytic ORR active site. [33, 34] Wiesener *et al.* also gave another theory suggesting that the transition metal probably assist the formation of the active catalyst.[30, 35]

1.5.2 Nitrogen rich polymer for carbon based non−noble metal ORR catalyst

In 1989, Gupta *et al.* reported the first M–N–C composites for ORR generated by the heat treatment of polyacrylonitrile (PAN) mixed with transition metal salts and high surface area carbon at various temperatures in an inert atmosphere (argon).[36] After that, Wu *et al.* also reported another polymer to develop M–N–C ORR catalyst. He suggested that polyaniline (PANI) has the favorable combination of aromatic rings connected via nitrogen-containing groups and can serve as a promising template compound for nitrogen and carbon. Both the PANI and graphite have similar structures, and upon heat treatment, the structure could facilitate the nitrogen-containing active sites to incorporate into the partially graphitized carbon matrix. Moreover, such nitrogen rich polymer could ensure uniform distribution of nitrogen sites on the surface and an increase in the active-site density and thereby higher ORR activity.[6]

Chan *et al.* reported synthesis of M–N–C catalyst derived from the polymerization of meta-phenylenediamine. The reason behind choosing poly-m-phenylenediamine (PmPDA) was that it has higher percentage of nitrogen (26 vs 15 wt %) and has better thermostability than PANI. [37] The higher thermostability will reduce the loss of nitrogen during the high temperature heat treatment. This group also investigated the effects of a series of inorganic molecules (e.g., CO and NO$_x$) and ions (e.g., Cl$^-$, F$^-$, Br$^-$, SCN$^-$, S^{2-}, and SO$_3^{2-}$ on the catalytic ORR activity and reported that the active site of the PmPDA-FeNx/C catalyst was the Fe element, and the valence state of Fe might be mainly Fe^{III}. [38] Later, Zhu *et al.* also used different ortho, meta and para phenylenediamine monomers as shown in Figure 1.6 to polymerize with

different iron precursors and evaluated the ORR catalytic performance of the pyrolyzed polymer. They established that polymerization of *p*-phenylenediamine and simultaneous heat treatment with ferric chloride yielded better dispersion and higher pyridinic N content which led to the formation of more FeN_x sites and higher ORR activity.[39]
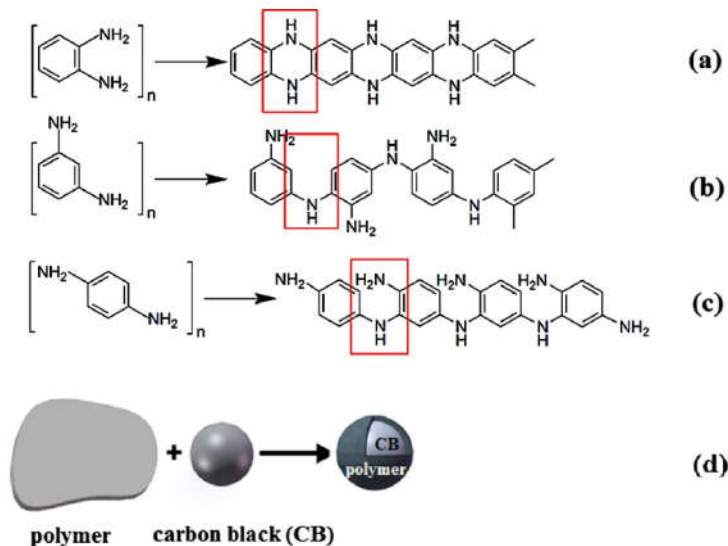
Figure 1.6: (a−c) Polymerization schemes for different phenylenediamine monomers leading to different N coordination in the polymer. (d) Schematic of polymer deposition as a thick coat around carbon black.[39] (Copyright@ 2016 Elsevier)

Osmieri *et al.* revealed that the total N and Fe content were not the limiting factors for ORR activity but rather the specific presence of pyridinic and pyrrolic N species, along with Fe exposed by an increase in micro porosity from a second heat treatment were correlated to the better catalytic performance. They have used poly(vinylpyrrolidone) (PVP) along with mesoporous carbon and iron acetate to develop Fe–N–C non-noble metal electrocatalyst.[40] Another group followed simple pyrolysis–leaching–stabilization (PLS) sequence for poly-pyrrole (PPy) and ferric chloride to develop Fe/N–C electrocatalyst. They reported that the higher ORR

activity could be due to several factors such as amount of graphic carbon, conductivity, and surface area. In their work, the graphitic and pyridinic N incorporated by the metal precursor resulted in the highest ORR activity.[41] After that, several works are still going on to develop better ORR catalyst from pyrolyzed polymers.

1.5.3 Metal organic frameworks derived ORR catalyst

Metal−organic frameworks (MOFs) and other similar frameworks as sources of metal, nitrogen and carbon were also used to develop nonprecious metal ORR catalyst. Pyrolysis of MOFs provided more dispersed metal sites within the porous catalysts. In 2011, Proietti *et al.* synthesized Fe-based catalysts by ball milling a mixture of a ZIF-8 (a commercial Zn II zeolitic imidazolate framework of formula $ZnN_4 C_8 H_{12}$), 1,10-phenanthroline and ferrous acetate and followed by two heat treatments, firstly in argon flow at 1050°C, then in ammonia at 950°C. The ZIF-8 served as a microporous host for phenanthroline and ferrous acetate to form a catalyst precursor which was subsequently heat treated. This particular MOF was chosen for its high nitrogen content and its high microporous surface area, two critical factors for the high ORR activity of Fe/N/C-catalysts. This catalyst displayed a power density of 0.75 Wcm^{-2} at 0.6V, a meaningful voltage for polymer electrolyte-membrane fuel cells operation and quite comparable to that obtained using a commercial Pt catalyst tested under similar conditions.[42]

Zhao *et al.* demonstrated facile one-pot synthetic process of preparing ZIF based non-precious metal ORR electrocatalyst. The group prepared in situ solid state Zn-based ZIFs from different ligands such as 2-methylimidazole (HmIm), 2-ethylimidazole (HeIm), imidazole (HIm) and ligand 4-azabenzimidazole (H4ablm) with tris-1,10-phenanthroline iron (II) perchlorate, which was added as precursor for transition metal, as shown in Figure 1.7. The resulting material was heat treated at 1050 °C in argon. Then it was acid leached prior

secondary heat treatment at 950°C in ammonia. The Zn(eIm)$_2$TPIP achieved the highest

volumetric current density of 88.1 A cm^{-3} at 0.8 V in a polymer electrolyte fuel cell test.[43]
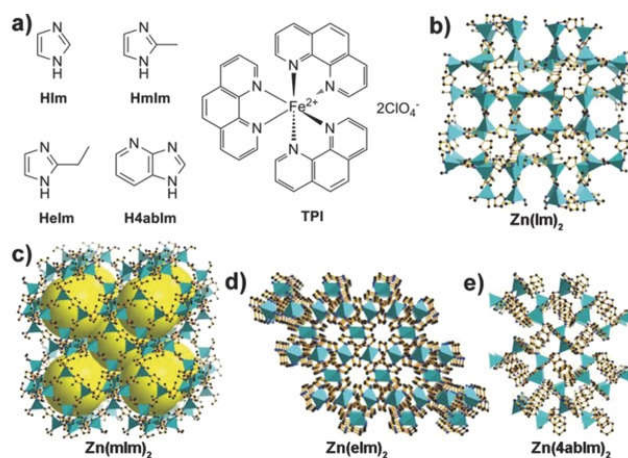
Figure 1.7: a) Chemical structures of ligands and iron additive. b) Crystal structure of Zn(Im)$_2$.

c) Crystal structure of Zn(mIm)$_2$ (aka ZIF-8, yellow balls represent void). d) Crystal structure

of Zn(eIm)$_2$. e) Crystal structure of Zn(4abIm)$_2$.[43] (Copyright@ 2013 Wiley Online Library)

Another group reported a method of preparing highly efficient, nanofibrous non-

precious metal catalyst by electrospinning solution dimethylformamide (DMF) of PAN, poly

methyl methacrylate, Tris-1,10-phenanthroline iron (II) perchlorate (TPI) and ZIF-8. Then it

followed some post treatments illustrated in Figure 1.8. Since it retained its network structure

even after pyrolysis and acid wash, this network structure facilitated the mass transfer of

oxygen molecule via its macro porous voids between the interconnected nanofibers. In

addition, each nanofiber was predominantly microporous which allowed uniform and dense

dispersion of catalytic sites throughout the fiber. This catalyst exhibited an initial peak power

of 0.90 W cm^{-2} in a single cell test with reasonable durability in the acidic working

environments.[44] The three MOF based catalyst discussed above displayed as the best performing MOF based M–N–C. However, many different approaches have been done recently to generate MOFs based catalysts with high ORR activity.
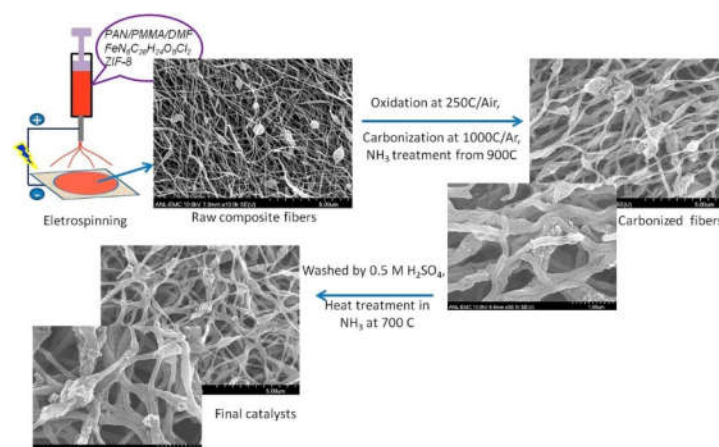
Figure 1.8: The schematic diagram for synthesis of Fe based ORR catalyst by electrospinning. The fibrous structure remained intact after pyrolysis and acid wash as shown in SEM images. (Copyright@ 2015 Proceedings of the National Academy of Sciences of the United States of America)

1.5.4 Templated synthesis of carbon based non−noble metal ORR catalyst

The use of hard templates along with other precursors is another procedure to prepare non-noble metal ORR catalysts. Hard templates such as silica colloid (12 nm SiO_2 nanomaterials dispersed in water), ordered mesoporous silica SBA-15, montmorillonite (MMT, a layered clay with a 2D open channel) were generally used to promote the formation of desired pore structures and to increase the surface area of the catalyst. The most common hard template is silica which can be removed by washing with either KOH or HF. Liang *et al.* reported cobalt−nitrogen-doped carbon (C−N−Co) and iron−nitrogen-doped carbon (C−N−

Fe) catalysts for ORR in acidic media. They used vitamin B12 (VB12) and the polyaniline-Fe (PANI-Fe) complex as the respective precursors for the two different catalysts as shown in Figure 1.9. The most active mesoporous catalyst was obtained from VB12 and silica nanoparticles template which was later removed by HF etching. The resulting C−N−Co catalyst exhibited a remarkable ORR activity in acidic medium. Its well-defined porous structures with a narrow mesopore size distribution, high Brunauer−Emmett−Teller surface area, and homogeneous distribution of abundant metal−N_x active sites were held responsible for its high ORR activity.[45]
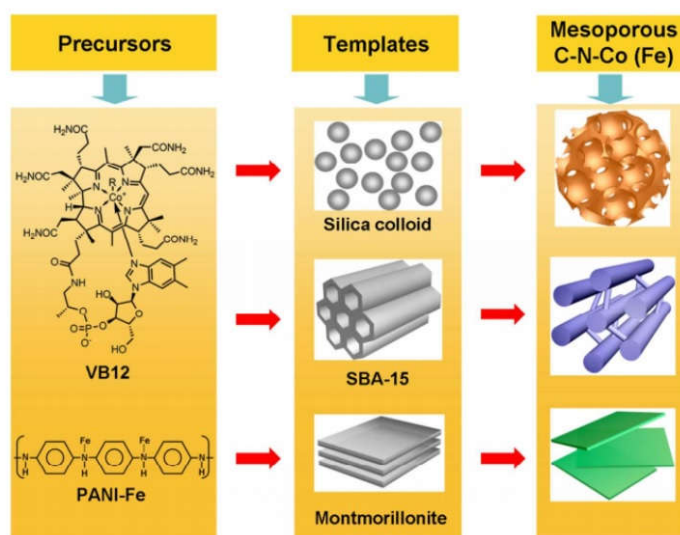
Figure 1.9: The schematic diagram for synthesis of Fe or Co based ORR catalyst by using different hard templates.[45] (Copyright@ 2013 American Chemical Society)

Liu et al. developed a series of Fe–N_x doped mesoporous carbons from pyrolysis of nitrogen containing ionic liquids and iron precursors in mesoporous silicas (i.e. SBA-15). This group established that the high ORR activity and excellent methanol tolerance of the catalyst

were due to its high specific surface area with uniformly distributed square pyramidal structure of Fe–N$_x$ species. The ORR active pyridinic-N and pyridinic-N–Fe were also present in abundance in the Fe–N$_x$ doped mesoporous carbon catalyst. [46] Other researchers suggested that not only surface area and pore size can affect ORR activity, but, pore shapes are equally important in templated catalyst synthesis. Ink bottle shaped pores (smaller at neck) in the catalyst showed lower ORR performance because of the inhibited accessibility of O$_2$.[47]

Another researcher used micrometer-scale sodium chloride (NaCl) crystal as a template which adsorbed the precursors on its surfaces. This template allowed the formation of micrometer sized graphitic carbon nanosheets during the pyrolysis and also distributed the iron precursor uniformly preventing the aggregation. The resulting catalyst with well-dispersed FeN$_x$ species and encased Fe/Fe$_3$C nanoparticles showed enhanced ORR activity.[48] In the same year, Niu *et al.* also used NaCl as a template to polymerize pyrrole in presence of polyvinyl pyrrolidone and iron (III) chloride. Before pyrolyzing the polymer sheets, the NaCl template was washed with water. The porous carbon sheets contained N and/or Fe−N sites which performed as good ORR catalyst in an alkaline medium.[49]

1.5.5 Heteroatom doped carbon based non−noble metal ORR catalyst

Another procedure to prepare non-noble metal ORR catalysts is heteroatom doping. Many researchers have attempted to incorporate dopants such as sulfur and phosphorus into the catalyst surface in addition to the metal and nitrogen. Men *et al.* reported that Fe and S decorated N-doped graphene/carbon nanosheets exhibited superior performance toward ORR which was better than commercial Pt/C in alkaline media due to existence of multiple effective intrinsic active sites. He suggested that sulfur in −C−S− and conjugated −C=S− bonds along with the pyridinic N and graphitic N, and the Fe-N$_x$ moiety effectively facilitated ORR in

alkaline solution.[50] Zhang *et al.* also performed dual doping by calcining Co^{2+} based ZIF-67 loaded with different sulfur containing molecules such as thiourea, NH_4SCN, sublimed sulfur, thiophene. This group found that incorporation of sulfur into the structure led to higher N content and a greater percentage of pyridinic N formation. As a result, the ORR overpotential was lowered and enhanced ORR activity was observed.[51]

Yang *et al.* have suggested that the major factor for infusing efficient ORR activity in the doped carbon is breaking the electroneutrality of carbon matrix.[52] So, electropositive dopants such as phosphorus or boron (P or B) with less electronegativity than carbon can also influence the ORR activity of the electrocatalyst in alkaline medium.[52-54] Besides N and S doping, P-doping was also investigated by some researchers. Singh *et al.* and Razmjooei *et al.* also investigated a new class of non−noble metal heteroatom bonded carbon (Fe−P) ORR catalyst. They polymerized phytic acid with iron (III) chloride to obtain a ferric phytate complex as shown in Figure 1.10 and then carbonized at high temperature to obtain the catalyst. However, it was noticed that the ORR activity of the prepared Fe−P-900 sample improved significantly in both acidic and alkaline media compared to nonactivity of iron free phytic acid carbonized catalyst in acidic medium. [55, 56] Research on heteroatom doping is still going on to develop effective ORR catalyst.
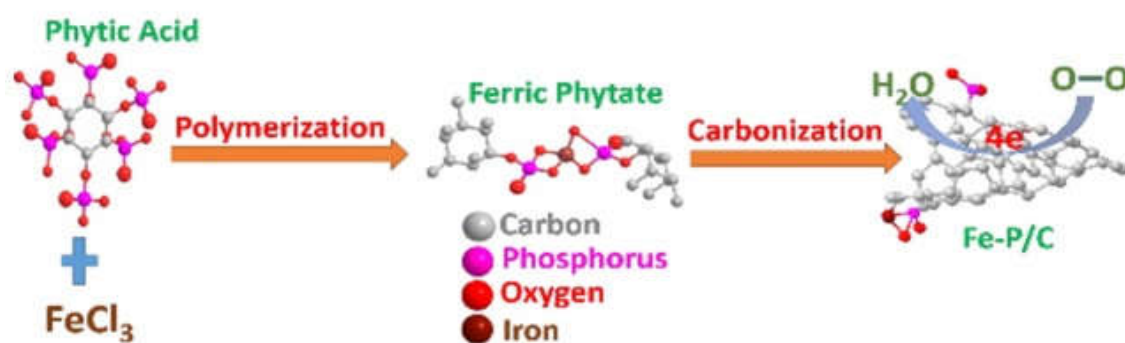
Figure 1.10: The reaction scheme diagram for synthesis of Fe-P based carbon catalyst by carbonization of ferric phytate.[55] (Copyright@ 2015 American Chemical Society)

1.6 Prospect of metal-based heteroatom doped porous carbon as ORR catalyst

Different heteroatoms (e.g., nitrogen, boron, phosphorus) can be introduced into carbon nanomaterials in order to tune their optoelectronic properties and/or chemical activities through electron modulation. This would increase the practical applicability of such materials.[57-59] Two different approaches could be done to obtain heteroatom doped carbon nanomaterials; either by in-situ doping while synthesizing the carbon nanomaterials or through post-treatment of preformed carbon nanomaterials with heteroatom containing precursors. The first approach can incorporate heteroatoms uniformly throughout the entire structure. On the other hand, the second approach can only functionalize the surface of the carbon while retaining their bulk properties.[60, 61]

Basically, heteroatom doping involves the replacement of some carbon atoms in the graphitic structure with other non-metal elements such as B, N, P, S, and/or F. Due to the difference in the size and electronegativity of the heteroatoms from those of carbon atom, the heteroatoms can change the charge distribution and the electronic properties and thus, cause electron modulation in carbon nanomaterials.[62] In addition, this heteroatom doping would induce defects causing further change in the chemical activity of carbon nanomaterials. As a result, these heteroatom doped carbon materials could be used in numerous practical applications even as ORR electrocatalyst in fuel cells.[57]

Among the different heteroatoms, nitrogen has received immense attention and is still the most common dopant in carbon materials. In the periodic table, nitrogen is next to carbon with similar atomic size as carbon but their electron configuration is different. Due to the difference in electronegativity between carbon and nitrogen, N doping in carbon could change their electronic structures and minimize the lattice mismatch and thus increase their applications in electrochemical energy conversion and storage systems.[63]

The band gap between the highest-occupied molecular orbital (HOMO) and the lowest-unoccupied molecular orbital (LUMO) can be reduced by nitrogen doping. Due to nitrogen doping, there will be corresponding lift in the HOMO as depicted in Figure 1.11 (a) and this would allow smooth transfer of the electron from the nitrogen doped carbon nanotube (NCNT) to the adsorbed oxygen.[64, 65] A doping-induced charge redistribution was observed due to the as significant charge difference between the nitrogen atom and the carbon atoms adjacent the nitrogen dopant as shown in Figure 1.11 (b). The enhanced electrocatalytic ORR activity in NCNT was due to this N doping-induced electron-deficient carbon atoms which enhanced the chemisorption of O_2.
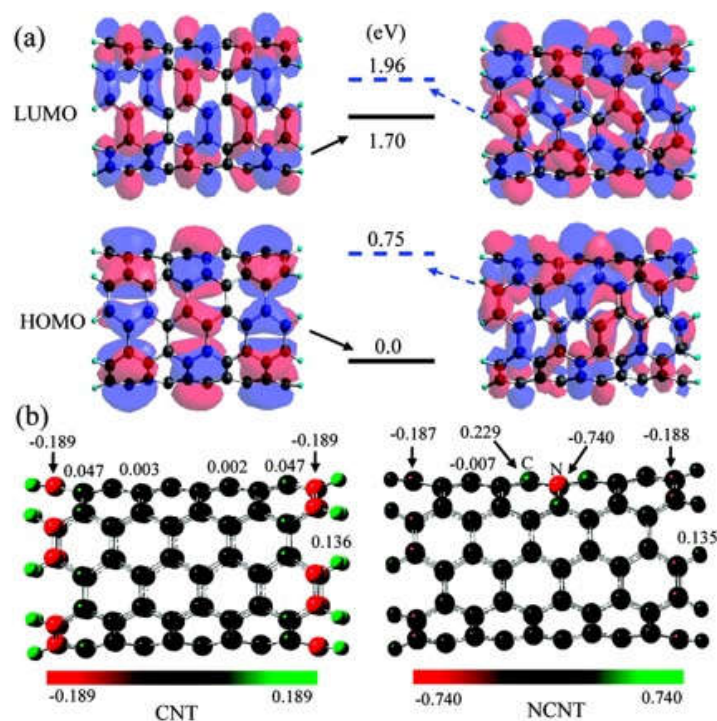
Figure 1.11: (a) LUMO/HOMO and **(b)** the charge distribution of normal carbon nanotube (CNT) and nitrogen doped carbon nanotube (NCNT).[65] (Copyright@ 2010 American Chemical Society)

According to bonding configuration, nitrogen can exist as pyridinic, pyrollic or graphitic N in nitrogen doped carbon. As shown in Figure 1.12, the pyridinic N bonds to two C atoms with one p-elctron localized in the π conjugated system while pyrrolic N have two p-electrons. Graphitic N substitutes a C atom in the hexagonal ring. Among these bonding configurations of N, the graphitic and the pyridinic N are considered as ORR active. In general, the graphitic N content affects the limiting current density, whereas the pyridinic N content improves the onset potential for ORR.[66]
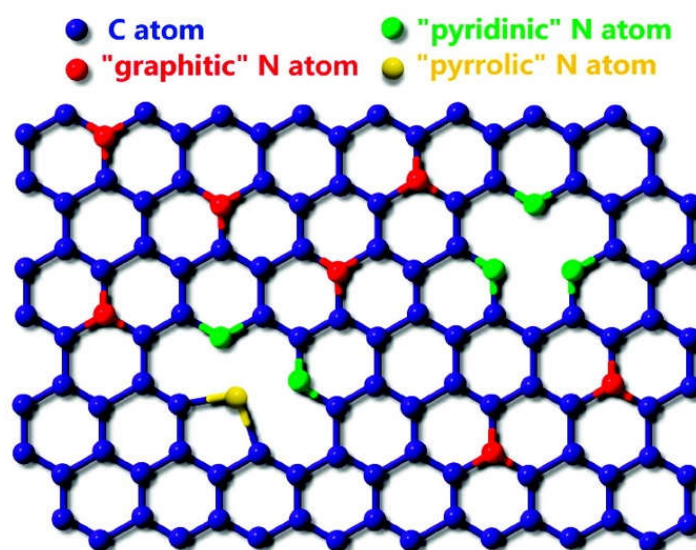
Figure 1.12: Schematic representation of the nitrogen doped graphene. The blue, red, green, and yellow spheres represent the carbon, "graphitic" nitrogen, "pyridinic" nitrogen, and "pyrrolic" nitrogen atoms respectively.[67] (Copyright@ 2009 American Chemical Society)

In case of graphitic N, nitrogen being more electronegative than C, it allows transfer of electrons from the adjacent C to N atom and N then returns the electrons to adjacent C. This overall donation and backdonation process aids the dissociation of oxygen molecule on adjacent C atom and also allows a strong chemical bond to form between O and C.[68] For pyridinic N, the oxygen molecules are adsorbed on carbon atoms next to pyridinic N with Lewis basicity.[69, 70] Pyridinic-N donates one p-electron to the aromatic π system and its lone electron pair in the plane of carbon matrix increases the electron-donating property of the catalyst. So, the oxygen bonds with nitrogen and/or the adjacent carbon atoms which weakens the O−O bond and thereby, facilitates the reduction of O_2.[71]

In case of sulfur dopant, the difference in electronegativity between carbon and sulfur ($\chi = 2.58$) is very small in comparison to that between carbon and nitrogen ($\chi = 3.04$) and so the effect of the charge polarization is almost negligible. Jeon *et al.* suggested a different mechanism for the enhanced ORR activity of edge sulfurized graphene nano platelets (SGnP). This group performed theoretical calculations to investigate the origin of high ORR activity of SGnP. Their calculation suggested that the electronic spin density along with charge density can affect the ORR activity of SGnP. The doped S atoms located at the edges of the graphene nanoplatelets can strongly promote the ORR activity. Both the charge and spin density can be induced on the graphene through covalently bonded sulfur or sulfur oxide at the zigzag and armchair edges (Figure 1.13). According to their theoretical prediction and experimental result, it has been reported that carbon atoms with either high spin densities and/ or positive charge could serve as the active sites and enhance the activity of electrocatalytic ORR.[72]
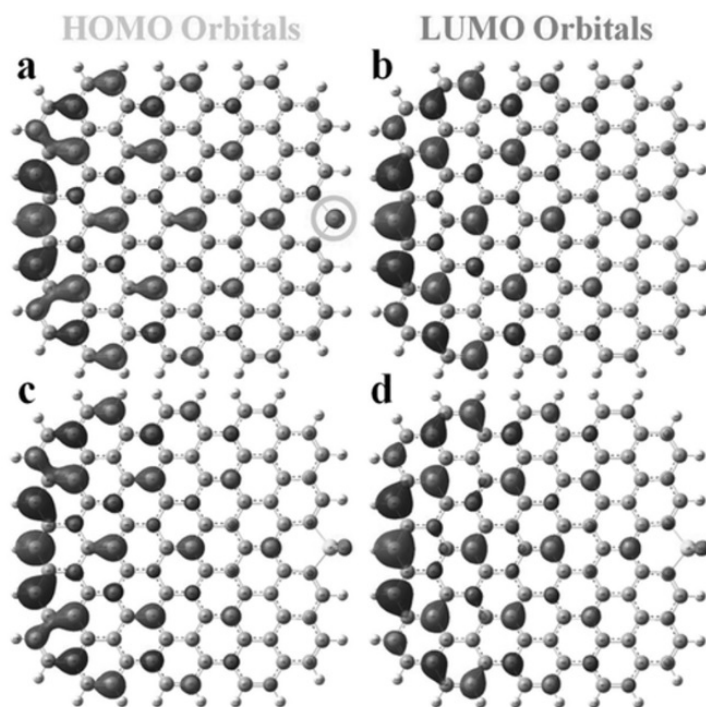
Figure 1.13: HOMO and LUMO distributions: a) HOMO of SGnP; b) LUMO of SGnP; c) HOMO of SOGnP; and, d) LUMO of SOGnP.[72] (Copyright@ 2009 American Chemical Society)

It has been observed in the literature, that the electrocatalytic ORR activity of metal free either pure carbon or nitrogen-doped carbon materials in acidic and alkaline conditions are quite different. They exhibited much higher ORR onset potentials in base than in acid. However, when non-precious metal such as iron, cobalt, etc. were introduced into heteroatom doped carbon structures, the differences in activity between acid and base became less significant. Chung *et al.* suggested that metal-free sites involving C or N atoms might serve as ORR active sites in base, but, to obtain higher ORR onset potentials in acid conditions, non-precious metal should be incorporated into the carbon structure. Li *et al.* also reported that in the absence of Fe, the electrocatalyst showed quite low activity in acidic medium.[73] On the basis of molecular orbital theory, it has been assumed that Fe atom in Fe−N/C aided in developing strong back bonding with the adsorbed O_2 which increased the O−O bond distance

facilitating ORR.[74] Some researchers have proposed that the in plane $Fe-N_4/Fe-N_2$ center bound to the carbon support is responsible for the higher kinetic current density and better ORR performance.[75, 76] On the other hand, some researchers have suggested that the transition metal actually helps in the formation of active sites but itself is not the active site. [32, 77-79] Nallathambi *et al.* reported that transition metals such as Fe or Co facilitated the incorporation of pyridinic-N and quaternary-N into the carbon matrix, which increased electron-donor property of the N-doped carbon. Due to the bonding between oxygen and nitrogen and/or the adjacent carbon atom, the O–O bond weakened and enhanced electrocatalytic ORR activity was observed.[78] Even though there is a debate regarding the active sites for ORR, however, the importance of heteroatom doped carbon-based non-precious metal catalysts for ORR is beyond doubt. Therefore, development of cost effective and highly efficient heteroatom doped carbon-based non-precious metal catalysts is imperative.

1.7   Thesis statement

This thesis represents a comprehensive study focused on the development of cost effective and highly efficient heteroatom doped carbon-based non-precious metal catalysts for ORR. Two different synthetic approaches were done to synthesize Fe based S and N dual doped porous carbon and Co_3O_4 deposited on benzimidazole derived porous carbon. A set of experimental techniques such as Brunauer−Emmett−Teller (BET) surface area measurement, scanning electron microscopy (SEM), energy-dispersive X-ray spectroscopy (EDX), thermogravimetric analysis (TGA), X-ray photoelectron spectroscopy (XPS), Powder X-ray diffraction (P-XRD), Raman spectrometry, inductively coupled plasma optical emission spectrometry (ICP-OES) etc. were used to evaluate the physical characteristics of the synthesized materials. To explore the electrocatalytic performance of the synthesized catalyst, different techniques such as cyclic voltammetry, linear sweep voltammetry, amperometric i-t

curve were obtained. The results obtained was also compared to the commercially available catalyst, 20 wt% Pt/C.

Chapter 2 reports on the reaction mechanism and kinetics of ORR and also different measurement techniques to study ORR. This chapter starts with a discussion of ORR mechanism and kinetics using different catalysts including Pt, N doped carbon and transition-metal based heteroatom doped carbon. Next, different measurement techniques such as cyclic voltammetry to observe ORR in either oxygen or nitrogen saturated electrolyte, linear sweep voltammetry to study the number of electrons involved in ORR will be discussed. The stability and poison tolerance evaluation using amperometric i-t curve will be discussed as well.

In Chapter 3, the synthesis of Fe based S and N doped porous carbon will be discussed. An easy synthetic route will be proposed which involves pyrolysis of benzimidazole monomer with iron thiocyanate. Next the physical properties will be explained to illustrate the significance of porosity, different bonding configurations of heteroatoms in the structure. Finally, the electrocatalytic performance of the catalyst will be analyzed with respect to different parameters in terms of the structure of the catalyst and also its performance will be compared to that of the 20 wt% Pt/C.

Chapter 4 will discuss the prospect of another synthetic method which involves the hydrothermal growth of Co_3O_4 on a template of benzimidazole derived porous carbon. The amount of Co_3O_4 will be varied and the electrocatalytic ORR performance of the N doped porous carbon with Co_3O_4 and without Co_3O_4 will be discussed.

All the results are summarized and overall conclusions and outlook are provided in Chapter 5.

1.8 References

1.   Zhang, J., *PEM fuel cell electrocatalysts and catalyst layers : fundamentals and applications*. Springer: London, 2008; p xxi, 1137 p.

2.   Nie, Y.; Li, L.; Wei, Z. D., Recent advancements in Pt and Pt-free catalysts for oxygen reduction reaction. *Chemical Society Reviews* **2015,** *44* (8), 2168-2201.

3.   Gasteiger, H. A.; Markovic, N. M., Just a Dream-or Future Reality? *Science* **2009,** *324* (5923), 48-49.

4.   Wagner, F. T.; Lakshmanan, B.; Mathias, M. F., Electrochemistry and the Future of the Automobile. *Journal of Physical Chemistry Letters* **2010,** *1* (14), 2204-2219.

5.   Yu, K.; Groom, D.; Wang, X.; Yang, Z.; Gummalla, M.; Ball, S.; Myers, D.; Ferreira, P., Degradation Mechanisms of Platinum Nanoparticle Catalysts in Proton Exchange Membrane Fuel Cells: The Role of Particle Size. *Chemistry of Materials* **2014,** *26* (19), 5540-5548.

6.   Wu, G.; More, K. L.; Johnston, C. M.; Zelenay, P., High-Performance Electrocatalysts for Oxygen Reduction Derived from Polyaniline, Iron, and Cobalt. *Science* **2011,** *332* (6028), 443-447.

7.   Sheng, W. C.; Gasteiger, H. A.; Shao-Horn, Y., Hydrogen Oxidation and Evolution Reaction Kinetics on Platinum: Acid vs Alkaline Electrolytes. *Journal of the Electrochemical Society* **2010,** *157* (11), B1529-B1536.

8.   Holton, O.; Stevenson, J., The Role of Platinum in Proton Exchange Membrane Fuel Cells Evaluation of platinum's unique properties for use in both the anode and cathode of a proton exchange membrane fuel cell. *Platinum Metals Review* **2013,** *57* (4), 259-271.

9. Norskov, J. K.; Rossmeisl, J.; Logadottir, A.; Lindqvist, L.; Kitchin, J. R.; Bligaard, T.; Jonsson, H., Origin of the overpotential for oxygen reduction at a fuel-cell cathode. *Journal of Physical Chemistry B* **2004,** *108* (46), 17886-17892.

10. Borup, R.; Meyers, J.; Pivovar, B.; Kim, Y. S.; Mukundan, R.; Garland, N.; Myers, D.; Wilson, M.; Garzon, F.; Wood, D.; Zelenay, P.; More, K.; Stroh, K.; Zawodzinski, T.; Boncella, J.; McGrath, J. E.; Inaba, M.; Miyatake, K.; Hori, M.; Ota, K.; Ogumi, Z.; Miyata, S.; Nishikata, A.; Siroma, Z.; Uchimoto, Y.; Yasuda, K.; Kimijima, K. I.; Iwashita, N., Scientific aspects of polymer electrolyte fuel cell durability and degradation. *Chemical Reviews* **2007,** *107* (10), 3904-3951.

11. Sanchez-Sanchez, C. M.; Bard, A. J., Hydrogen Peroxide Production in the Oxygen Reduction Reaction at Different Electrocatalysts as Quantified by Scanning Electrochemical Microscopy. *Analytical Chemistry* **2009,** *81* (19), 8094-8100.

12. Mathias, M.; Gasteiger, H.; Makharia, R.; Kocha, S.; Fuller, T.; Pisco, J., Can available membranes and catalysts meet automotive PEFC requirements? *Abstracts of Papers of the American Chemical Society* **2004,** *228*, U653-U653.

13. Xie, J.; Wood, D. L.; More, K. L.; Atanassov, P.; Borup, R. L., Microstructural changes of membrane electrode assemblies during PEFC durability testing at high humidity conditions. *Journal of the Electrochemical Society* **2005,** *152* (5), A1011-A1020.

14. Ferreira, P. J.; la O, G. J.; Shao-Horn, Y.; Morgan, D.; Makharia, R.; Kocha, S.; Gasteiger, H. A., Instability of Pt/C electrocatalysts in proton exchange membrane fuel cells - A mechanistic investigation. *Journal of the Electrochemical Society* **2005,** *152* (11), A2256-A2271.

15. Urban, P. M.; Funke, A.; Muller, J. T.; Himmen, M.; Docter, A., Catalytic processes in solid polymer electrolyte fuel cell systems. *Applied Catalysis a-General* **2001,** *221* (1-2), 459-470.

16.   Gurau, B.; Smotkin, E. S., Methanol crossover in direct methanol fuel cells: a link between power and energy density. *Journal of Power Sources* **2002,** *112* (2), 339-352.

17.   Cruickshank, J.; Scott, K., The degree and effect of methanol crossover in the direct methanol fuel cell. *Journal of Power Sources* **1998,** *70* (1), 40-47.

18.   Antolini, E.; Lopes, T.; Gonzalez, E. R., An overview of platinum-based catalysts as methanol-resistant oxygen reduction materials for direct methanol fuel cells. *Journal of Alloys and Compounds* **2008,** *461* (1-2), 253-262.

19.   Shukla, A. K.; Raman, R. K.; Choudhury, N. A.; Priolkar, K. R.; Sarode, P. R.; Emura, S.; Kumashiro, R., Carbon-supported Pt-Fe alloy as a methanol-resistant oxygen-reduction catalyst for direct methanol fuel cells. *Journal of Electroanalytical Chemistry* **2004,** *563* (2), 181-190.

20.   Shukla, A. K.; Neergat, M.; Bera, P.; Jayaram, V.; Hegde, M. S., An XPS study on binary and ternary alloys of transition metals with platinized carbon and its bearing upon oxygen electroreduction in direct methanol fuel cells. *Journal of Electroanalytical Chemistry* **2001,** *504* (1), 111-119.

21.   Neergat, M.; Shukla, A. K.; Gandhi, K. S., Platinum-based alloys as oxygen-reduction catalysts for solid-polymer-electrolyte direct methanol fuel cells. *Journal of Applied Electrochemistry* **2001,** *31* (4), 373-378.

22.   Yano, H.; Ono, C.; Shiroishi, H.; Okada, T., New CO tolerant electro-catalysts exceeding Pt-Ru for the anode of fuel cells. *Chemical Communications* **2005,** (9), 1212-1214.

23.   Shao, M. H.; Chang, Q. W.; Dodelet, J. P.; Chenitz, R., Recent Advances in Electrocatalysts for Oxygen Reduction Reaction. *Chemical Reviews* **2016,** *116* (6), 3594-3657.

24.   Vesborg, P. C. K.; Jaramillo, T. F., Addressing the terawatt challenge: scalability in the supply of chemical elements for renewable energy. *Rsc Advances* **2012,** *2* (21), 7933-7947.

25.   Bezerra, C. W. B.; Zhang, L.; Lee, K. C.; Liu, H. S.; Marques, A. L. B.; Marques, E. P.; Wang, H. J.; Zhang, J. J., A review of Fe-N/C and Co-N/C catalysts for the oxygen reduction reaction. *Electrochimica Acta* **2008,** *53* (15), 4937-4951.

26.   Hu, Y.; Jensen, J. O.; Zhang, W.; Cleemann, L. N.; Xing, W.; Bjerrum, N. J.; Li, Q. F., Hollow Spheres of Iron Carbide Nanoparticles Encased in Graphitic Layers as Oxygen Reduction Catalysts. *Angewandte Chemie-International Edition* **2014,** *53* (14), 3675-3679.

27.   Jasinski, R., NEW FUEL CELL CATHODE CATALYST. *Nature* **1964,** *201* (492), 1212-&.

28.   Jasinski, R., COBALT PHTHALOCYANINE AS A FUEL CELL CATHODE. *Journal of the Electrochemical Society* **1965,** *112* (5), 526-&.

29.   Vanveen, J. A. R.; Vanbaar, J. F.; Kroese, C. J.; Coolegem, J. G. F.; Dewit, N.; Colijn, H. A., OXYGEN REDUCTION ON TRANSITION-METAL PORPHYRINS IN ACID ELECTROLYTE .1. ACTIVITY. *Berichte Der Bunsen-Gesellschaft-Physical Chemistry Chemical Physics* **1981,** *85* (8), 693-700.

30.   Wiesener, K., N-4-CHELATES AS ELECTROCATALYST FOR CATHODIC OXYGEN REDUCTION. *Electrochimica Acta* **1986,** *31* (8), 1073-1078.

31.   Scherson, D. A.; Gupta, S. L.; Fierro, C.; Yeager, E. B.; Kordesch, M. E.; Eldridge, J.; Hoffman, R. W.; Blue, J., COBALT TETRAMETHOXYPHENYL PORPHYRIN - EMISSION MOSSBAUER-SPECTROSCOPY AND O-2 REDUCTION ELECTROCHEMICAL STUDIES. *Electrochimica Acta* **1983,** *28* (9), 1205-1209.

32.   Yeager, E., ELECTROCATALYSTS FOR O-2 REDUCTION. *Electrochimica Acta* **1984,** *29* (11), 1527-1537.

33.   Vanwingerden, B.; Vanveen, J. A. R.; Mensch, C. T. J., AN EXTENDED X-RAY ABSORPTION FINE-STRUCTURE STUDY OF HEAT-TREATED COBALT

PORPHYRIN CATALYSTS SUPPORTED ON ACTIVE-CARBON. *Journal of the Chemical Society-Faraday Transactions I* **1988,** *84*, 65-74.

34.   Vanveen, J. A. R.; Colijn, H. A.; Vanbaar, J. F., ON THE EFFECT OF A HEAT-TREATMENT ON THE STRUCTURE OF CARBON-SUPPORTED METALLOPORPHYRINS AND PHTHALOCYANINES. *Electrochimica Acta* **1988,** *33* (6), 801-804.

35.   Wiesener, K.; Ohms, D.; Neumann, V.; Franke, R., N-4 MACROCYCLES AS ELECTROCATALYSTS FOR THE CATHODIC REDUCTION OF OXYGEN. *Materials Chemistry and Physics* **1989,** *22* (3-4), 457-475.

36.   Gupta, S.; Tryk, D.; Bae, I.; Aldred, W.; Yeager, E., HEAT-TREATED POLYACRYLONITRILE-BASED CATALYSTS FOR OXYGEN ELECTROREDUCTION. *Journal of Applied Electrochemistry* **1989,** *19* (1), 19-27.

37.   Chan, H. S. O.; Ng, S. C.; Hor, T. S. A.; Sun, J.; Tan, K. L.; Tan, B. T. G., POLY(META-PHENYLENEDIAMINE) - SYNTHESIS AND CHARACTERIZATION BY X-RAY PHOTOELECTRON-SPECTROSCOPY. *European Polymer Journal* **1991,** *27* (11), 1303-1308.

38.   Wang, Q.; Zhou, Z. Y.; Lai, Y. J.; You, Y.; Liu, J. G.; Wu, X. L.; Terefe, E.; Chen, C.; Song, L.; Rauf, M.; Tian, N.; Sun, S. G., Phenylenediamine-Based FeNx/C Catalyst with High Activity for Oxygen Reduction in Acid Medium and Its Active-Site Probing. *Journal of the American Chemical Society* **2014,** *136* (31), 10882-10885.

39.   Zhu, Y. S.; Zhang, B. S.; Feng, Z. B.; Su, D. S., Synthesis-structure-performance correlation for poly(phenylenediamine)s/iron/carbon non-precious metal catalysts for oxygen reduction reaction. *Catalysis Today* **2016,** *260*, 112-118.

40.   Osmieri, L.; Videla, A.; Specchia, S., Optimization of a Fe-N-C electrocatalyst supported on mesoporous carbon functionalized with polypyrrole for oxygen reduction

reaction under both alkaline and acidic conditions. *International Journal of Hydrogen Energy* **2016,** *41* (43), 19610-19628.

41.   Tran, T. N.; Song, M. Y.; Singh, K. P.; Yang, D. S.; Yu, J. S., Iron-polypyrrole electrocatalyst with remarkable activity and stability for ORR in both alkaline and acidic conditions: a comprehensive assessment of catalyst preparation sequence. *Journal of Materials Chemistry A* **2016,** *4* (22), 8645-8657.

42.   Proietti, E.; Jaouen, F.; Lefevre, M.; Larouche, N.; Tian, J.; Herranz, J.; Dodelet, J. P., Iron-based cathode catalyst with enhanced power density in polymer electrolyte membrane fuel cells. *Nature Communications* **2011,** *2*.

43.   Zhao, D.; Shui, J. L.; Grabstanowicz, L. R.; Chen, C.; Commet, S. M.; Xu, T.; Lu, J.; Liu, D. J., Highly Efficient Non-Precious Metal Electrocatalysts Prepared from One-Pot Synthesized Zeolitic Imidazolate Frameworks. *Advanced Materials* **2014,** *26* (7), 1093-1097.

44.   Shui, J. L.; Chen, C.; Grabstanowicz, L.; Zhao, D.; Liu, D. J., Highly efficient nonprecious metal catalyst prepared with metal-organic framework in a continuous carbon nanofibrous network. *Proceedings of the National Academy of Sciences of the United States of America* **2015,** *112* (34), 10629-10634.

45.   Liang, H. W.; Wei, W.; Wu, Z. S.; Feng, X. L.; Mullen, K., Mesoporous Metal-Nitrogen-Doped Carbon Electrocatalysts for Highly Efficient Oxygen Reduction Reaction. *Journal of the American Chemical Society* **2013,** *135* (43), 16002-16005.

46.   Liu, S. H.; Yang, S. W.; Chen, S. C., Iron nanoparticles with a square pyramidal structure in mesoporous carbons as an effective catalyst toward oxygen reduction. *Rsc Advances* **2016,** *6* (112), 111366-111373.

47.   Marzorati, S.; Longhi, M., Templating induced behavior of platinum-free carbons for oxygen reduction reaction. *Journal of Electroanalytical Chemistry* **2016,** *775*, 350-355.

48.   Zhang, Y.; Huang, L. B.; Jiang, W. J.; Zhang, X.; Chen, Y. Y.; Wei, Z. D.; Wan, L. J.; Hu, J. S., Sodium chloride-assisted green synthesis of a 3D Fe-N-C hybrid as a highly active electrocatalyst for the oxygen reduction reaction. *Journal of Materials Chemistry A* **2016,** *4* (20), 7781-7787.

49.   Niu, W. H.; Li, L. G.; Wang, N.; Zeng, S. B.; Liu, J.; Zhao, D. K.; Chen, S. W., Volatilizable template-assisted scalable preparation of honeycomb-like porous carbons for efficient oxygen electroreduction. *Journal of Materials Chemistry A* **2016,** *4* (28), 10820-10827.

50.   Men, B.; Sun, Y. Z.; Liu, J.; Tang, Y.; Chen, Y. M.; Wan, P. Y.; Pan, J. Q., Synergistically Enhanced Electrocatalytic Activity of Sandwich-like N-Doped Graphene/Carbon Nanosheets Decorated by Fe and S for Oxygen Reduction Reaction. *Acs Applied Materials & Interfaces* **2016,** *8* (30), 19533-19541.

51.   Zhang, C.; An, B.; Yang, L.; Wu, B. B.; Shi, W.; Wang, Y. C.; Long, L. S.; Wang, C.; Lin, W. B., Sulfur-doping achieves efficient oxygen reduction in pyrolyzed zeolitic imidazolate frameworks. *Journal of Materials Chemistry A* **2016,** *4* (12), 4457-4463.

52.   Yang, L. J.; Jiang, S. J.; Zhao, Y.; Zhu, L.; Chen, S.; Wang, X. Z.; Wu, Q.; Ma, J.; Ma, Y. W.; Hu, Z., Boron-Doped Carbon Nanotubes as Metal-Free Electrocatalysts for the Oxygen Reduction Reaction. *Angewandte Chemie-International Edition* **2011,** *50* (31), 7132-7135.

53.   Liu, Z. W.; Peng, F.; Wang, H. J.; Yu, H.; Zheng, W. X.; Yang, J. A., Phosphorus-Doped Graphite Layers with High Electrocatalytic Activity for the O-2 Reduction in an Alkaline Medium. *Angewandte Chemie-International Edition* **2011,** *50* (14), 3257-3261.

54.   Yang, D. S.; Bhattacharjya, D.; Inamdar, S.; Park, J.; Yu, J. S., Phosphorus-Doped Ordered Mesoporous Carbons with Different Lengths as Efficient Metal-Free Electrocatalysts

for Oxygen Reduction Reaction in Alkaline Media. *Journal of the American Chemical Society* **2012,** *134* (39), 16127-16130.

55.   Singh, K. P.; Bae, E. J.; Yu, J. S., Fe-P: A New Class of Electroactive Catalyst for Oxygen Reduction Reaction. *Journal of the American Chemical Society* **2015,** *137* (9), 3165-3168.

56.   Razmjooei, F.; Singh, K. P.; Bae, E. J.; Yu, J. S., A new class of electroactive Fe- and P-functionalized graphene for oxygen reduction. *Journal of Materials Chemistry A* **2015,** *3* (20), 11031-11039.

57.   Yu, D. S.; Nagelli, E.; Du, F.; Dai, L. M., Metal-Free Carbon Nanomaterials Become More Active than Metal Catalysts and Last Longer. *Journal of Physical Chemistry Letters* **2010,** *1* (14), 2165-2173.

58.   Dai, L. M., Functionalization of Graphene for Efficient Energy Conversion and Storage. *Accounts of Chemical Research* **2013,** *46* (1), 31-42.

59.   Nistor, R. A.; Newns, D. M.; Martyna, G. J., The Role of Chemistry in Graphene Doping for Carbon-Based Electronics. *Acs Nano* **2011,** *5* (4), 3096-3103.

60.   Titirici, M. M.; Thomas, A.; Antonietti, M., Aminated hydrophilic ordered mesoporous carbons. *Journal of Materials Chemistry* **2007,** *17* (32), 3412-3418.

61.   Sidik, R. A.; Anderson, A. B.; Subramanian, N. P.; Kumaraguru, S. P.; Popov, B. N., O-2 reduction on graphite and nitrogen-doped graphite: Experiment and theory. *Journal of Physical Chemistry B* **2006,** *110* (4), 1787-1793.

62.   Rinzler, A. G.; Liu, J.; Dai, H.; Nikolaev, P.; Huffman, C. B.; Rodriguez-Macias, F. J.; Boul, P. J.; Lu, A. H.; Heymann, D.; Colbert, D. T.; Lee, R. S.; Fischer, J. E.; Rao, A. M.; Eklund, P. C.; Smalley, R. E., Large-scale purification of single-wall carbon nanotubes: process, product, and characterization. *Applied Physics a-Materials Science & Processing* **1998,** *67* (1), 29-37.

63.   Wood, K. N.; O'Hayre, R.; Pylypenko, S., Recent progress on nitrogen/carbon structures designed for use in energy and sustainability applications. *Energy & Environmental Science* **2014,** *7* (4), 1212-1249.

64.   Ikeda, T.; Boero, M.; Huang, S. F.; Terakura, K.; Oshima, M.; Ozaki, J., Carbon alloy catalysts: Active sites for oxygen reduction reaction. *Journal of Physical Chemistry C* **2008,** *112* (38), 14706-14709.

65.   Hu, X. B.; Wu, Y. T.; Li, H. R.; Zhang, Z. B., Adsorption and Activation of O-2 on Nitrogen-Doped Carbon Nanotubes. *Journal of Physical Chemistry C* **2010,** *114* (21), 9603-9607.

66.   Lai, L. F.; Potts, J. R.; Zhan, D.; Wang, L.; Poh, C. K.; Tang, C. H.; Gong, H.; Shen, Z. X.; Jianyi, L. Y.; Ruoff, R. S., Exploration of the active center structure of nitrogen-doped graphene-based catalysts for oxygen reduction reaction. *Energy & Environmental Science* **2012,** *5* (7), 7936-7942.

67.   Wei, D. C.; Liu, Y. Q.; Wang, Y.; Zhang, H. L.; Huang, L. P.; Yu, G., Synthesis of N-Doped Graphene by Chemical Vapor Deposition and Its Electrical Properties. *Nano Letters* **2009,** *9* (5), 1752-1758.

68.   Deng, D. H.; Pan, X. L.; Yu, L. A.; Cui, Y.; Jiang, Y. P.; Qi, J.; Li, W. X.; Fu, Q. A.; Ma, X. C.; Xue, Q. K.; Sun, G. Q.; Bao, X. H., Toward N-Doped Graphene via Solvothermal Synthesis. *Chem Mater* **2011,** *23* (5), 1188-1193.

69.   Guo, D. H.; Shibuya, R.; Akiba, C.; Saji, S.; Kondo, T.; Nakamura, J., Active sites of nitrogen-doped carbon materials for oxygen reduction reaction clarified using model catalysts. *Science* **2016,** *351* (6271), 361-365.

70.   Daems, N.; Sheng, X.; Vankelecom, I. F. J.; Pescarmona, P. P., Metal-free doped carbon materials as electrocatalysts for the oxygen reduction reaction. *J Mater Chem A* **2014,** *2* (12), 4085-4110.

71.   Zhang, J. T.; Dai, L. M., Heteroatom-Doped Graphitic Carbon Catalysts for Efficient Electrocatalysis of Oxygen Reduction Reaction. *Acs Catalysis* **2015,** *5* (12), 7244-7253.

72.   Jeon, I. Y.; Zhang, S.; Zhang, L. P.; Choi, H. J.; Seo, J. M.; Xia, Z. H.; Dai, L. M.; Baek, J. B., Edge-Selectively Sulfurized Graphene Nanoplatelets as Efficient Metal-Free Electrocatalysts for Oxygen Reduction Reaction: The Electron Spin Effect. *Advanced Materials* **2013,** *25* (42), 6138-6145.

73.   Li, Y. G.; Zhou, W.; Wang, H. L.; Xie, L. M.; Liang, Y. Y.; Wei, F.; Idrobo, J. C.; Pennycook, S. J.; Dai, H. J., An oxygen reduction electrocatalyst based on carbon nanotube-graphene complexes. *Nature Nanotechnology* **2012,** *7* (6), 394-400.

74.   Behret, H.; Binder, H.; Sandstede, G.; Scherer, G. G., ON THE MECHANISM OF ELECTROCATALYTIC OXYGEN REDUCTION AT METAL-CHELATES .3. METAL PHTHALOCYANINES. *Journal of Electroanalytical Chemistry* **1981,** *117* (1), 29-42.

75.   Lefevre, M.; Dodelet, J. P.; Bertrand, P., Molecular oxygen reduction in PEM fuel cells: Evidence for the simultaneous presence of two active sites in Fe-based catalysts. *Journal of Physical Chemistry B* **2002,** *106* (34), 8705-8713.

76.   Koslowski, U. I.; Abs-Wurmbach, I.; Fiechter, S.; Bogdanoff, P., Nature of the catalytic centers of porphyrin-based electrocatalysts for the ORR: A correlation of kinetic current density with the site density of Fe-N-4 Centers. *Journal of Physical Chemistry C* **2008,** *112* (39), 15356-15366.

77.   Gouerec, P.; Savy, M.; Riga, J., Oxygen reduction in acidic media catalyzed by pyrolyzed cobalt macrocycles dispersed on an active carbon: The importance of the content of oxygen surface groups on the evolution of the chelate structure during the heat treatment. *Electrochimica Acta* **1998,** *43* (7), 743-753.

78.   Nallathambi, V.; Lee, J. W.; Kumaraguru, S. P.; Wu, G.; Popov, B. N., Development of high performance carbon composite catalyst for oxygen reduction reaction in PEM Proton Exchange Membrane fuel cells. *Journal of Power Sources* **2008,** *183* (1), 34-42.

79.   Maldonado, S.; Stevenson, K. J., Direct preparation of carbon nanofiber electrodes via pyrolysis of iron(II) phthalocyanine: Electrocatalytic aspects for oxygen reduction. *Journal of Physical Chemistry B* **2004,** *108* (31), 11375-11383.

Chapter 2

Study of oxygen reduction reaction

2.1 Reaction mechanism of ORR

It is well known that ORR is one of the crucial reactions affecting the performance of fuel cell. This reaction can proceed either through a two-step $2e^-$ pathway leading to the formation of H_2O_2 (in acidic medium) or HO_2^- in alkaline medium) as the intermediate species, or by a more efficient, direct $4e^-$ reduction producing H_2O (in acidic medium) or OH^- (in alkaline medium).[1] Several DFT studies suggested that the adsorption energetics of the reaction intermediates and the reaction barriers on the catalyst surface could determine the selectivity of ORR, whether it should follow two electrons or four electrons pathway.[2, 3] For ORR, the most desired reduction pathway is the 4e$^-$ reduction pathway since it is energy efficient and produces water as the product in acidic electrolyte.

In case of two-electron ORR, partial reduction of oxygen occurs resulting in the formation of H_2O_2 as the product and only the reaction intermediate OOH* is involved. The reactions involved in associative two electron reduction pathway:

$$O_2 + {}^* \rightarrow O_2^*$$

$$O_2^* + H_2O + e^- \rightarrow OOH^* + OH^-$$

$$OOH^* + H^+ + e^- \rightarrow H_2O_2 + {}^*$$
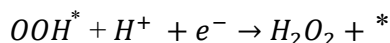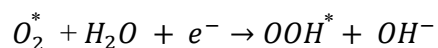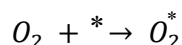
Here, "*" denotes a site on the catalyst surface. So, O_2 molecule is adsorbed on the catalyst surface and gains two electrons forming H_2O_2.

On contrary, when the full reduction of oxygen to water i.e. four electron ORR occur, it can proceed by either associative or dissociative mechanisms, depending on whether the

oxygen molecule dissociates before reduction. The primary difference between associative and dissociative mechanism is the intermediates involved. In associative mechanism, three different intermediates, (*OOH, *O, and *OH) are involved, however, the dissociative pathway involves only *O and *OH intermediates which alters the construction of the free energy pathway.[4] The dissociative four electron ORR mechanism involves the following reactions:

$$O_2 + 2^* \rightarrow 2O^*$$

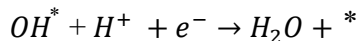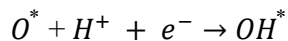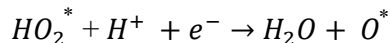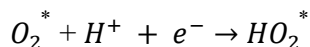$$2O^* + 2H^+ + 2e^- \rightarrow 2OH^*$$

$$2OH^* + 2H^+ + 2e^- \rightarrow 2H_2O + 2^*$$
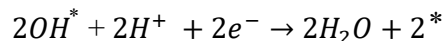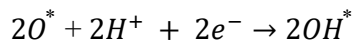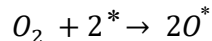
Here, "*" denotes a site on the catalyst surface. In this dissociative four electron mechanism, no H_2O_2 is produced. O_2 molecule is adsorbed on the surface of the catalyst where the O-O bond is broken and two adsorbed atomic oxygen are formed. These adsorbed oxygen atoms gain two electrons in the two consecutive steps and form water.

The associative four electron ORR mechanism involves the following reactions:

$$O_2 + ^* \rightarrow O_2^*$$

$$O_2^* + H^+ + e^- \rightarrow HO_2^*$$

$$HO_2^* + H^+ + e^- \rightarrow H_2O + O^*$$

$$O^* + H^+ + e^- \rightarrow OH^*$$

$$OH^* + H^+ + e^- \rightarrow H_2O + ^*$$
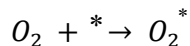
Here, "*" denotes a site on the catalyst surface. In this associative four electron mechanism, no H_2O_2 is produced. O_2 molecule is adsorbed on the surface of the catalyst but the O-O bond is not broken unlike dissociative mechanism. The last two steps in associative

mechanisms are similar to the dissociative mechanism above. However, the first three new steps involving adsorption of molecular oxygen and direct proton/electron transfer to it and to OOH are quite different since O-O bond remains intact. Instead of forming water, the adsorbed OOH intermediates can alternately form hydrogen peroxide. So, the associative mechanism is also termed as peroxo mechanism.[5]

2.2 ORR mechanism on Pt

Pt (111) surface is considered as an ideal benchmark for comparisons to theoretical work due to its large electrochemical volume, sensitive and single-crystal structure. Nørskov *et al.* proposed the free energy diagram at three different electrode potentials for ORR mechanism.[5] For small oxygen coverage, the electrode potential measured relative to the standard hydrogen potential is equal to the potential of the fuel cell with the assumptions that the anodic reaction is in equilibrium and ohmic losses are negligible. The relationship $U = 0$ V corresponds to the reaction conducted by short circuiting the cell where all the elementary steps are strongly exothermic implying a facile reaction. At the maximum potential allowed by thermodynamics in fuel cells, $U_0 = 1.23$ eV, both electron/proton-transfer steps become uphill and the energy barriers for the two steps are literally the same. Either of these electron/proton transfer step could be the rate limiting step. For this process, there will be an activation free energy equal to the larger of the reaction free energies where the overpotential, $\eta = U_0 - U$. The adsorbed oxygen and hydroxide on the Pt (111) surface act as thermodynamic sinks for the oxygen reduction process and the activation energy for the total process or the overpotential at the maximum cell voltage $U_0 = 1.23$ eV is 0.5 eV as shown in Figure 2.1. When the oxygen coverage shifted to high i.e. 0.5 mono layer at the equilibrium cell potential, the energies are

shifted up. This suggested that the first electron and proton transfer have the higher energy

barrier, however, the value of the energy barrier is independent of the coverage.
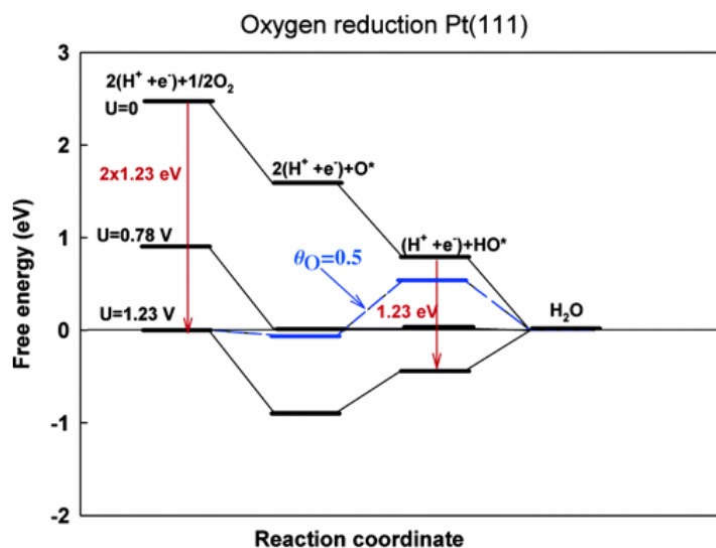
Figure 2.1: Free-energy diagram for oxygen reduction over Pt (111). Results for low oxygen

coverage are shown at zero cell potential (U = 0), at the equilibrium potential (U = 1.23 V),

and at the highest potential (U = 0.78 V) where all reaction steps are exothermic. For U = 1.23

V, the free-energy diagram for the case of an oxygen coverage of 1 /2 monolayer is included.[5]

(Copyright 2004 American Chemical Society)

According to the theory of Nørskov *et al.*, the dissociative ORR mechanism for Pt (111) is dependent on the coverage of oxygen. At high oxygen coverage, Pt (111) has lower free-energy barriers in the associative mechanism than in the dissociative mechanism. On the other hand, when the oxygen coverage is low, the dissociative mechanism has the lowest energy barriers and dominates over associative mechanism as illustrated in Figure 2.2 and 2.3. Some researchers suggested that the ORR on Pt surfaces normally follows a dissociative mechanism due to the strong initial adsorption of oxygen molecule and quick dissociation to atomic oxygen.[6]
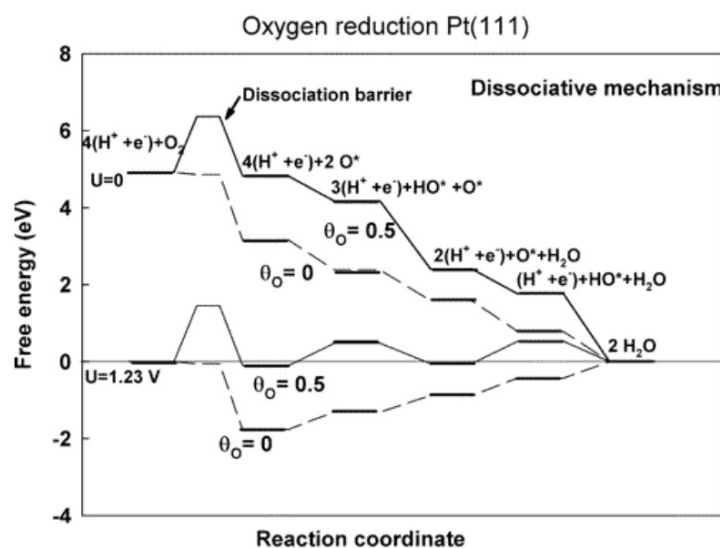
Figure 2.2: Free-energy diagram for oxygen reduction over Pt (111) at two different potentials and at two different oxygen coverages, including the barrier for O2 dissociation.[5] (Copyright 2004 American Chemical Society)
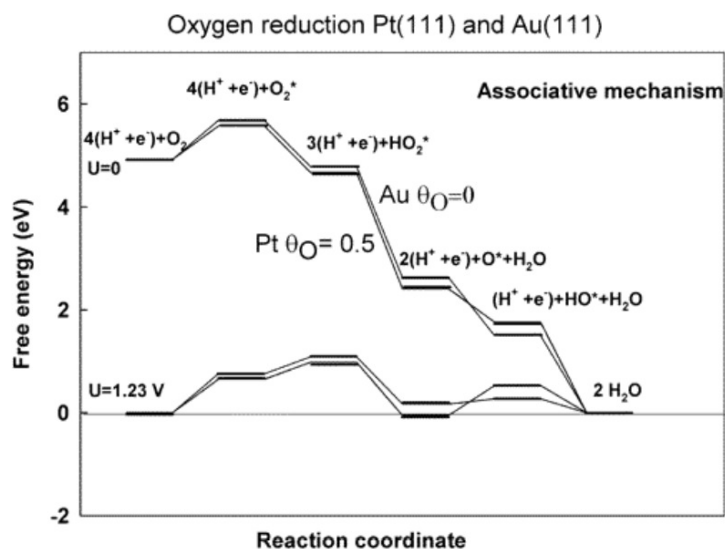
Figure 2.3: Free-energy diagram for oxygen reduction via the associative mechanism at two different potentials over Au (111) at a low oxygen coverage and over Pt (111) at an oxygen coverage of 1 /2 monolayer.[5] (Copyright 2004 American Chemical Society)

2.3 ORR mechanism on heteroatom doped carbon

The ORR mechanism on heteroatom doped carbon is preferably associative mechanism since the dissociation barrier is very high on carbon surfaces. From the density functional theory calculations, the oxygen dissociation barrier on both graphene and N doped graphene surface are determined as 2.39 eV and 1.20 eV respectively shown in Figure 2.4. After the introduction of nitrogen on the graphene, the oxygen dissociation energy halves but still both the values are beyond surmountable at room temperature.[7] So, the four electron ORR proceeds through associative ORR mechanism in case of heteroatom doped carbon based catalyst.
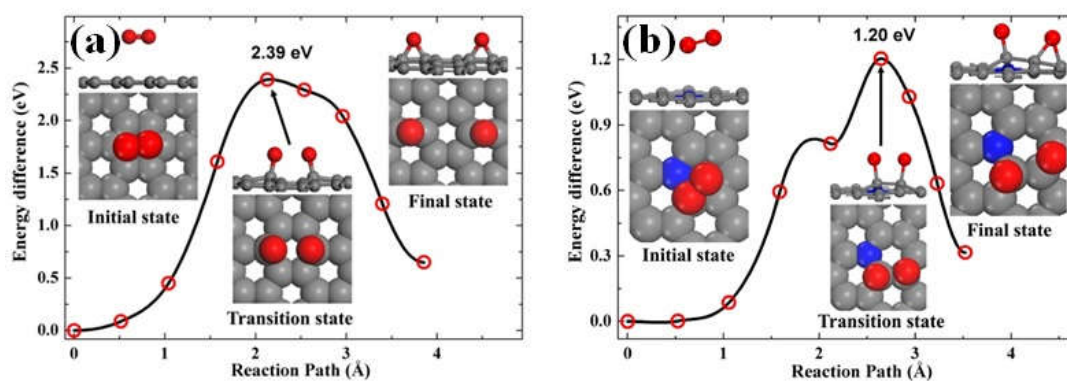
Figure 2.4: The optimized O_2 molecule dissociation reaction path and energy profile along the optimized dissociation reaction path at **(a)** graphene surface and **(b)** N-doped graphene surface.[7](Copyright 2012 American Institute of Physics)

The associative 4e[-] ORR mechanisms of the different heteroatom such as boron, nitrogen, sulfur, oxygen, phosphorus doped graphene at the equilibrium potential $U_0 = 0.455$ V vs NHE are illustrated on a free energy diagram as presented in Figure 2.5. The diagram revealed that nitrogen- and boron-doped graphene models (gN-G and gB-G) exhibit the lowest overall reaction free energy change at the equilibrium potential and showed better ORR performance in both theoretical and experimental viewpoints.[7-9]
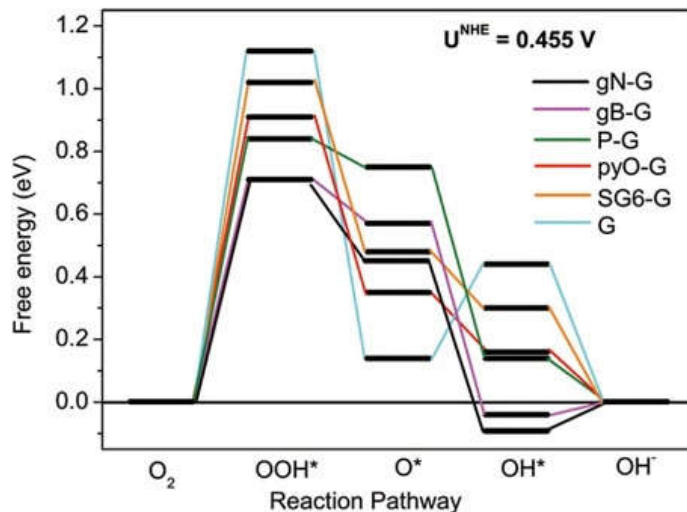
Figure 2.5: Free energy diagram of different heteroatom-doped graphene surfaces at the equilibrium potential $U_0 = 0.455$ V vs NHE.[7] (Copyright 2014 American Chemical Society)

From the above diagram, if the N doped graphene (gN-G) cluster model is considered as an example (black line), it is observed that the first electron transfer step to form OOH* is an endothermic reaction with a free energy change $\Delta G_{eq}(U_0) = 0.70$ eV, but the next following second and third electron transfer step to form chemisorbed O* and OH* respectively are all exothermic with $\Delta G_{eq}(U_0)$ values of −0.25 eV and −0.54 eV respectively. And the free energy difference $\Delta G_{eq}(U_0) = 0.09$ eV for final electron transfer step involving OH* desorption is easily achievable. So, the largest free energy changes of all four reaction steps is the formation of OOH* and it is considered as the rate limiting step. This step is responsible for the sluggish kinetics of ORR. All the other heteroatom-doped graphene models followed similar trend, indicating that the ORR rate-determining step for these catalysts is the same. In practical synthesis, each heteroatom dopant in graphene can result in several different cluster configurations which will have their own reaction pathways. However, the above diagram

represents only the best model with the lowest overall reaction free energy change among all the investigated cluster models for each dopant.[7]

For pure graphene model, two carbons located at the middle and the edge of the basal plane of graphene are named as G-M and G-E respectively and are evaluated as ORR active sites as shown in Figure 2.6 (a). Among the two types of carbon, G-E having lower energy barrier at U_0, showed more ORR activity in comparison to G-M. The ORR pathway in case of G-M involved two large energy barriers which matched the experimentally determined energy barriers by Yuan *et al.*[10] Since all the carbons are saturated by sp^2 bonding and evenly distributed π bonding over the plane, so G-M was ORR inactive as the reaction intermediates cannot bond to the graphene surface. However, the reaction intermediates OOH^*, O^* and OH^* can chemisorb on the G-E model as depicted in Figure 2.6 (b-d) unlike the G-M model and ease the ORR. So, G-E model is more ORR active than G-M model .[7]

Figure 2.6: (a) Free energy diagram at U_0 (solid lines) and experimentally observed $U_G^{onset} = 0.145\ V\ vs\ NHE$ (dash lines) for G-E (gray) and G-M (blue). **(b-d)** Reaction intermediates on G-E and **(e-g)** G-M. Green, red and white represent carbon, oxygen, and hydrogen respectively.[7] (Copyright 2014 American Chemical Society)

Three different models of N-graphene such as central graphitic nitrogen (gN-G) and edge pyridinic (pdN-G) and pyrrolic N (prN-G) in the graphene plane were investigated. Among them, gN-G showed the most ORR activity due to its overall lowest energy barrier of 0.70 eV at U_0. This value dropped further to 0.26 eV at experimentally observed onset potential of $U_G^{onset} = 0.145\ V\ vs\ NHE$ demonstrated in Figure 2.7 (a). On both the gN-G and prN-G models, the nitrogen is not considered as the ORR active site, but the carbon next to gN-G and prN-G are reported as ORR active sites by several researchers and is also shown in the Figure 2.6 (b-g). [11-13] In case of gN-G, the free energy of chemisorption of the reaction intermediates OOH^* on N atom is 1.02 eV, which is much higher than the carbon atom next to it, so it is not considered as ORR active site. Similarly, for prN-G, the chemisorption of OOH and OH on the N atom of the catalyst requires larger free energy and N is not the ORR active site. However, for pdN-G oxygen can be activated via direct bonding with the lone pair electrons of N and thus N is considered as the ORR active sites shown in Figure (h-j).[7]
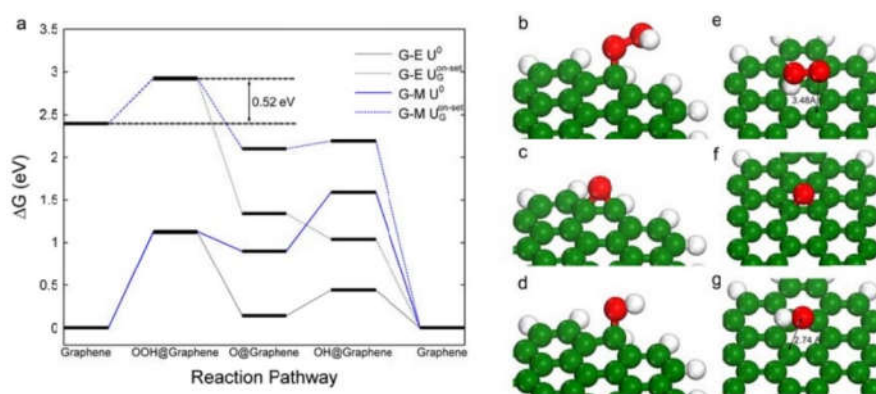

Figure 2.7: (a) Free energy diagram at U_0 (solid lines) and experimentally observed $U_G^{onset} = 0.145\ V\ vs\ NHE$ (dash lines) for gN-G (gray), prN-G (blue), and pdN-G (magenta). **(b-d)** Reaction intermediates on gN-G, **(e-g)** prN-G and **(h-j)** pdN-G. Green, red, blue and white represent carbon, oxygen, nitrogen and hydrogen respectively.[7] (Copyright 2014 American Chemical Society)

Two different models of S doped graphene such as C-S-C type (SC6-G) and thiophene type S (SC5-G) were studied to determine the ORR active site. In case (SC6-G) model, the doped S atom (S), the carbon next to the sulfur (C1) and the carbon which is second neighbor of doped sulfur (C2) were evaluated on the basis of ORR activity. Among these three sites, C1 displayed the lowest overall energy barrier and the OOH* adsorption almost halved (dropped from 1.02 eV to 0.51 eV) when the electrode potential shifts from equilibrium potential to onset potential. Thus, C1 served as the ORR active sites in SC6-G model and allowed effective ORR as shown in Figure 2.8 a and (b-d). The similar active sites as mentioned above were also studied for SC5-G model. The free energy involved in adsorption of OOH are 1.15 eV for S, 1.97 eV for C1 and 1.25 eV for C2. Even though S has the lowest OOH adsorption free energy at equilibrium potential, OOH cannot chemisorb on the S atom and is thus not considered as ORR active sites. Instead, the second neighboring C to sulfur dopant (C2) is considered as the most ORR active sites in comparison to S and C1, the reaction intermediates are depicted in Figure 2.8 (e-g).[7]
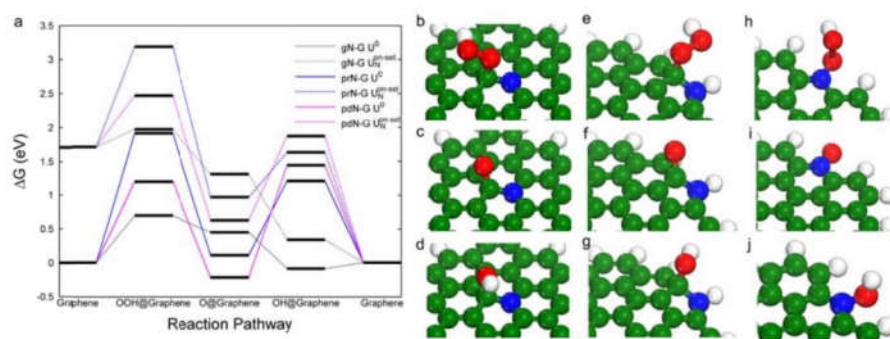

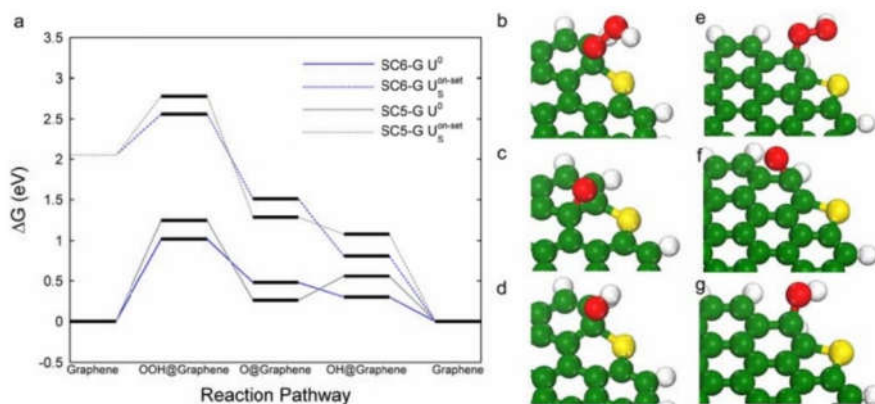**Figure 2.8: (a)** Free energy diagram at U_0 (solid lines) and experimentally observed $U_G^{onset} = 0.145\ V\ vs\ NHE$ (dash lines) for SC6-G (blue) and SC5-G (gray) respectively. **(b-d)** Reaction intermediates on SC6-G and **(e-g)** SC5-G. Green, red, yellow and white represent carbon, oxygen, sulfur and hydrogen respectively.[7] (Copyright 2014 American Chemical Society)

Dual doped graphene such as boron and nitrogen co doped graphene (B/N)[12, 14-17], sulfur and nitrogen (S/N)[18-20], phosphorus and nitrogen (P/N)[21, 22] or triple doped graphene such as nitrogen, boron and phosphorus (N/B/P)[23], nitrogen, sulfur and phosphorus (N/S/P)[24] were investigated and these showed better ORR activity in comparison to singly doped graphene. Several DFT calculations revealed that the origin of this ORR activity enhancement is due to the synergistic effect between the two or more different dopant elements. It is difficult to observe this synergy within graphene matrix through direct experimental observation, but, theoretical analysis indicated that dual dopants can tailor the electron-donor properties of nearby carbon atoms facilitating the adsorption of reaction intermediates.[12]

Among all these dual dopants, S/N co-doped graphene displayed the best electrocatalytic activity for both the ORR and hydrogen evolution reaction (HER). Two researchers synthesized S and N doped graphene via high temperature thermal treatment of either a single precursor (e.g., thiourea) or two precursors (e.g., melamine and benzyl disulfide) with graphene oxide.[18, 20] Higgins *et al.* explained the synergy of sulfur and nitrogen dual doping by the following three factors.[25]

i.   The dopant species modify the electronic properties of carbon and activate a larger number of carbon atoms creating an increased number of active sites.

ii. Dopants also increase the charge and spin densities of the atoms providing a higher intrinsic ORR activity. DFT calculations revealed that the C atoms adjacent to the N atoms in S/N co doped graphene lattice had higher spin density, while the C atoms bonded to S atoms had a relatively smaller spin density.[18]

iii. Moreover, when S-dopants in the form of five-fold coordinated thiophenic arrangement is incorporated in the graphene, it disrupts the graphene lattice, and thus, increases the number of electrocatalytically ORR active edge sites.

2.4 ORR mechanism on non-precious metal M-N-C catalyst

The selectivity of ORR with respect to either two or four electron reduction pathways for ORR is considered as an important parameter for the viability of the catalyst. In case of two electron ORR, H_2O_2 is produced as the product which is corrosive to the fuel cell system. To determine the selectivity of catalyst, the yield of H_2O_2 and electron transfer number (n) is measured by rotating ring disk voltammetry and rotating disk voltammetry and applying Koutecky-Levich equation. Recently, hydrogen peroxide reduction reaction (HPRR) on Fe-based non-precious metal ORR catalyst was investigated by Muthukrishnan *et al.* and they reported that significant HPRR activity occur at similar potentials to those typically applied to study the ORR.[26] This group suggested that the Damjanovic model[27] describing direct 4e$^-$ ORR pathway might also include a significant contribution from the 2e$^-$ reduction of O_2 to form H_2O_2 within the catalyst. This H_2O_2 will undergo subsequent reduction to H_2O without ever generating a free H_2O_2 species on the catalyst surface or in solution. Therefore, Muthukrishnan *et al.* developed another model including both surface and matrix-adsorbed H_2O_2 species based on the previous Damjanovic method. Both the models are illustrated in Figure 2.9.

In order to understand the ORR mechanism on Fe–N–C catalysts, Muthukrishnan *et al.* studied the role of Fe in the reduction of H_2O_2 intermediate by comparing the H_2O_2 reduction activity of Fe-free (PI) and Fe containing (Fe/PI) polyimide-based catalysts. Their results suggested that the Damjanovic method assumed the contribution of the direct 4e$^-$ ORR pathway neglecting the contribution of the 2 x 2e$^-$ pathway in determining the selectivity of ORR catalysts.
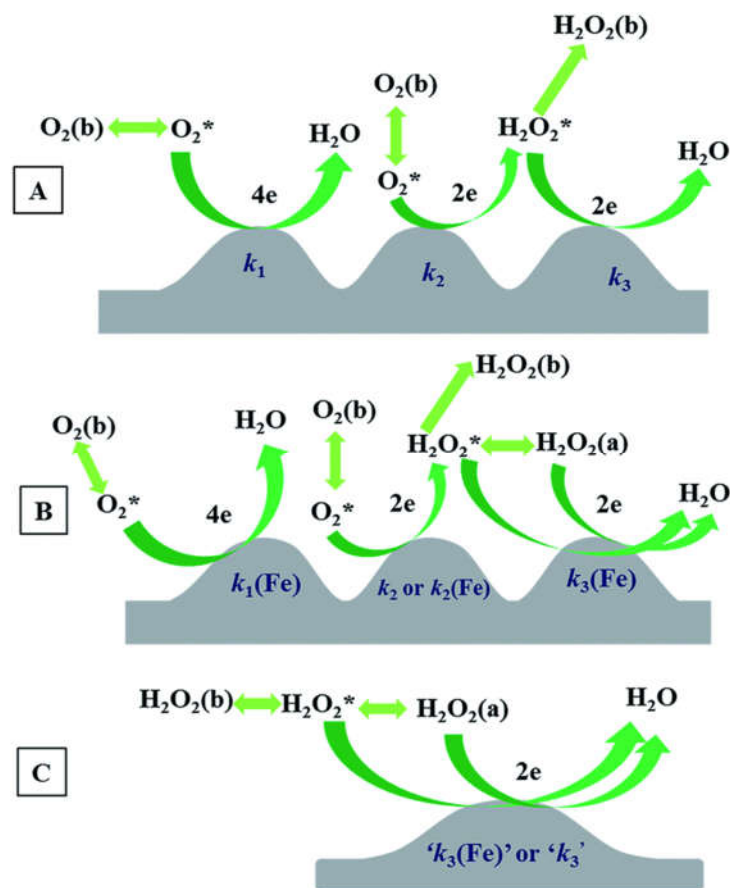
Figure 2.9: Schematic illustration of **(A)** ORR mechanism proposed by Damjanovic *et al.*, **(B)** ORR mechanism of the Damjanovic model type including the contribution of H_2O_2 (a) in the ORR and **(C)** hydrogen peroxide reduction mechanism including H_2O_2 (a) species. Indices b, * and a represent the bulk species, the species in the vicinity of the catalyst surface and the adsorbed species, respectively. k_i and k_i (Fe) (i = 1, 2 and 3) correspond to the rate constants at the Fe-free PI (polyimide) and Fe/PI catalysts, respectively. 'k_3' and 'k_3 (Fe)' represent the rate constants for the H_2O_2 reduction on the Fe-free PI and Fe/PI catalysts, respectively.[26] (Copyright 2016 The Royal Society of Chemistry)
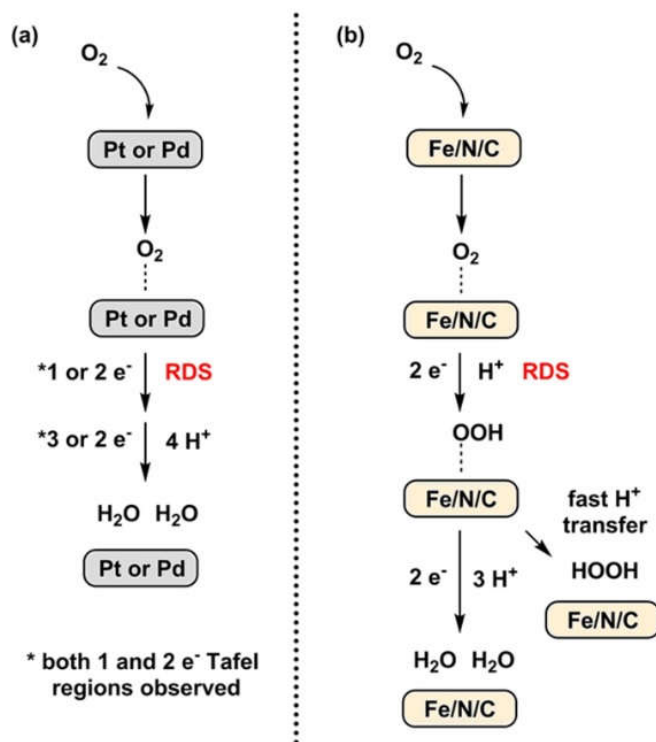
Figure 2.10: Possible mechanisms for the ORR on **(a)** precious metal and **(b)** non-precious-metal materials. Rate determining step (RDS) is shown in red.[28] (Copyright 2016 American Chemical Society)

In order to determine the role of proton in the ORR mechanism on non-precious metal-based catalyst, Tse *et al.* replaced protons (H^+) with deuterons (D^+) and applied the kinetic isotope effect (KIE). Their group conducted linear sweep voltammetry in protio and deutero solutions using three different ORR catalyst from Pt, Pd, and Fe and obtained the kinetically limited current densities using Koutecky-Levich (K-L) equation. Then the inherent electrochemical rate constants derived from this K-L analysis were compared for both the solutions. From the obtained results, Pt and Pd displayed no change in the rate constants which suggest the rate-determining step of the ORR on these surfaces is independent of the proton

transfer step. In case of the non-precious metal-based catalyst, they KIE of 2 was observed which the proton transfer step is the rate determining step in the ORR mechanism. To further elucidate the role of proton in ORR, rotating disk voltammetry was performed on NPM catalysts in H_2SO_4 and D_2SO_4solutions. It was observed that the rate of ORR was much slower in D_2SO_4 compared to H_2SO_4 with reduced amount of hydrogen peroxide formation. These results justified that proton transfer plays an important role in determining the activity and selectivity of NPM catalysts as shown in Figure 2.10 but do not affect the ORR activity of Pt or Pd catalysts.[28]

2.5 ORR kinetics

Generally, Butler−Volmer equation can be used to describe the kinetic current overpotential relationship of the ORR that occurs on electrode surfaces. Since the overpotential (η) of ORR in real condition is relatively large, so the backward reaction is considered negligible and the Butler−Volmer equation becomes:

$$j_k = j_o \, e^{n\alpha F\eta/RT}$$

where j_k is the kinetic ORR current density, j_o is the exchange current density which represents the current density of the forward reaction equal to that of the backward reaction at equilibrium, n is the number of electrons transferred in the rate determining step (rds), α is the electron transfer coefficient (always 0.5−1 for the ORR), F is the Faraday constant, R is the gas constant, and T is the temperature in Kelvin. [29]

On the basis of the above equation, the plot of η vs log (j_k) should provide a linear relationship with a slope called the Tafel slope.

$$\text{Tafel slope} = 2.303 \, RT/\alpha nF$$

Two options are available in order to obtain a high j_k at a certain value of η are either the j_o should be large and/or the value of the Tafel slope should be small. According to the simple microkinetic model developed by Nørskov $et\ al.,$[5] the value of j_o is related to the adsorption energetics of a series of reaction intermediates.

$$j_o = nFk^0 C_{total} \left[(1 - \theta)^{1-\alpha}\, \theta^\alpha \right]$$

where k^0 is the standard rate constant, C_{total} is the total number of active sites, and coverage of surface adsorbates and θ is a quantity related to the highest free energy change of the whole reaction as:

$$\theta = \frac{C_R}{C_{total}} = \frac{K}{1+K}$$

where the equilibrium constant K is related with the free energy change (ΔG) for the rds:

$$K = \exp\left(\frac{\Delta G}{k_B T}\right)$$

where k_B is the Boltzmann constant.

Depending on the electrode material and applied potential in ORR, two values of Tafel slopes are obtained, 60 and 120 mV/dec, respectively. Both these values have their own significance, the lower Tafel slope value reflects that the rds of ORR is a pseudo two-electron reaction, on contrary the higher value indicates the first-electron reduction of oxygen being the rds.[30, 31]

2.6 Different Measurement techniques to evaluate ORR

2.6.1 Surface area measurements

The specific surface area and porosity can significantly affect the catalytic performance of the synthesized materials. Higher surface area allows better mass transfer of the electrolytes, reaction intermediates and products, effectively removing the products from the active site and bringing more reactants to the sites and thereby, allowing frequent interaction between substrates and the active sites. In addition, the size of the pore in porous materials also controls the catalytic activity, micro pore size in particular can increase the surface area and also allow formation of ORR active sites.[32] Usually, both the parameters i.e. surface area and pore size can be determined from gas adsorption isotherms. The isotherms represent the adsorption of an adsorbate such as N_2 gas on the surface of a solid in a constant temperature. By determining the amount of adsorbed gas on the surface of the synthesized materials, the surface area of materials can be estimated.

Prior to collecting isotherms, the materials undergo outgassing which is done by heating the solid sample in a cell under vacuum. This process removes all of the physisorbed species from the surface of the adsorbent without changing the surface or the solid structure of the materials.[33] After that, the cell containing the sample is brought to room temperature and backfilled with helium gas and connected to the autosorb analyzer. Then the cell is submerged in a liquid bath to provide a constant temperature during the measurement of surface area. The collected gas isotherms display the amount of gas adsorbed on the surface of the sorbent as a function of relative pressure. The gas isotherms for porosity measurement are usually obtained at pressure range of $10^{-6} \sim 1$ bar.

The adsorption isotherms are obtained by charging successively increased amounts of a known gas. The successive addition of the gas to the cell is done automatically by the

instrument. The amount of gas adsorbed at a particular temperature in order to achieve desired pressure can be calculated by applying gas law while considering the pressure change, void volume of the cell and mass of the adsorbents. Initially a small amount of gas is introduced by the instrument into a confined calibrated sample containing cell and then adsorption occurs, reducing the pressure in the cell until the equilibrium is established. Then this dosing process is continued until the desired pressure is achieved. Then the total amount of gas introduced to the cell for that particular pressure will be recorded by the instrument. In order to complete the adsorption isotherm, this dosing process will be repeated for each desired pressure. After adsorption is completed, desorption starts in order to remove the adsorbed gas from the surface of the material. The instrument applies vacuum to the sample containing cell in a stepwise manner while recording the volume of the desorbed gas at each pressure in order to generate a desorption curve. So, this approach can be used to measure the gas uptake capacity of porous sorbent at desired temperature.

Initially, each gas molecule occupies an adsorption site on the surface of the material forming a monolayer of gas. On top of this layer, another layer of gas molecules form and this build of layers continues forming multiple layers of gas.[34] Typically argon and nitrogen gas display this multilayer adsorption behavior at cryogenic temperature. By calculating the number of gas molecules adsorbed on the surface of the adsorbent material, the specific surface area can be obtained. Initially, the monolayer capacity i.e. the amount of gas required to form a monolayer on the surface of a solid material is determined. Then this monolayer capacity is multiplied by the area occupied by each gas molecule to calculate the surface area.

Two different models (Langmuir and BET models) are generally used to assess the surface area of solid materials. used for assessment of surface area of solid materials.[35] The Langmuir model is based on three assumptions which are stated below:

i.   Adsorbed gas molecules do not interact with each other

ii.   All adsorbate molecules follow same adsorption mechanism

iii.   Adsorbates form a monolayer of gas molecules and do not form multi layers

But these assumptions are not met in reality since gas molecules usually interact with each other forming multi layers. This causes difference in adsorption mechanism in both early and final stage of the adsorption. Hence, Langmuir model overestimates the measured surface areas of solid materials. That's why another group of researchers (Brunauer, Emmett, and Teller) developed BET model to effectively determine surface area of solid materials. Since this group considered multilayer formation of adsorbed gas, it provided more realistic results in comparison to Langmuir model.[34]

Gas isotherms can also provide insights to the pore sizes of the porous material. Due to the difference in adsorbate-sorbent as well as adsorbate-adsorbate interactions, different pore size results in different types of isotherms. In general, two different models such as Barrett-Joyner Halenda (BJH) and Non-Local Density Functional Theory (NLDFT) models used to determine pore size distribution in the porous materials.[36] The collected isotherms are fitted into these models to measure the pore size. Among these two models, NLDFT is mostly used as it does not underestimate the pore size unlike BJH model.

2.6.2 Cyclic Voltammetry

To study the oxygen reduction reaction, cyclic voltammetry (CV) is considered as the most viable technique as it can provide easily interpretable and qualitative information about the reaction. Typically, CV is carried out in a three-electrode setup consisting of Pt wire as counter electrode, Ag/AgCl as reference electrode and glassy carbon with deposited catalyst on it as working electrode in an unstirred analyte containing electrolyte. The counter electrode (auxiliary electrode) is used only to complete the circuit in the electrochemical cell. It does not take part in the electrochemical reaction. The factors that influence the choice of counter electrodes are that the material for the electrode must be inert and should have large surface area than working electrode so that it does not limit the kinetics of the electrochemical reactions. The reference electrode is a half-cell with known reduction potential and is used to control the potential of the electrochemical cell. In addition, it acts as a point of reference in measuring potential at the working electrode. The working electrode is made of inert material and catalyst is usually loaded on its surface. The reaction of interest in an electrochemical system occurs on the working electrode which facilitate the transfer of charge between catalyst and oxygen in the electrolyte.

CV is performed by cycling the applied potential on a working electrode linearly from an initial value to a predetermined limit (also called the switching potential). Once the applied potential reached the switching potential, the direction of the scan is reversed. A typical cyclic voltammogram is shown in Figure 2.11.
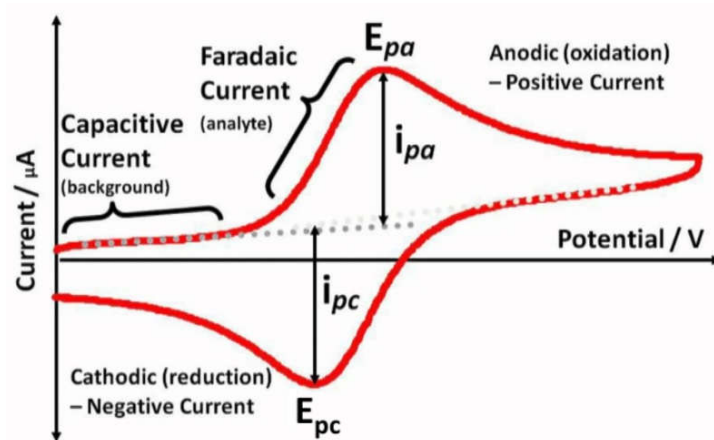
Figure 2.11: Typical cyclic voltammogram illustrating different parameters.

CV measures the current generated on the working electrode when the applied potential is cycled between a range of potential. As the initial potential is increased to a more positive value, the anodic current increases gradually due to the oxidation of the analyte followed by a decay in the same manner. Since CV is carried out with stationary working electrode in an unstirred solution, diffusion is the only mode of transport between the reactant and the catalyst deposited on working electrode. Slow diffusion cannot maintain a steady-state concentration profile at the same rate as the electrolysis depletes the reactant near the working electrode. As a result, a depletion zone is created and reactant molecules had to travel more distances to reach the catalytic surface. So, after reaching the anodic peak current (i_{pa}), the current cannot continue to increase exponentially with potential due to the mass transfer dependence and a finite rate for the reverse electron transfer process. As the concentration gradient starts to decrease, the rate of mass transfer also diminishes causing the peak current to decay gradually. Capacitive current i.e. current beyond i_{pa} is independent of the chemical reaction occurring at the working electrode and it either accumulates or removes charged species from the electrode or near the electrode.[37] Once the potential reaches the switching potential, the potential scan is reversed, reduction occurs reviving the oxidized species. The corresponding peak current and respective

potential are referred as cathodic peak current (i_{pc}) and cathodic peak potential (E_{pc}) as shown in Figure 2.11.
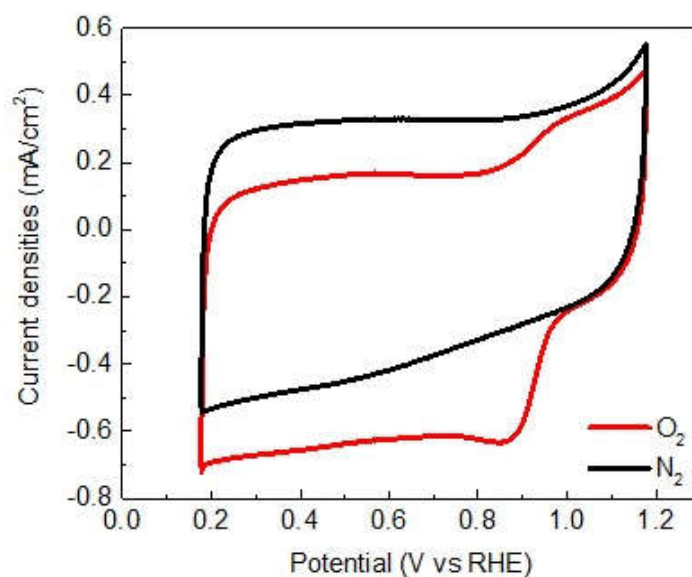

Figure 2.12: Typical cyclic voltammogram obtained in N_2 and O_2 saturated 0.1 M KOH to show the ORR activity.

At the beginning of the electrochemical testing procedures for ORR, the electrolytes were saturated with either nitrogen or ultra-high purity oxygen by bubbling the gas in the electrolyte for an hour and a continuous supply of either nitrogen or oxygen gases were maintained throughout the experiment in order to create a blanket over the solution. When CV was obtained in N_2 saturated electrolyte, the CV did not show any features except the capacitive current. However, when the electrolyte was saturated with O_2 it showed a typical cathodic ORR peak at around 0.9 V vs RHE displayed in Figure 2.12. This peak is due to the faradaic current resulting from the reduction of oxygen by the catalyst. Since oxygen reduction is an irreversible process, so CV does not provide much more information other than illustrating ORR activity with a cathodic peak current.

2.6.3 Rotating disk voltammetry and rotating ring disk voltammetry

Two experimental methods rotating ring-disk electrode (RRDE) method and the Koutecky−Levich (KL) method involving rotating disk voltammetry (RDE)) are widely used to determine the number of electrons involved in oxygen reduction. Both methods measure the current generated at the working electrode when the potential is swept between the working and reference electrode.

In rotating disk voltammetry, the working electrode is rotated at different rpm. This rotation creates particular flow pattern involving both convection and diffusion. According to Nernst diffusion layer model, [38] the two zones in the electrolyte near the electrode are:

i.   The region closest to the electrode surface with thickness δ is determined by assuming that there is a totally stagnant layer where diffusion is the only mode of mass transport

ii. The region near the first region is determined by assuming that transport of reactant molecules to the electrode surface occurs via convection and the concentration of reactant always remains the same.

Based on these stated assumptions, the limiting current density for the voltammogram is expressed as:

$$\frac{1}{J} = \frac{1}{J_L} + \frac{1}{J_K}$$

$$= 1/B\omega^{1/2} + 1/J_K$$

$$B = 0.2nFC_o(D_o)^{2/3}\,\upsilon^{-1/6}$$

where J = Measured current density, J_K = Kinetic current density, J_L = Diffusion limiting current density or Levich current density due to the influx of reactant species A at the

outer boundary of the film., ω = Rotation per minute, n = Transferred number of electrons, F= Faraday's constant, C_o = Bulk concentration of O_2, D_o = Diffusion coefficient of O_2, v = Kinematic viscosity, k = Electron transfer rate constant.

The kinetic current density represents the limit for rotation at an infinite rate assuming unlimited supply of reactants at the outer boundary of the structure.[39]

In case of RRDE, similar phenomenon occurs with an additional benefit. The ORR occurs at the disk and if H_2O_2 is produced during ORR, it can be directly oxidized by applying a constant potential on the ring. Due to this, the amount of H_2O_2 produced can be assessed along with the number of electrons involved in ORR. The equations involved in the calculations are as follows:

$$n_{e^-} = \frac{4I_D}{I_D + {I_R}/{N}}$$

where I_D is the disk current, I_R is the ring current and N is the collection efficiency.

The amount of H_2O_2 is calculated by the equation given below:

$$\%H_2O_2 = \frac{Total\ moles\ of\ peroxide\ produced}{Total\ moles\ of\ oxygen\ reacted} \times 100$$

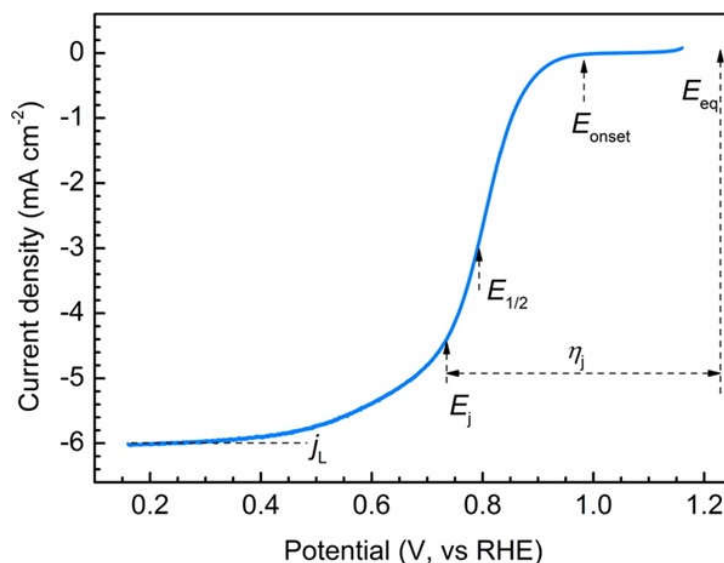$$\%H_2O_2 = \frac{2I_R}{I_D N + I_R} \times 100$$

Figure 2.13: Typical linear sweep voltammogram obtained using rotating disk voltammetry.

Different parameters which reflect the ORR activity can be determined from the linear sweep voltammogram obtained either by RDE or RRDE as shown in the above Figure 2.13. The onset potential E_{onset} is the potential at which ORR occur, the more positive the value is the better the catalytic performance. $E_{1/2}$ is the half wave potential obtained at the half of limiting current density, J_l. As discussed above, J_l value is used to calculate the number of electrons involved in ORR and thus determine ORR selectivity of the catalyst.

2.6.4 Amperometric i-t curve

Besides cyclic voltammetry and linear sweep voltammetry, chronoamperometry (CA) is also a popular technique to study electrochemical reactions. This technique can be used to evaluate the long-term durability and poison tolerance of the catalyst. In CA, current from faradaic processes due to the applied potential at the working electrode is recorded as a function

of time. In general, CA can be implemented either as a single potential step where the current due to forward step is only recorded or double potential step which involves increasing the potential form E_1 to E_2 and then returning the potential back to the E_1 after certain time period which is denoted by τ. This τ is also termed as pulse width/step time.[39] Both of these CA are depicted in Figure 2.14.
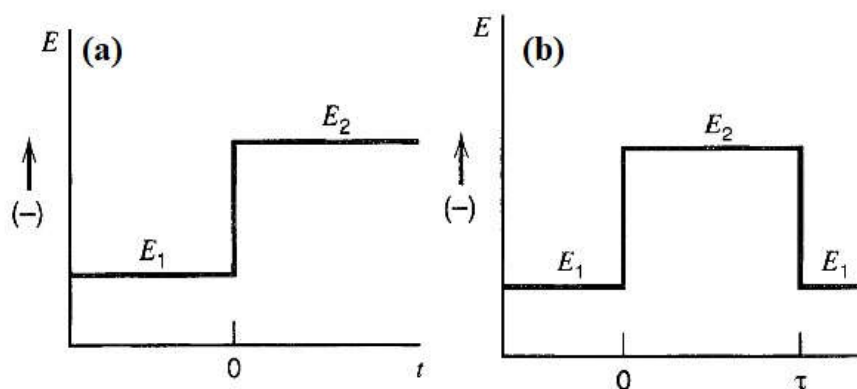

Figure 2.13: (a) Waveform for a step experiment when the reactant species is electroinactive at E_1 but is reduced at a diffusion limited rate at E_2 and **(b)** Typical waveform for double potential step.[39]

At the initial potential (E_1), no Faradaic reactions take place. When the potential is changed from E_1 to E_2, the oxidation or reduction of eletroactive species occurs causing the surface concentration of the species drop to zero. This potential is maintained for a step time while recording the current- time dependence. The mode of transport of reactive species to the electrode is solely governed by diffusion throughout this CA process. Due to this, the concentration of reactive species at the electrodes surface changes which is reflected current-time curve. With the depletion of reactive species, a diffusion layer starts to grow near the electrode causing a decrease in the concentration gradient as time progresses. This is reflected as the decrease in current with time and such plot is called amperometric i-t curve.

The observed current (planar electrode of infinite size) at any time following a large forward potential step in a reversible redox reaction (or to large overpotential) as a function of $t^{-1/2}$ can be expressed in CA by the Cottrell equation[39]:

$$I_L(t) = nFAD^{1/2}C(\pi t)^{-1/2}$$

where n = stoichiometric number of electrons involved in the reaction, F is the Faraday's constant, A is the electrode area, C is the concentration of electroactive species and D is the diffusion coefficient.

After applying potential step, another type of current originating from double layer charging is also observed. This current is only significant during the initial time period. However, it decays as a function of t^{-1}.[39]

2.7 References

1.   Dai, L. M.; Xue, Y. H.; Qu, L. T.; Choi, H. J.; Baek, J. B., Metal-Free Catalysts for Oxygen Reduction Reaction. *Chemical Reviews* **2015,** *115* (11), 4823-4892.

2.   Rossmeisl, J.; Qu, Z. W.; Zhu, H.; Kroes, G. J.; Norskov, J. K., Electrolysis of water on oxide surfaces. *Journal of Electroanalytical Chemistry* **2007,** *607* (1-2), 83-89.

3.   Rossmeisl, J.; Logadottir, A.; Norskov, J. K., Electrolysis of water on (oxidized) metal surfaces. *Chemical Physics* **2005,** *319* (1-3), 178-184.

4.   Kulkarni, A.; Siahrostami, S.; Patel, A.; Norskov, J. K., Understanding Catalytic Activity Trends in the Oxygen Reduction Reaction. *Chemical Reviews* **2018,** *118* (5), 2302-2312.

5.   Norskov, J. K.; Rossmeisl, J.; Logadottir, A.; Lindqvist, L.; Kitchin, J. R.; Bligaard, T.; Jonsson, H., Origin of the overpotential for oxygen reduction at a fuel-cell cathode. *Journal of Physical Chemistry B* **2004,** *108* (46), 17886-17892.

6.   Jiao, Y.; Zheng, Y.; Jaroniec, M.; Qiao, S. Z., Origin of the Electrocatalytic Oxygen Reduction Activity of Graphene-Based Catalysts: A Roadnnap to Achieve the Best Performance. *Journal of the American Chemical Society* **2014,** *136* (11), 4394-4403.

7.   Yan, H. J.; Xu, B.; Shi, S. Q.; Ouyang, C. Y., First-principles study of the oxygen adsorption and dissociation on graphene and nitrogen doped graphene for Li-air batteries. *Journal of Applied Physics* **2012,** *112* (10).

8.   Sheng, Z. H.; Gao, H. L.; Bao, W. J.; Wang, F. B.; Xia, X. H., Synthesis of boron doped graphene for oxygen reduction reaction in fuel cells. *Journal of Materials Chemistry* **2012,** *22* (2), 390-395.

9.   Yang, S. B.; Zhi, L. J.; Tang, K.; Feng, X. L.; Maier, J.; Mullen, K., Efficient Synthesis of Heteroatom (N or S)-Doped Graphene Based on Ultrathin Graphene Oxide-

Porous Silica Sheets for Oxygen Reduction Reactions. *Advanced Functional Materials* **2012,** *22* (17), 3634-3640.

10. Yuan, W. J.; Zhou, Y.; Li, Y. R.; Li, C.; Peng, H. L.; Zhang, J.; Liu, Z. F.; Dai, L. M.; Shi, G. Q., The edge- and basal-plane-specific electrochemistry of a single-layer graphene sheet. *Scientific Reports* **2013,** *3*.

11. Yu, L.; Pan, X. L.; Cao, X. M.; Hu, P.; Bao, X. H., Oxygen reduction reaction mechanism on nitrogen-doped graphene: A density functional theory study. *Journal of Catalysis* **2011,** *282* (1), 183-190.

12. Zheng, Y.; Jiao, Y.; Ge, L.; Jaroniec, M.; Qiao, S. Z., Two-Step Boron and Nitrogen Doping in Graphene for Enhanced Synergistic Catalysis. *Angewandte Chemie-International Edition* **2013,** *52* (11), 3110-3116.

13. Zhang, L. P.; Xia, Z. H., Mechanisms of Oxygen Reduction Reaction on Nitrogen-Doped Graphene for Fuel Cells. *Journal of Physical Chemistry C* **2011,** *115* (22), 11170-11176.

14. Kattel, S.; Atanassov, P.; Kiefer, B., Density functional theory study of the oxygen reduction reaction mechanism in a BN co-doped graphene electrocatalyst. *Journal of Materials Chemistry A* **2014,** *2* (26), 10273-10279.

15. Wang, S. Y.; Zhang, L. P.; Xia, Z. H.; Roy, A.; Chang, D. W.; Baek, J. B.; Dai, L. M., BCN Graphene as Efficient Metal-Free Electrocatalyst for the Oxygen Reduction Reaction. *Angewandte Chemie-International Edition* **2012,** *51* (17), 4209-4212.

16. Wang, J. M.; Hao, J.; Liu, D.; Qin, S.; Portehault, D.; Li, Y. W.; Chen, Y.; Lei, W. W., Porous Boron Carbon Nitride Nanosheets as Efficient Metal-Free Catalysts for the Oxygen Reduction Reaction in Both Alkaline and Acidic Solutions. *Acs Energy Letters* **2017,** *2* (2), 306-312.

17.   Xue, Y. H.; Yu, D. S.; Dai, L. M.; Wang, R. G.; Li, D. Q.; Roy, A.; Lu, F.; Chen, H.; Liu, Y.; Qu, J., Three-dimensional B,N-doped graphene foam as a metal-free catalyst for oxygen reduction reaction. *Physical Chemistry Chemical Physics* **2013,** *15* (29), 12220-12226.

18.   Liang, J.; Jiao, Y.; Jaroniec, M.; Qiao, S. Z., Sulfur and Nitrogen Dual-Doped Mesoporous Graphene Electrocatalyst for Oxygen Reduction with Synergistically Enhanced Performance. *Angewandte Chemie-International Edition* **2012,** *51* (46), 11496-11500.

19.   Qu, K. G.; Zheng, Y.; Dai, S.; Qiao, S. Z., Graphene oxide-polydopamine derived N, S-codoped carbon nanosheets as superior bifunctional electrocatalysts for oxygen reduction and evolution. *Nano Energy* **2016,** *19*, 373-381.

20.   Wang, X.; Wang, J.; Wang, D. L.; Dou, S. O.; Ma, Z. L.; Wu, J. H.; Tao, L.; Shen, A. L.; Ouyang, C. B.; Liu, Q. H.; Wang, S. Y., One-pot synthesis of nitrogen and sulfur co-doped graphene as efficient metal-free electrocatalysts for the oxygen reduction reaction. *Chemical Communications* **2014,** *50* (37), 4839-4842.

21.   Zhang, J. T.; Zhao, Z. H.; Xia, Z. H.; Dai, L. M., A metal-free bifunctional electrocatalyst for oxygen reduction and oxygen evolution reactions. *Nature Nanotechnology* **2015,** *10* (5), 444-452.

22.   Yu, D. S.; Xue, Y. H.; Dai, L. M., Vertically Aligned Carbon Nanotube Arrays Co-doped with Phosphorus and Nitrogen as Efficient Metal-Free Electrocatalysts for Oxygen Reduction. *Journal of Physical Chemistry Letters* **2012,** *3* (19), 2863-2870.

23.   Choi, C. H.; Park, S. H.; Woo, S. I., Binary and Ternary Doping of Nitrogen, Boron, and Phosphorus into Carbon for Enhancing Electrochemical Oxygen Reduction Activity. *Acs Nano* **2012,** *6* (8), 7084-7091.

24.   Razmjooei, F.; Singh, K. P.; Song, M. Y.; Yu, J. S., Enhanced electrocatalytic activity due to additional phosphorous doping in nitrogen and sulfur-doped graphene: A comprehensive study. *Carbon* **2014,** *78*, 257-267.

25.   Higgins, D.; Zamani, P.; Yu, A. P.; Chen, Z. W., The application of graphene and its composites in oxygen reduction electrocatalysis: a perspective and review of recent progress. *Energy & Environmental Science* **2016,** *9* (2), 357-390.

26.   Muthukrishnan, A.; Nabae, Y.; Ohsaka, T., Role of iron in the reduction of H2O2 intermediate during the oxygen reduction reaction on iron-containing polyimide-based electrocatalysts. *Rsc Advances* **2016,** *6* (5), 3774-3777.

27.   Damjanovic, A.; Genshaw, M. A.; Bockris, J. O., DISTINCTION BETWEEN INTERMEDIATES PRODUCED IN MAIN AND SIDE ELECTRODIC REACTIONS. *Journal of Chemical Physics* **1966,** *45* (11), 4057-+.

28.   Tse, E. C. M.; Varnell, J. A.; Hoang, T. T. H.; Gewirth, A. A., Elucidating Proton Involvement in the Rate-Determining Step for Pt/Pd-Based and Non-Precious-Metal Oxygen Reduction Reaction Catalysts Using the Kinetic Isotope Effect. *Journal of Physical Chemistry Letters* **2016,** *7* (18), 3542-3547.

29.   Jin, H.; Guo, C.; Liu, X.; Liu, J.; Vasileff, A.; Jiao, Y.; Zheng, Y.; Qiao, S.-Z., Emerging Two-Dimensional Nanomaterials for Electrocatalysis. *Chemical Reviews* **2018,** *118* (13), 6337-6408.

30.   Huang, J. H.; Chen, J. T.; Yao, T.; He, J. F.; Jiang, S.; Sun, Z. H.; Liu, Q. H.; Cheng, W. R.; Hu, F. C.; Jiang, Y.; Pan, Z. Y.; Wei, S. Q., CoOOH Nanosheets with High Mass Activity for Water Oxidation. *Angewandte Chemie-International Edition* **2015,** *54* (30), 8722-8727.

31.   Ge, X. M.; Sumboja, A.; Wuu, D.; An, T.; Li, B.; Goh, F. W. T.; Hor, T. S. A.; Zong, Y.; Liu, Z. L., Oxygen Reduction in Alkaline Media: From Mechanisms to Recent Advances of Catalysts. *Acs Catalysis* **2015,** *5* (8), 4643-4667.

32.   Jaouen, F.; Lefevre, M.; Dodelet, J. P.; Cai, M., Heat-treated Fe/N/C catalysts for O-2 electroreduction: Are active sites hosted in micropores? *Journal of Physical Chemistry B* **2006,** *110* (11), 5553-5558.

33.   Thommes, M.; Kaneko, K.; Neimark, A. V.; Olivier, J. P.; Rodriguez-Reinoso, F.; Rouquerol, J.; Sing, K. S. W., Physisorption of gases, with special reference to the evaluation of surface area and pore size distribution (IUPAC Technical Report). *Pure and Applied Chemistry* **2015,** *87* (9-10), 1051-1069.

34.   Brunauer, S.; Emmett, P. H.; Teller, E., Adsorption of gases in multimolecular layers. *Journal of the American Chemical Society* **1938,** *60*, 309-319.

35.   Gomez-Serrano, V.; Gonzalez-Garcia, C. M.; Gonzalez-Martin, M. L., Nitrogen adsorption isotherms on carbonaceous materials. Comparison of BET and Langmuir surface areas. *Powder Technology* **2001,** *116* (1), 103-108.

36.   Ojeda, M. L.; Esparza, J. M.; Campero, A.; Cordero, S.; Kornhauser, I.; Rojas, F., On comparing BJH and NLDFT pore-size distributions determined from N(2) sorption on SBA-15 substrata. *Physical Chemistry Chemical Physics* **2003,** *5* (9), 1859-1866.

37.   Mabbott, G. A., AN INTRODUCTION TO CYCLIC VOLTAMMETRY. *Journal of Chemical Education* **1983,** *60* (9), 697-702.

38.   Nikolic, J.; Exposito, E.; Iniesta, J.; Gonzalez-Garcia, J.; Montiel, V., Theoretical concepts and applications of a rotating disk electrode. *Journal of Chemical Education* **2000,** *77* (9), 1191-1194.

39.   Bard, A. J., *Electrochemical methods : fundamentals and applications / Allen J. Bard, Larry R. Faulkner*. Wiley: New York, 1980.

Chapter 3

Rapid Synthesis of Fe Based S and N dual doped Benzimidazole derived Porous Carbon for Efficient Electrocatalytic Oxygen Reduction Reaction

3.1 Abstract

In this work, an easy synthetic approach was followed to prepare iron-based sulfur and nitrogen dual doped porous carbon (Fe@SNDC). A cheap, commercially available monomer i.e. benzimidazole was used as a precursor for N doped carbon and calcined with potassium thiocyanate at different temperatures to tune the pore size, nitrogen content and different types of nitrogen functionality such as pyridinic, pyrrolic and graphitic. The Fe@SNDC–1–950 with high surface area, optimum N content of about 5 at% and high amount of pyridinic and graphitic N displayed an onset potential and half wave potential of 0.98 and 0.83 V vs RHE, respectively, in 0.1 M KOH solution. The catalyst also exhibits very good ORR performance in acidic media. Furthermore, when compared to commercially available Pt/C (20 wt.%), Fe@SNDC–1–950 showed excellent poison tolerance in case of methanol crossover, high durability and stability in oxygen saturated alkaline electrolyte. Our study demonstrates that the presence of N and S along with Fe-N moieties synergistically served as ORR active sites while the high surface area with a wide pore size distribution allowed for efficient mass transfer and interaction of oxygen molecule to the active sites contributing to the remarkable ORR activity of the catalyst.

3.2 Introduction

Currently, incorporation of nonprecious transition metal in carbon-based materials doped with either N [1-4] alone or dual doping with another element such as S [4-7] has garnered an overwhelming attention. This type of catalysts exhibited outstanding ORR performance due to the presence of effective ORR active sites. It has been suggested that ORR active centers originate from the doping atoms which alter the charge and spin densities of adjacent carbon atoms allowing for molecular oxygen adsorption.[8-10] In contrast, other studies have suggested metals coordinated to the N (M-N) are responsible for enhanced ORR performance.[3, 11] The ORR performance of nonprecious metal based catalysts outperformed those of metal-free N-doped carbon particularly in acidic electrolyte highlighting the role of M-N.[12-14] The addition of certain transition metals (e.g., Fe, Co) to the metal-free, nitrogen-doped carbon frameworks results in a nonprecious metal (NPM) catalyst system with improved ORR activity in acidic media.[3, 13-15] Most of these N or N and S dual doped NPM catalysts are moderately porous allowing efficient transfer of oxygen saturated electrolyte. However, to obtain the specific pore size and increased porosity, soft templates such as silica nanoparticle [13] or amphiphilic molecules [16] were used which require harsh treatment to remove the templates.

In this study, we have developed a simple and cost-effective synthetic procedure for Fe-based S and N dual doped porous carbon by calcining an inexpensive monomer, benzimidazole with iron (III) thiocyanate. This synthetic route is environment friendly as it eliminates the use of templates or any harsh solvent. By varying the calcination temperature, different properties such as surface area, pore size distribution, dopant content and types of N and S are controlled. The obtained catalyst shows an outstanding ORR performance in alkaline medium due to its high surface area, wide pore size distribution and multiple active sites for ORR. In addition, the presence of Fe–N moieties in the catalyst enables enhanced ORR activity

in acidic media. The superior long-term durability and excellent methanol tolerance of the synthesized catalyst in comparison to commercial 20wt% Pt/C catalyst indicate that Fe@SNDCs are promising cost-effective catalysts for future use in ORR.

3.3 Experimental Section

3.3.1 Materials and Methods

All chemicals were purchased from commercial suppliers (Alfa Aesar, Acros Organics, TCI America) and used without further modification. Initially, $Fe(SCN)_3$ was prepared by adding $FeCl_3$ (1.0 mL, 1.0 M) to a solution of KSCN (3.0 mL, of 1.0 M).[17] Benzimidazole was added to this solution followed by addition of distilled water (70 mL). The resultant mixture was stirred overnight and the solvent was then removed via rotary evaporation. The mixture was further dried in an oven for 12 hours at 80 °C. The resulting powder was carbonized at different temperatures starting from 850, 950 to 1050 °C in a temperature programmed tube furnace (Carbolite) at a ramp rate of 5 °C per minute under argon gas flow for an hour. The carbonized sample was allowed to cool to room temperature and then sonicated with 1.0 M HCl (10 mL) for 30 minutes then filtered on a medium glass frit and washed with 1.0 M HCl (3 x 50 mL). Finally, the resultant black powder was washed with excess distill water and ethanol. We denote the as-prepared catalyst as Fe@SNDC–X–Y, where X indicates the number of pyrolysis and Y indicates the pyrolysis temperature.

3.3.2 Physical Characterization

The Brunauer–Emmett–Teller (BET) method was used to calculate the specific surface area of the samples using N_2 isotherms at 77 K collected using Autosorb-iQ2 volumetric adsorption analyzer (Quantachrome Instruments). The pore size distributions (PSD) were obtained from the equilibrium branch of N_2 (77 K) isotherms by using quench solid density functional theory (QSDFT) model with the assumption that the carbon material has slit-pore geometry. Prior to any adsorption analysis, the samples were degassed at 200 °C for 12 h.

Hitachi SU-70 scanning electron microscope was used to obtain the scanning electron microscopy (SEM) images of the synthesized samples. The samples were prepared by dispersing each specimen onto the surface of a flat aluminum sample holder with silver paste. Then the samples were coated with platinum at a pressure of 1.0×10^{-5} bar in a N_2 atmosphere for 60s prior to SEM imaging. Elemental distribution was analyzed by collecting elemental mapping using energy-dispersive X-ray spectroscopy (EDX).

X-ray photoelectron spectroscopy (XPS) analysis was performed on a Thermo Fisher Scientific ESCALAB 250 spectrometer employing an Al Kα (1486.68 eV) X-ray source equipped with a hemispherical analyzer. Samples were prepared for XPS measurements by pressing the carbon specimen into a piece of indium foil, which was then mounted onto the sample holder using double-sided sticky tape. During XPS analysis, a combination of a low-energy electron flood gun and an argon ion flood gun was utilized for charge compensation. The binding energy scale was calibrated by setting the C 1s peak at 285.0 eV. XPS results were analyzed with the Thermo Avantage software (v4.84).

Powder X-ray diffraction (P-XRD) patterns of the dried samples were collected at room temperature on a Panalytical X'Pert Pro Multipurpose Diffractometer (MPD). The samples were mounted on a zero-background sample holder measured in transmission mode using Cu

Kα radiation with a 2θ range of 20 to 70. The Raman spectra were obtained using a Thermo Scientific DXR Smart Raman spectrometer operating at an excitation wavelength of 532 nm.

3.3.3 Electrochemical Characterization

The electrochemical measurements were conducted using a conventional three electrode setup with Ag/AgCl in 3 M KCl (reference electrode), glassy carbon electrode (working electrode) and Pt wire (counter electrode) in a Bipotentiostat (Model 760E Series, CH Instruments). The catalyst ink was prepared by ultrasonically dispersing 3.0 mg of the catalyst in a solution containing 25 μL of Nafion per fluorinated resin (5 wt %, Sigma-Aldrich) and 400 μL of isopropanol. About 10 μL of the catalyst ink was pipetted onto a polished glassy carbon electrode and dried in an oven for half an hour. The loading of the catalyst was 0.36 mg/cm^2. The electrochemical performance of the catalyst was compared to commercial Pt/C (20 wt % Pt on graphitized carbon, Sigma-Aldrich) with similar catalyst loading. The electrolytes for alkaline and acidic medium were 0.1 M KOH and 0.5 M H$_2$SO$_4$ respectively. At the beginning of the electrochemical testing procedures, the electrolytes were saturated with either nitrogen or ultra-high purity oxygen by bubbling the gas in the electrolyte for an hour and a continuous supply of either nitrogen or oxygen gases were maintained throughout the experiment in order to create a blanket over the solution.

According to Nernst equation, the measured potential vs Ag/AgCl (3M KCl) can be converted to the reversible Hydrogen electrode (RHE) scale following:

$$E_{RHE} = E_{Ag/AgCl} + 0.059\ pH + E^{\circ}_{Ag/AgCl} \quad (1)$$

where $E_{Ag/AgCl}$ is the experimentally measured potential vs Ag/AgCl, $E^{\circ}_{Ag/AgCl}$ is 0.210 V at 25 °C.

The ORR performance was evaluated by cyclic voltammetry (CV) in N$_2$ or O$_2$ saturated 0.1 M KOH and 0.5 M H$_2$SO$_4$ in a potential window 0 to 1.0 V vs RHE at varying sweep rates

from 5 to 50 mV. The ORR kinetics were evaluated by linear sweep voltammetry (LSV) at various rotations rates per minute ranging from 400 to 2500 rpm. The Koutecky-Levich equation was used to determine the number of electrons in oxygen reduction reactions.

$$1/J = 1/J_L + 1/J_K$$

$$= 1/B\omega^{1/2} + 1/J_K$$

$$B = 0.2nFC_o(D_o)^{2/3} v^{-1/6}$$

where J = Measured current density, J_K = Kinetic current density, J_L = Diffusion limiting current density, ω = Rotation per minute, n = Transferred number of electrons, F = Faraday's constant, C_o = Bulk concentration of O_2, D_o = Diffusion coefficient of O_2, v = Kinematic viscosity.

Rotating ring disk voltammetry (RRDE) was used to determine the apparent number of electrons (n_{e^-}) involved in ORR using the following equation:

$$n_{e^-} = \frac{4I_D}{I_D + {I_R}/{N}}$$

where I_D is the disk current, I_R is the ring current and N is the collection efficiency.

The collection efficiency of RRDE was measured using 10 mM potassium ferrocyanide in 1.0 M KNO_3 and calculated to be 0.36 as shown in Figure 3.18. The durability test of the catalyst was done using the chronoamperometric i-t technique at 0.88 V vs RHE in O_2 saturated 0.1 M KOH solution with a rotation of 1600 rpm for 12 hours. The methanol tolerance test was also evaluated by both cyclic voltammetry and chronoamperometric i-t technique with the introduction of 3 M methanol solution.

3.4 Results and Discussion

3.4.1 Facile Synthetic route for heteroatom derived porous carbon

The Fe-based S and N co-doped porous carbon catalysts (Fe@SNDCs) were synthesized by thermolysis of iron(III) thiocyanate/benzimidazole mixtures at 850, 950, and 1050 °C under nitrogen as shown in Figure 3.1. Calcination temperatures played a significant role in controlling the dopant content and textural properties of Fe@SNDCs. As the calcination temperature was increased, the atomic percentage of heteroatoms decreased sharply (Table 3.2) and the type of nitrogen functionalities also changed from pyridinic to more graphitic as observed in deconvoluted N XPS spectra (Figure 3.7, 3.8, 3.9).
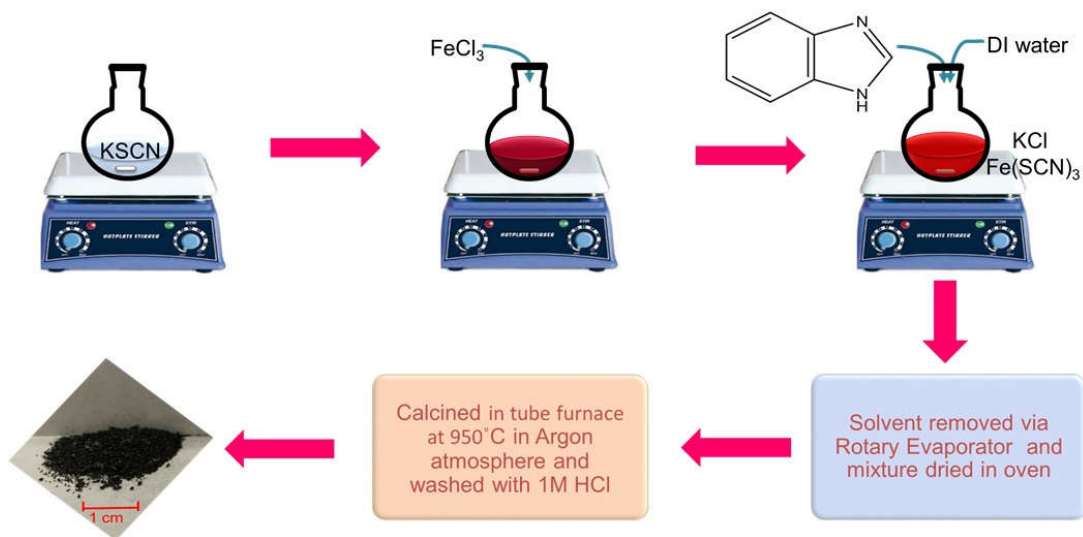
Figure 3.1: Facile synthetic route for Fe@SNDC–1–950 samples.
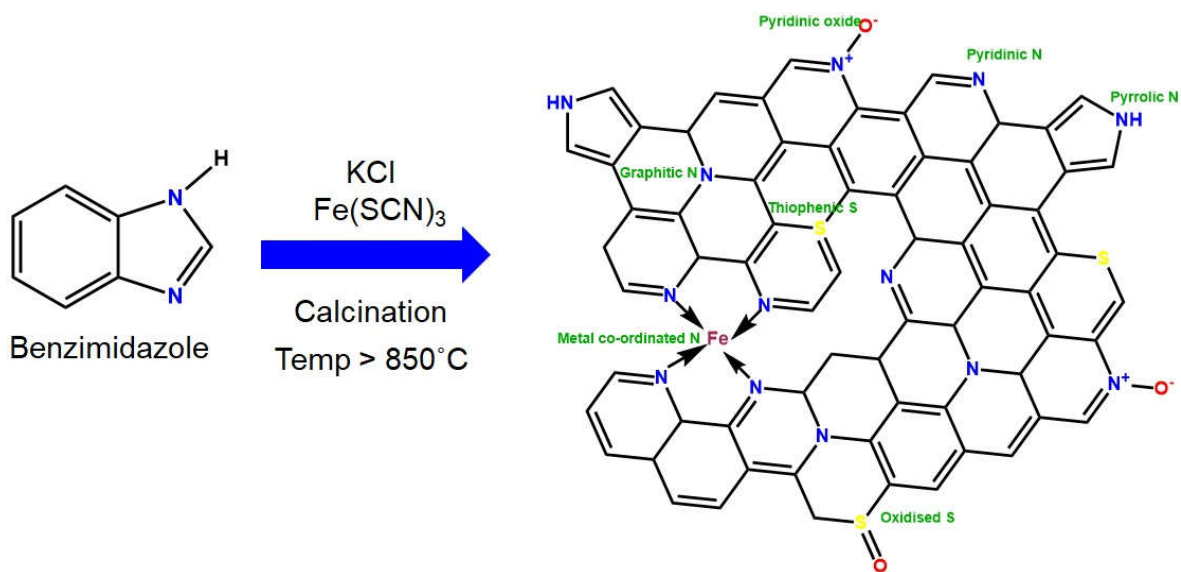
Figure 3.2: Proposed structure of Fe@SNDC samples

3.4.2 Physical Characterization of Fe@SNDC samples

The porosity of Fe@SNDCs was studied by N_2 adsorption and desorption measurements at 77 K (Figure 3.3). The isotherms of all the samples displayed a rapid uptake at very low relative pressures ($P/P_o < 0.01$) which suggest the presence of micropores. The isotherm of the sample calcined at 850 °C reached a plateau between P/P_o (0.1~0.9) which further confirmed the presence of micropore. However, the existence of mesopores in Fe@SNDC samples calcined at temperatures higher than 850 °C was noted due to a gradual increase in N_2 uptake beyond ($P/P_o > 0.1$). The BET surface areas of the Fe@SNDC calcined at 850, 950, and 1050 °C were calculated to be 1020, 1101, and 1157 m^2 g^{-1} respectively. Quenched solid state density functional theory (QSDFT) was used to determine the pore size distribution (PSD) as depicted in Figure 3.4. The two major peaks in PSD for all the samples were centered around 6 and 11 Å. Using single point N_2 uptake at $P/P_o = 0.95$, the total pore

volume was determined and found to be the highest for Fe@SNDC–1–950 (0.56 cm^3 g^{-1}) in comparison to other Fe@SNDC samples as summarized in Table 3.1. The high surface area and wide pore size distribution are important parameters that allow for facile mass transport through the pores and enhance the accessibility of catalytic sites.
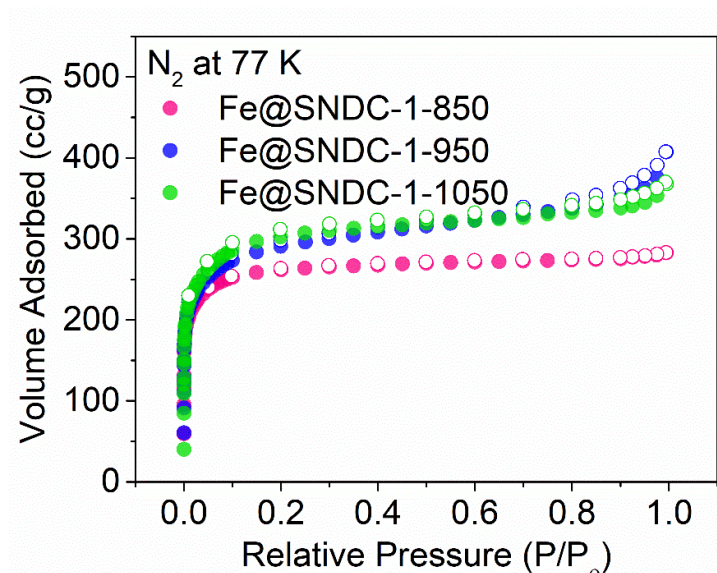

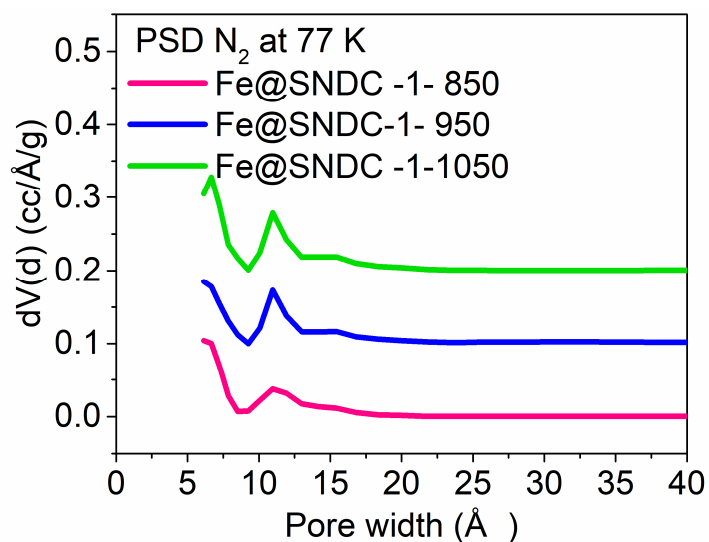**Figure 3.3:** Nitrogen isotherms at 77 K of Fe@SNDC–1–850, Fe@SNDC–1–950 and Fe@SNDC–1–1050.

Figure 3.4: Pore size distribution (PSD) from QSDFT using N_2 at 77 K (Figure 3.3). For clarity, PSD of Fe@SNDC–1–950 and Fe@SNDC–1–1050 are offset by 0.1 and 0.2, respectively.

Table 3.1: Surface area and pore volume of Fe@SNDCs.

Samples	Surface Area[a] (m^2 g^{-1})	Total Pore Volume[b] (cm^3 g^{-1})	Pore Size Distribution[c] (Å)
Fe@SNDC–1– 850	1020	0.43	
Fe@SNDC–1–950	1101	0.56	6-11
Fe@SNDC–1–1050	1157	0.54	

[a]BET surface area. [b]Total pore volume determined from single point N_2 uptake at P/P$_o$ = 0.95.

[c]Pore size distribution range calculated from quenched solid-state density functional theory (QSDFT).

The SEM images of Fe@SNDCs displayed fragmented sheet like morphologies (Figure 3.5) and the EDS elemental mapping survey showed uniform distribution of C, S, N, O and Fe throughout the porous structure in all samples (Figure 3.6).
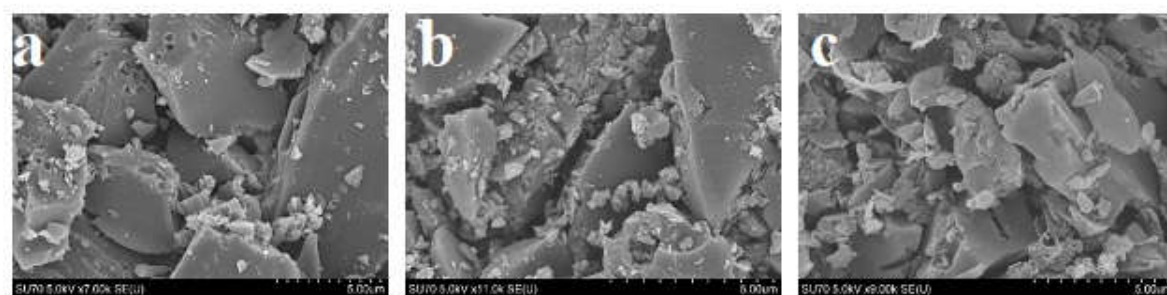
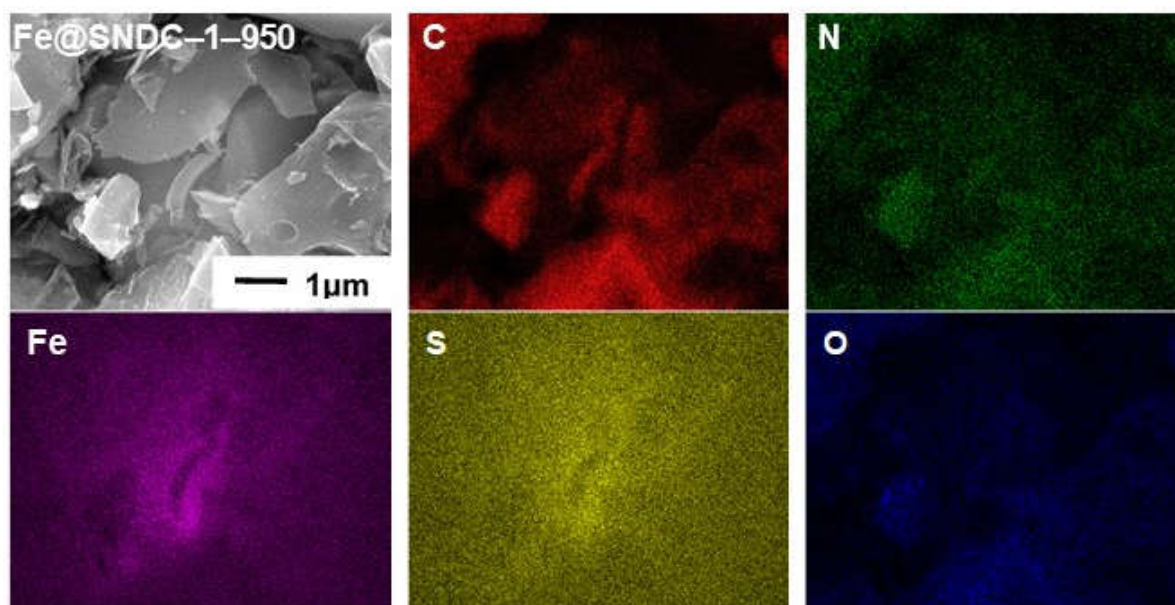**Figure 3.5:** SEM images of (a) Fe@SNDC–1–850, (b) Fe@SNDC –1–950 and (c) Fe@SNDC –1–1050.

Figure 3.6: SEM and EDX elemental mapping for Fe@SNDC–1–950; C: red, N: Green, Fe: purple, S: yellow, and O: blue.

To evaluate the chemical composition of Fe@SNDC samples, X-ray photoelectron spectroscopy (XPS) studies were performed. The XPS survey spectra of three samples calcined at different temperatures displayed three pronounced C 1s, N 1s and O 1s signals located at around 286, 400 and 533 eV respectively. The S 2p peak located at 170 eV was quite noticeable for Fe@SNDC–1–850 and Fe@SNDC–1–950. The XPS survey spectra (Figure 3.7) and the results are summarized in Table 3.2. The Fe peak at around 712 eV was visible for Fe@SNDC–1–850 but was very weak for the samples calcined at or above 950 °C. However, the coupled plasma optical emission spectrometry (ICP-OES) detected 20 ppm iron for Fe@SNDC–1–950 samples. For Fe@SNDC–1–850 and Fe@SNDC–1–1050 samples the iron content was only 6 ppm and 16 ppm respectively.
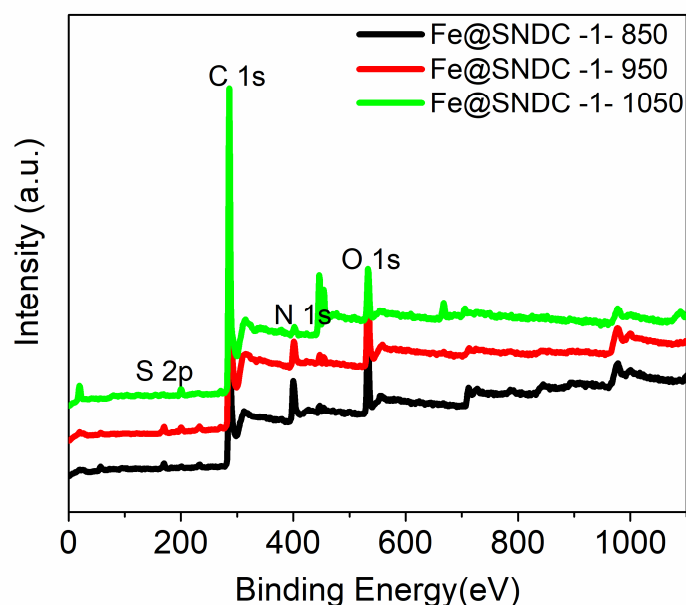
Figure 3.7: XPS survey spectra of the three FeBIDC samples.

Table 3.2: XPS survey spectra results.

Samples	C (At. %)	N (At. %)	O (At. %)	S (At. %)	Fe (At. %)
Fe@SNDC-1-850	76.8	9.81	10.68	1.32	1.21
Fe@SNDC-1-950	83.66	4.93	10.12	1.29	undetected
Fe@SNDC-1-1050	89.33	2.53	6.85	undetected	undetected

When the high-resolution spectrum of N 1s was deconvoluted (Figure 3.8, 3.9, 3.10), three peaks at 398.2 (pyridinic N), 400.3 eV (graphitic N) and 405.1 (pyridine N oxides) were observed.[18, 19] The pyridinic N can provide a pair of electrons to the π-conjugated system in the carbon structure and also act as metal co-ordination sites. The peak from nitrogen bound to iron is difficult to differentiate as its binding energy is very close to that of pyridinic N.[20] The deconvolution of S 2p spectra (Figure 3.8, 3.9, 3.10) also revealed three distinguished peaks located at 163.8 eV (−C−S−C− $2p_{2/3}$), 165.0 eV (−C−S−C−$2p_{1/2}$), and 168.7 eV (C−SO$_x$−C, X = 1, 2, 3) peaks.[17, 21-23] Fe@SNDC-1-950 sample was comprised of 21% of −C−S− and conjugated −C=S− bound which can efficiently promote ORR in alkaline media.[6]
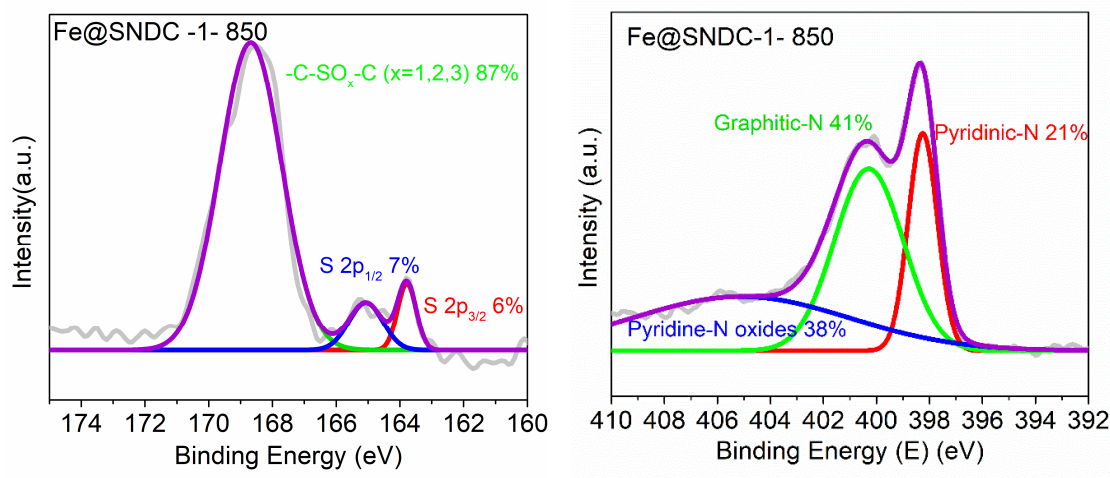
Figure 3.8: Deconvoluted S and N XPS spectra of Fe@SNDC–1–850.

The amount of N in Fe@SNDC–1–950 samples was around 5 at% but it served as better electrocatalyst for ORR compared to Fe@SNDC–1–850 (9.5 at%) and Fe@SNDC–1–1050 (2.5 at%). This suggested that the types of nitrogen in the porous carbon structure was more important than the amount of N for effective ORR performance. Among the different types of nitrogen, the pyridinic and graphitic N were recognized as the ORR active sites.[14] In case of graphitic N, nitrogen being more electronegative than C, it allows transfer of electrons from the adjacent C to N atom and N then returns the electrons to adjacent C. This overall donation and backdonation process aids the dissociation of oxygen molecule on adjacent C atom and also allows a strong chemical bond to form between O and C.[24] For pyridinic N, the oxygen molecules are adsorbed on carbon atoms next to pyridinic N with Lewis basicity.[25, 26] Both graphitic and pyridinic N-doped porous carbon have similar dissociative adsorption energies of oxygen.[24] Fe@SNDC–1–1050 which has the highest percentage of graphitic N and lowest percentage of pyridinic N (Figure 3.8) displayed inferior ORR performance compared to Fe@SNDC–1–950. This result suggested that an optimum amount of N content along with a proper balance between pyridinic (probably including the Fe-N moieties) and graphitic N are

required for effective electrocatalysis of ORR. The sulfur dopant further increases the ORR active sites by changing the atomic charge density and spin density of the neighboring C atoms which promotes the adsorption of oxygen and also weakens the O-O bonding thus enhancing ORR performance. [27-29]
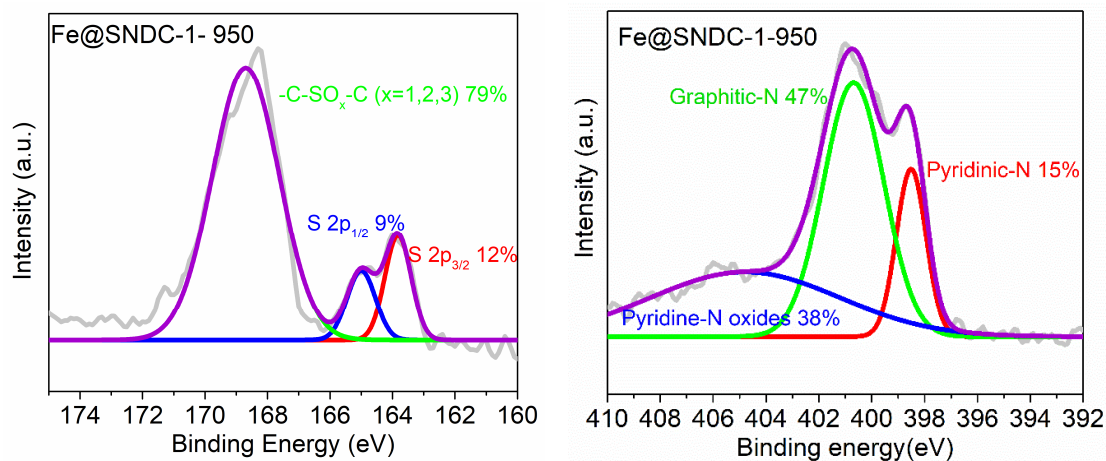

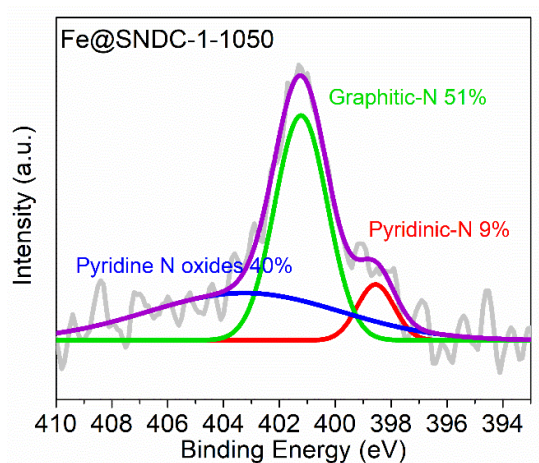**Figure 3.9:** Deconvoluted S and N XPS spectra of Fe@SNDC–1–950.

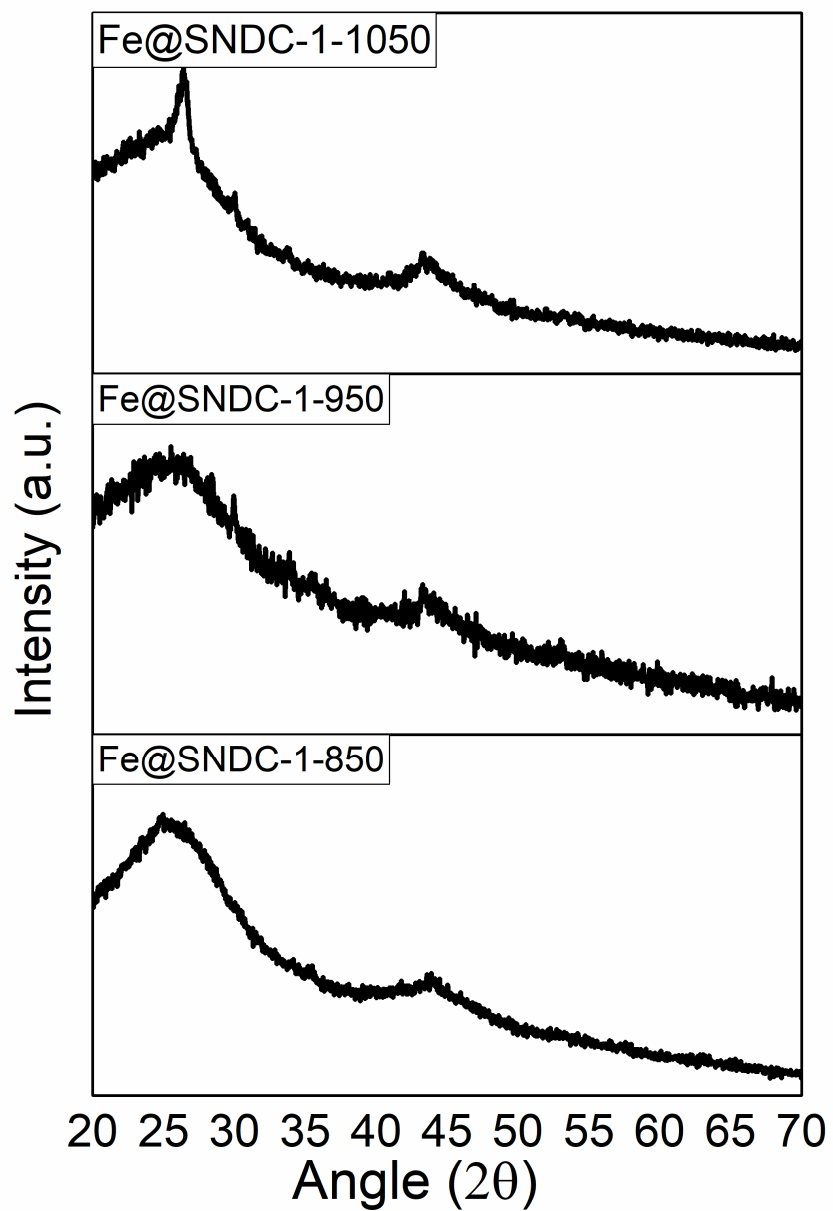**Figure 3.10:** Deconvoluted N XPS spectrum of Fe@SNDC–1–1050.

Figure 3.11: PXRD pattern of Fe@SNDC samples.

The PXRD patterns of the samples showed two characteristic peaks around 25° and 43° which are generally ascribed to the (200) and (100) planes of graphite.
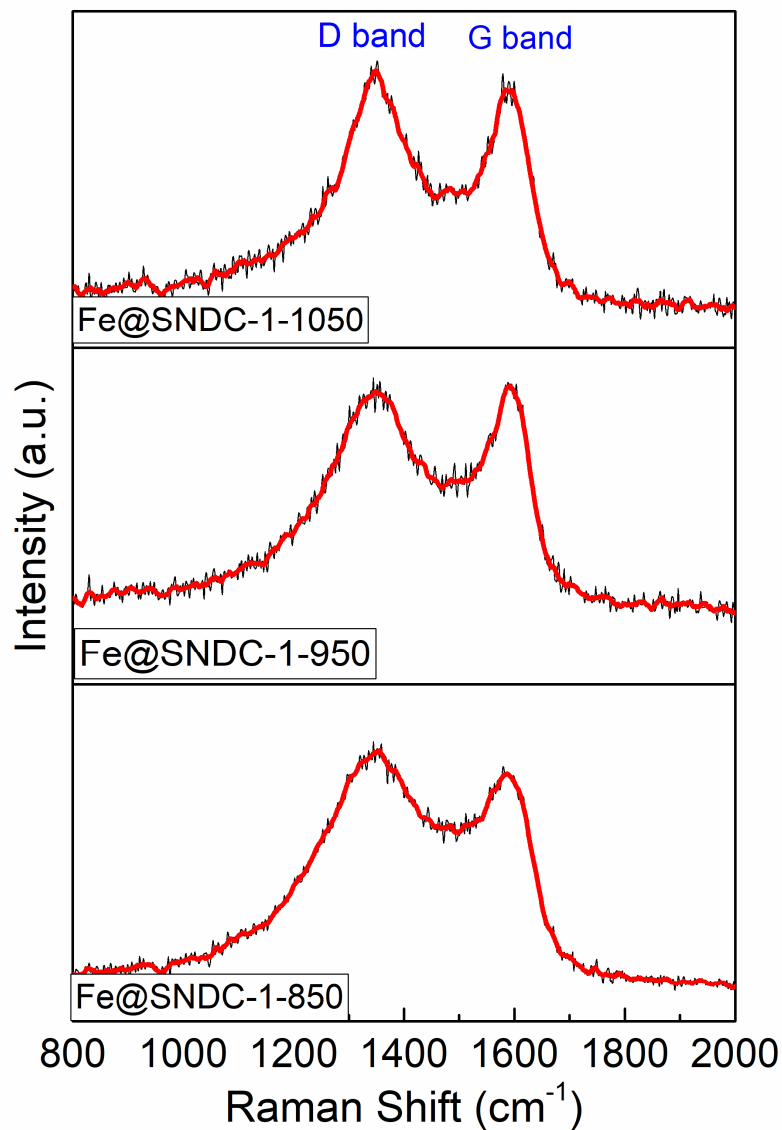
Figure 3.12: Raman spectra for Fe@SNDC samples.

All the samples displayed two intense peaks at around 1350 and 1590 cm^{-1} which are generally the D band and G band respectively. Bond stretching of all the sp^2-bonded pairs, including C–C, N–C, C–S, N–S are reflected by the G band while the D band reflects the sp^3 defect sites[30]. The $\frac{I_D}{I_G}$ ratios of Fe@SNDC samples range from 1.11, 0.97 and 1.08 with respect to their calcination temperature ranging from 850˚C to 1050˚C. This slight decrease in the $\frac{I_D}{I_G}$

ratio of Fe@SNDC-1-950 sample suggested more graphitic carbon structures compared to other samples[31]. Moreover, the broader the d band suggests more intercalation of heteroatoms into the conjugated carbon framework[32]. Fe@SNDC-1-950 sample with more graphitization had increased electronic conductivity and corrosion resistance during electrocatalysis. In addition, it had moderately broad d band with optimum dopants which served as active sites for ORR.

3.4.3 Electrochemical Characterization of Fe@SNDC samples in comparison to 20 wt% Pt/C

The electrochemical performance of Fe@SNDC–1–950 in ORR was assessed by cyclic voltammetry (CV) and compared to the performance of commercially available Pt/C (20 wt%) as shown in Figure 3.13 and 3.14.

The cyclic voltammograms obtained in nitrogen saturated 0.1 M KOH and 0.5 M H_2SO_4 showed a quasi-rectangular voltammogram without any redox peak due to the typical supercapacitance effect on porous carbon materials.[33, 34] When the electrolyte was saturated with O_2, Fe@SNDC–1–950 sample showed a well-defined characteristic ORR peak centered at 0.87 V vs RHE in 0.1 M KOH and an enhancement was observed in 0.5 M H_2SO_4 as shown in Figure 3. The cathodic current peak potential of Fe@SNDC–1–950 was slightly more positive than that of Pt/C (20 wt%). In acidic electrolyte, the CV showed a pair of reversible redox peaks (Fe^{3+}/Fe^{2+}) in between 0.62~0.64 V. These peaks are a common feature in CVs obtained using iron coordination compounds like $[Fe(CN)_6]^{3-}$/ $[Fe(CN)_6]^{4-}$.[35]
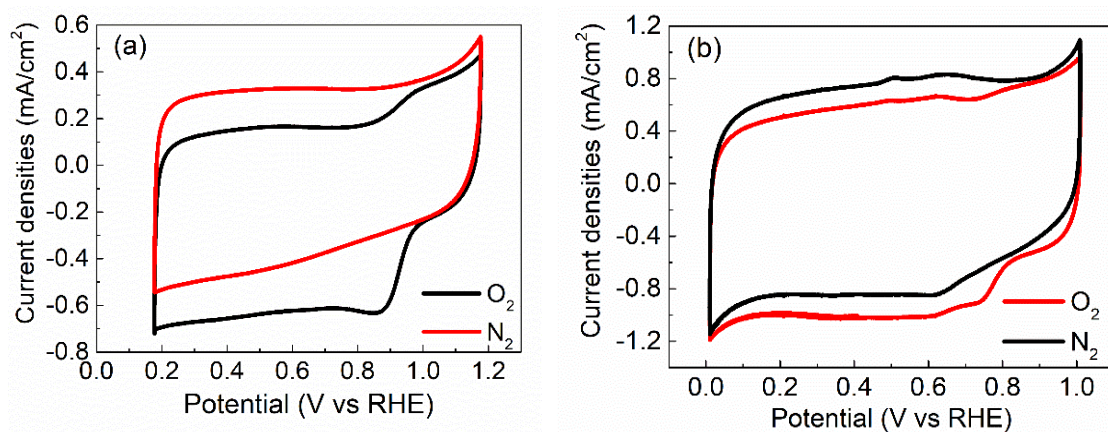
Figure 3.13: Cyclic voltammograms (CVs) for ORR obtained of Fe@SNDC–1–950 in N_2 and O_2 saturated (a) 0.1 M KOH and (b) 0.5 M H_2SO_4 at a scan rate of 20 mV/s.
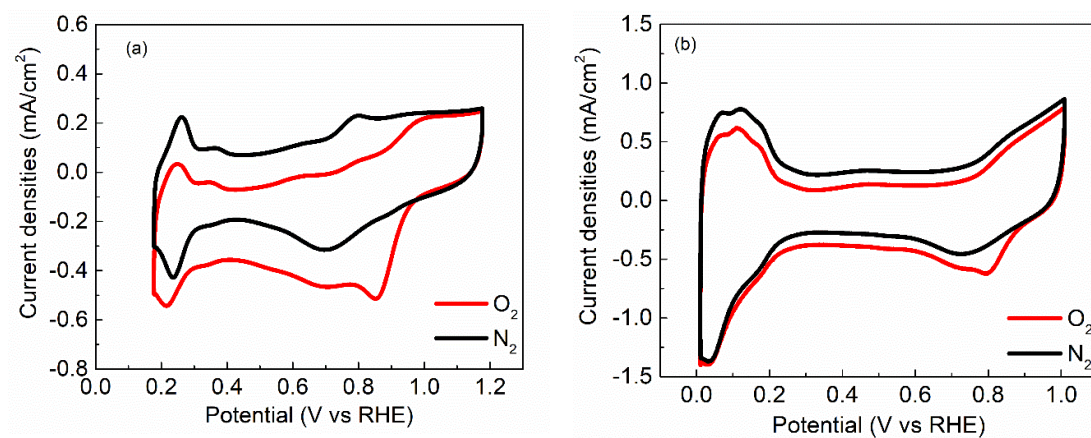

Figure 3.14: Cyclic voltammograms (CVs) for ORR obtained of 20 wt% Pt/C in N_2 and O_2 saturated (a) 0.1 M KOH and (b) 0.5 M H_2SO_4 at a scan rate of 20 mV/s.

To understand the kinetics and mechanism of ORR and linear sweep voltammograms (LSVs) were collected at different rpm starting from 400 to 2500 rpm in O_2 saturated acidic and alkaline electrolyte using rotating disk electrodes (RDE). The limiting current density increased linearly as the scan rate increased from 400 to 2500 rpm in all cases for short diffusion distance. Figure 3.15 and 3.16 show the LSVs of all the Fe@SNDC samples calcined at different temperatures. In 0.1 M KOH solution, Fe@SNDC–1–950 showed an onset potential of 0.98 V vs RHE which was quite close to the 0.99 V vs RHE obtained for commercially available 20 wt% Pt/C (Tables 3.3 and 3.4). The half wave potential and the limiting current density of Fe@SNDC–1–950 excelled the performance of samples calcined at 850 and 1050 °C suggesting that the optimum calcination temperature of the sample was 950 °C. Moreover, the Fe@SNDC–1–950 performed really well in 0.5 M H_2SO_4. The Koutecky Levich plot derived from the LSVs at a scan rate of 10 mV in O_2 saturated electrolyte displayed good linearity which suggested first order reaction kinetics toward the concentration of dissolved oxygen and similar electron transfer numbers for ORR at different potentials[36]. The number of electrons (n) in ORR was determined from the linear sweep voltammograms obtained by RDE as 3.5 (in alkaline solution) at the potential ranging from 0.2 ~ 0.6 V vs RHE. Another significant technique involving RRDE was also used to determine n as shown in Figure 4a and 4b and the n value was averaged to be 3.77 between 0.2 ~ 0.8 V vs RHE which was quite close to the four electron ORR pathway followed by 20 wt% Pt/C (Fig. S4). This result indicates that Fe@SNDC–1–950 is an excellent catalyst for ORR in alkaline solution. This RRDE was also used to monitor the percentage peroxide species (Figure 3.21 and 3.22) generated during the ORR which remained below 20% between 0.2 ~ 0.8 V vs RHE. In addition to alkaline media, Fe@SNDC–1–950 exhibited good ORR performance in 0.5 M H_2SO_4 with an n value of 3.4 and limiting current density quite close to the 20 wt% Pt/C.
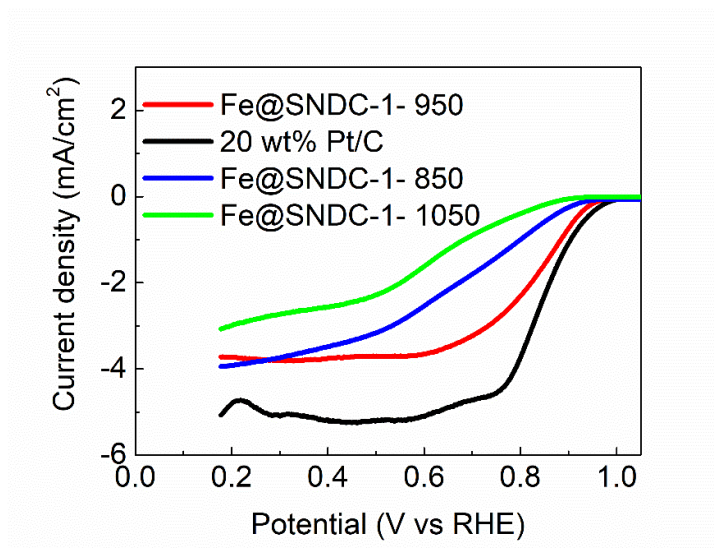
Figure 3.15: LSV curves at the rotating speed of 1600 rpm of the Fe@SNDC–1–850, Fe@SNDC–1–950, Fe@SNDC–1–1050 and Pt/C in O_2 saturated 0.1 M KOH.

Table 3.3: Onset and halfwave potentials of FeBIDC samples in 0.1 M KOH

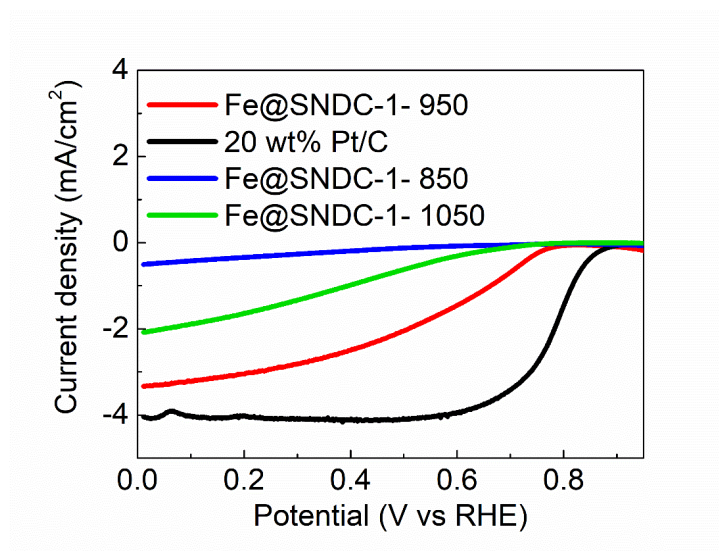| Samples	Onset Potential (V vs RHE)	Half wave potential (V vs RHE)	Limiting Current Density (mA/cm^2)
FeBIDC -1- 850	0.96	0.68	3.95
FeBIDC -1- 950	0.98	0.83	3.80
FeBIDC -1- 1050	0.91	0.61	3.06
20 wt% Pt/C	0.99	0.84	5.23

Figure 3.16: LSV curves at the rotating speed of 1600 rpm of the Fe@SNDC–1–850, Fe@SNDC–1–950, Fe@SNDC–1–1050 and Pt/C in O_2 saturated 0.5M H_2SO_4.

Table 3.4: Onset and halfwave potentials of FeBIDC samples in 0.5 M H_2SO_4

Samples	Onset Potential (V vs RHE)	Half wave potential (V vs RHE)	Limiting Current Density (mA/cm^2)
FeBIDC -1- 850	0.68	0.34	0.48
FeBIDC -1- 950	0.80	0.53	3.80
FeBIDC -1- 1050	0.74	0.39	2.06
20 wt% Pt/C	0.89	0.78	4.07

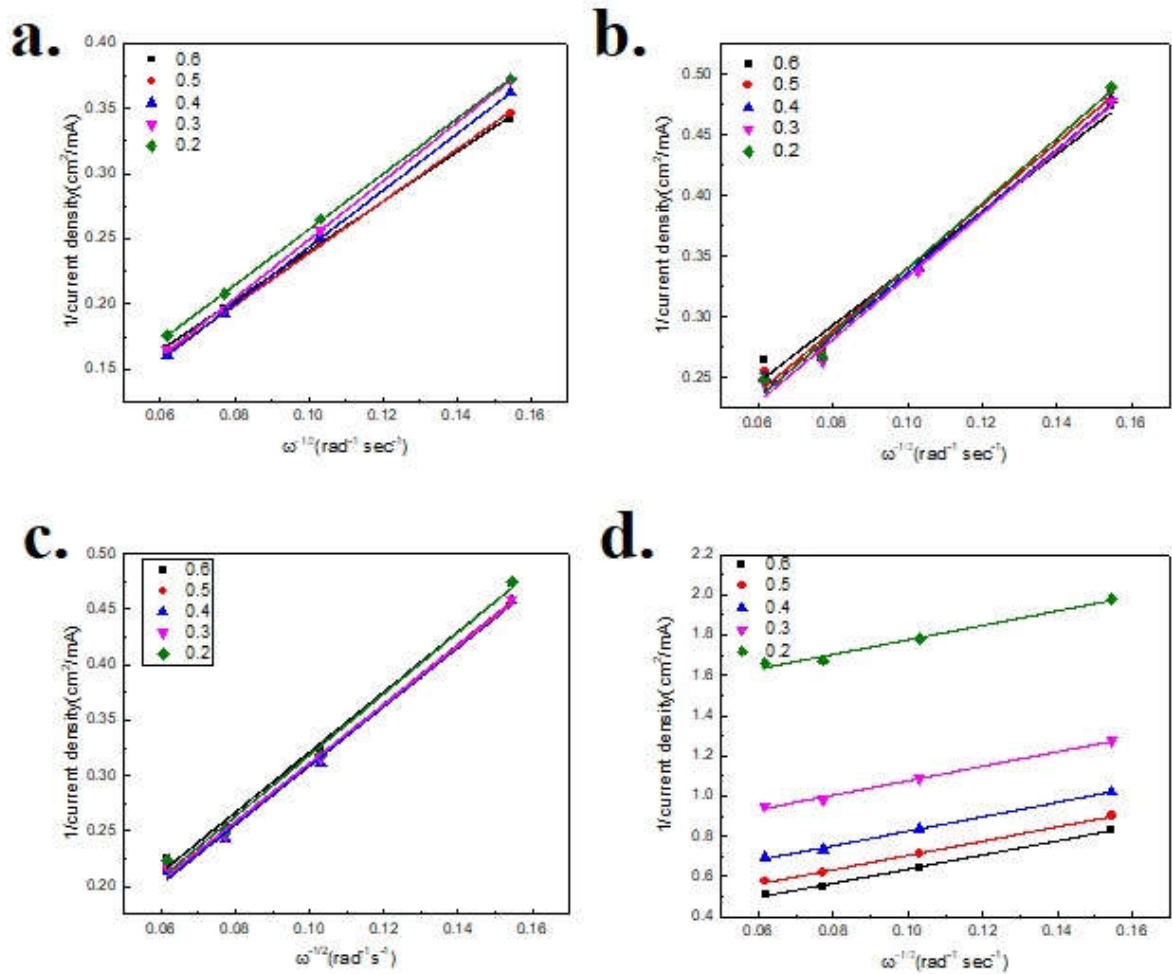**Figure 3.17**: Koutecky Levich plot of 20 wt% Pt/C (a) 0.1 M KOH and (c) 0.5 M H$_2$SO$_4$ and

in Fe@SNDC-950 (b) 0.1 M KOH and (d) 0.5 M H$_2$SO$_4$.

To calculate the number of electrons and determine the amount of HO_2^- produced while performing ORR, another technique involving RRDE was used beside RDE. The actual dimensions of the disk and ring in RRDE can vary as it is subjected to electrode polishing or temperature cycling. That's why it is important to measure the collection efficiency using a well-behaved redox system. Typically the ferrocyanide/ferricyanide half reaction, single-electron reversible half reaction, is used for measuring collection efficiency of RRDE. [37] The RRDE was placed in a solution of 10 mM potassium ferricyanide, $K_3Fe(CN)_6$ in 1 M potassium nitrate, KNO_3 solution. A positive potential of 1.6 V vs RHE is applied on both the ring and the disk so that no reaction occurs. While sweeping the potential of the disk towards negative at a scan rate of 50 mV/sec, the positive potential at the ring is held constant. A cathodic current is observed at the cathode (disk) corresponding to the reduction of ferricyanide to ferrocyanide.

$$Fe(CN)_6^{3-} + e^- \rightarrow Fe(CN)_6^{4-}$$
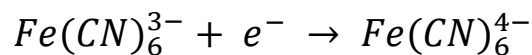
The generated ferrocyanide are pushed radially outward from the disk to the ring electrode. Since a positive potential is applied at the ring, some of the ferrocyanide are oxidized back to the ferricyanide. As a result, an anodic current is observed at the ring electrode.

$$Fe(CN)_6^{4-} \rightarrow Fe(CN)_6^{3-} + e^-$$
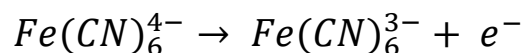
The ratio of the anodic and cathodic limiting current is the empirical collection efficiency, $N_{empirical}$. The linear sweep voltammograms for this RRDE is obtained by changing the rotation rate from 400 to 2500 rpm as shown in figure 3.18. As the rotation rate increases, both the cathodic and anodic current at the disk and ring increases. However, the collection efficiency is independent of the rotation rate due to the fact that limiting current is proportional to the square root of rotation rate.

This collection efficiency is a constant factor for this particular RRDE and can be used on any system regardless of the electrolyte solution.

$$N_{empirical} = -\frac{i_{limiting\ current\ at\ the\ ring}}{i_{limiting\ current\ at\ the\ disk}}$$
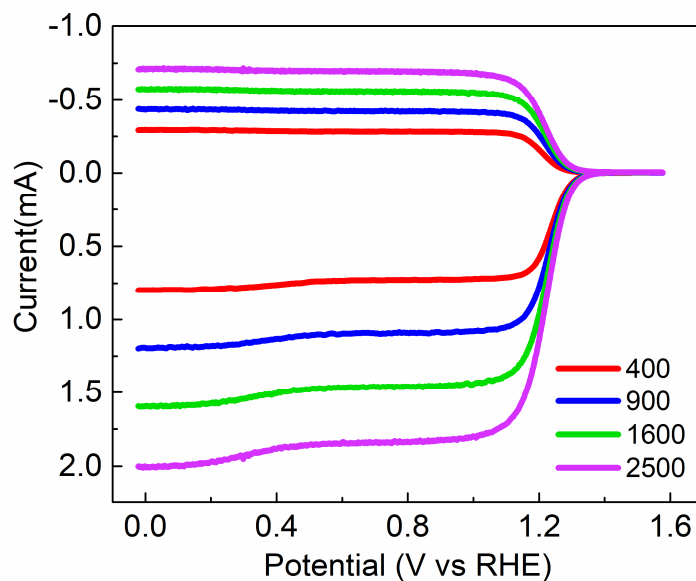

Figure 3.18: Calibration curve for collection efficiency in 10 mM potassium ferrocyanide in 1.0 M KNO$_3$.
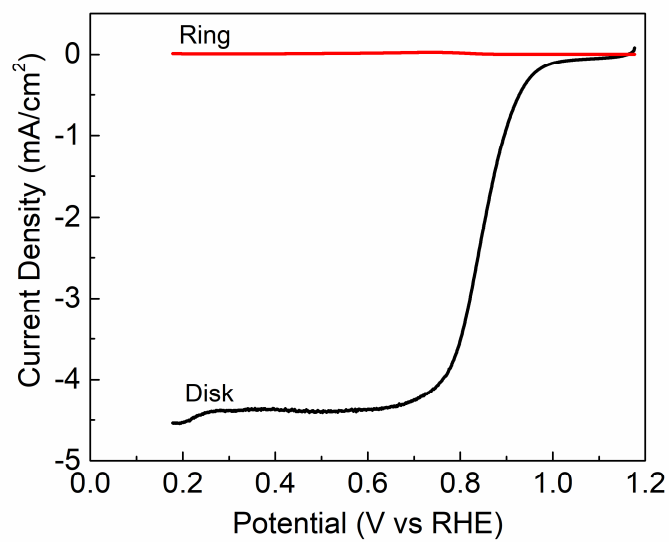
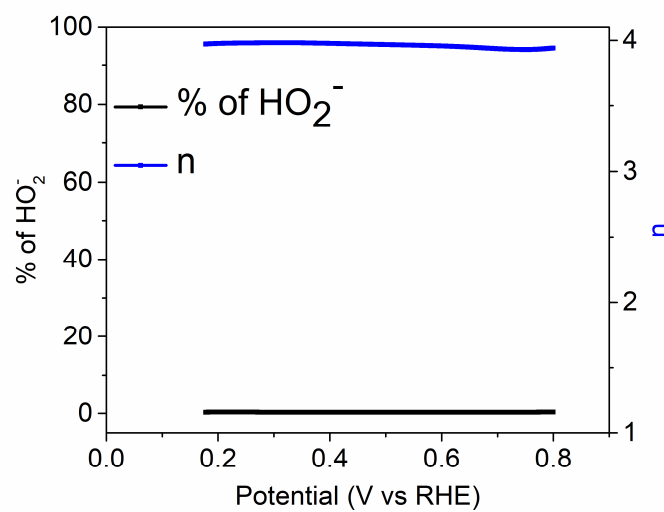**Figure 3.19:** Linear sweep voltammogram of 20 wt% Pt/C at 1600 rpm in 0.1M KOH.

Figure 3.20: The apparent number of electrons involved in ORR and the % of HO_2^- of 20 wt% Pt/C in 0.1M KOH derived from figure 3.19.
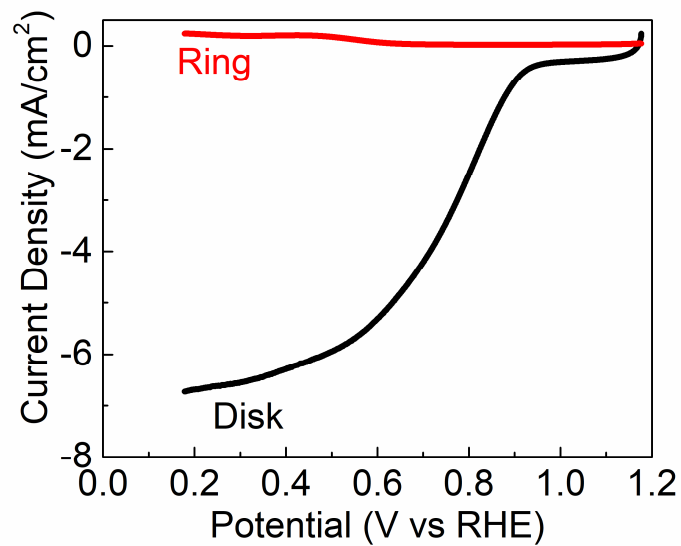
Figure 3.21: Linear sweep voltammogram of Fe@SNDC–1–950 using RRDE at 1600 rpm in 0.1 M KOH.
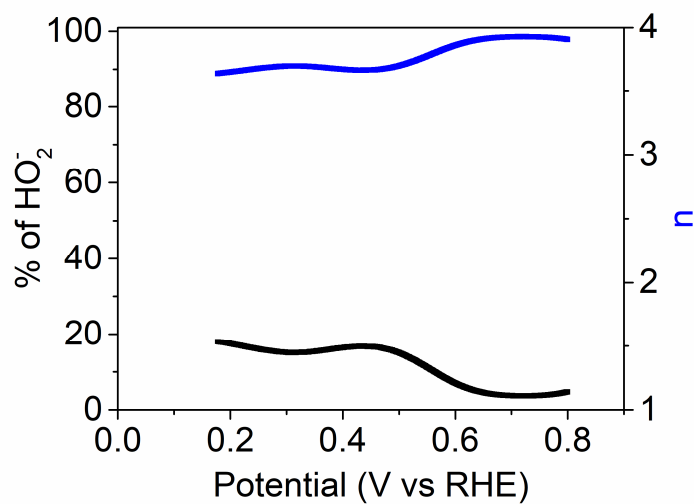

Figure 3.22: The apparent number of electrons involved in ORR and the % of HO_2^- of Fe@SNDC–1–950 in 0.1M KOH derived from figure 3.21.

Resistance to fuel crossover effects and long-term durability of the ORR catalysts are important criteria in fuel cell technology. The durability of Fe@SNDC–1–950 catalyst was measured using chronoamperometric i-t technique in 0.1 M KOH at 1600 rpm and was also compared to that of commercially available Pt/C (20 wt%) as shown in Figure 3.23. When the onset potential (0.877 V vs RHE) was applied for 12 hours, both the synthesized and commercial catalyst exhibited a slow degradation along with the time elapsed. However, Fe@SNDC–1–950 catalyst showed less degradability compared to Pt/C; it degraded only by 26 % after 12 hours. In case of direct methanol fuel cell, small amount of methanol sometimes can crossover from the anode to the cathode chamber and poison the ORR catalyst particularly Pt/C catalyst. The presence of methanol initiates methanol oxidation instead of oxygen reduction in Pt-based catalysts. To overcome this issue, the synthesized catalyst must be methanol tolerant and here the methanol tolerance of the Fe@SNDC–1–950 catalyst was measured by introducing 3 M methanol solution in O_2 saturated 0.1 M KOH solution. After the introduction of methanol, a drastic reduction in the ORR activity by Pt/C was observed whereas Fe@SNDC–1–950 was only slightly affected. The chronoamperometric i-t curves in Figure 3.26 indicate that Pt/C exhibited a massive 41% degradation in ORR activity over the 6 hours period while Fe@SNDC–1–950 showed only 8% degradation. Thus, Fe@SNDC–1–950 exhibited excellent stability and methanol tolerance in ORR which outperformed the performance of commercially available 20 wt% Pt/C.
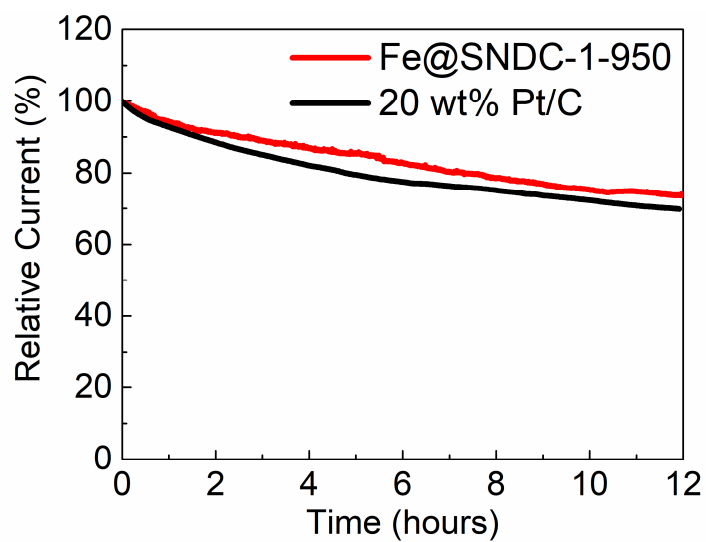
Figure 3.23: Chronoamperometric i-t curve of Fe@SNDC–1–950 and 20 wt% Pt/C in O_2 saturated 0.1M KOH.

Figure 3.24: Comparisons of cyclic voltammograms of 20 wt% Pt/C in either N_2 or O_2 saturated 0.1M KOH and also after addition of 3M methanol in O_2 saturated 0.1M KOH.
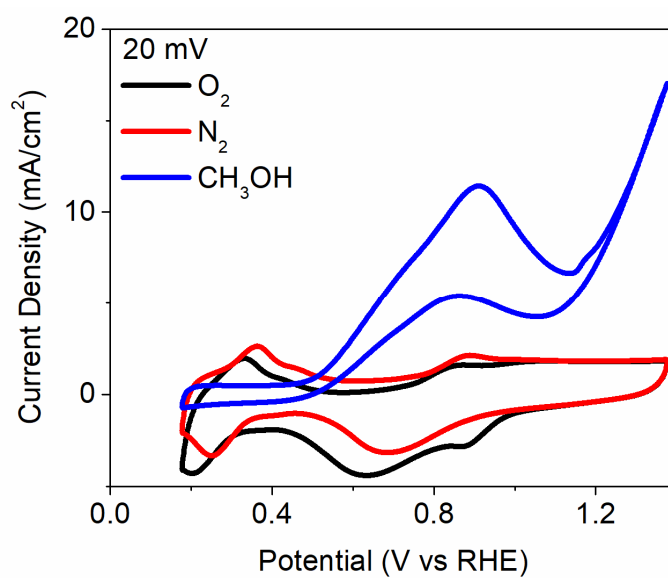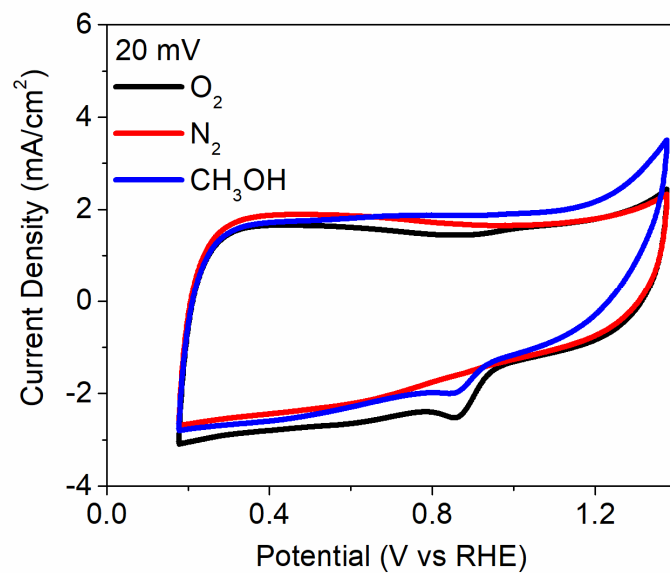
Figure 3.25: Comparisons of cyclic voltammograms of Fe@SNDC–950 in either N_2 or O_2 saturated 0.1M KOH and also after addition of 3M methanol in O_2 saturated 0.1M KOH.
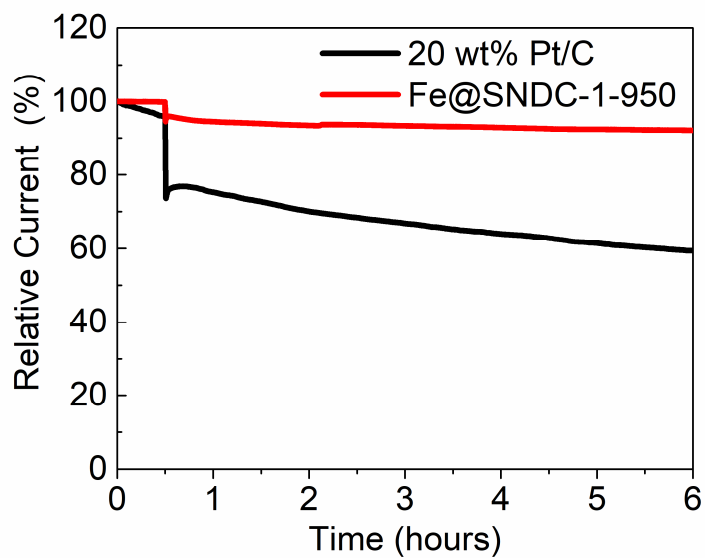

Figure 3.26: Methanol tolerance graph of Fe@SNDC–1–950 and 20 wt% Pt/C in O_2 saturated 0.1M KOH.

Table 3.5: Comparisons of onset, halfwave potentials and limiting current densities in the literature

Catalyst	Loading (mg/cm^2)	Electrolyte	E_{onset} (V vs RHE)	$E_{1/2}$ (V vs RHE)	Limiting current density (mA/cm^2)	Ref.
Fe-N-CA-800	0.2	0.1 M KOH	0.918	0.781	5.01	38
N-doped Fe/Fe$_3$C@C	0.7	0.1 M KOH	0.915	0.83	-	39
LDH@ZIF-67-800	0.2	0.1 M KOH	0.94	0.83	5.5	40
Fe−N/C-800	0.1	0.1 M KOH	0.923	0.809	6.06	41
		0.1 M HClO$_4$	0.687	~0.6	6.09	
Fe, S/NGC-900	0.2	0.1 M KOH	0.95	0.83	-	42
		0.1 M HClO$_4$	0.83	-	4.95	
VB12/silica colloid	0.6	0.5 M H$_2$SO$_4$	~0.8	0.79	4.5	14
PANI-Fe/Silica colloid	0.6	0.5 M H$_2$SO$_4$	0.84	0.73	-	
S-Fe/N/C	0.16	0.1 M HClO$_4$	0.83	0.66	-	43
		0.1M KOH	0.91	0.84		
Fe@SNDC -1-950	0.3	0.1 M KOH	0.98	0.83	3.80	This work

3.4.4 Application of secondary heat treatment to Fe@SNDC sample and its characterization and ORR performance

Another important phenomenon that was explored in this study was the application of secondary heat treatment (SHT) to pyrolyzed sample. It has been reported that secondary heat treatment of catalyst in N_2, NH_3, CO_2 or argon greatly improves the ORR performance of the catalyst. Particularly in presence of reactive gases such as NH_3, CO_2, SHT modifies the surface of the catalyst, improves the porosity and also allows incorporation of heteroatoms into the graphene structure, thereby enhancing electrocatalytic ORR performance of the synthesized catalyst. [44-48] But in our case, a nitrogen rich precursor along with iron thiocyanate was used to incorporate heteroatoms in the structure so inert gas was used instead of reactive gases. SHT in inert gases can also enhance the ORR performance by improving the porosity and enhancing the types of nitrogen in the catalyst.[17, 49]

The SEM image in Figure 3.27 revealed that SHT in Fe@SNDC sample resulted in more fragmentation of the structure along with small slightly spherical shaped clusters. When EDS elemental mapping was collected for Fe@SNDC–2–950 sample in Figure 3.28 , it appeared these clusters are probably iron sulfides which are reported as ORR inactive species.[11, 50]
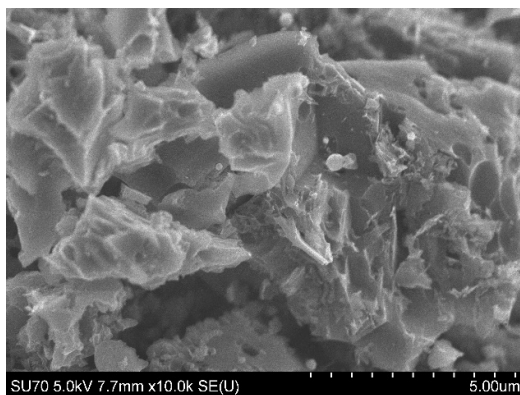

Figure 3.27: SEM image for Fe@SNDC–2–950 sample.
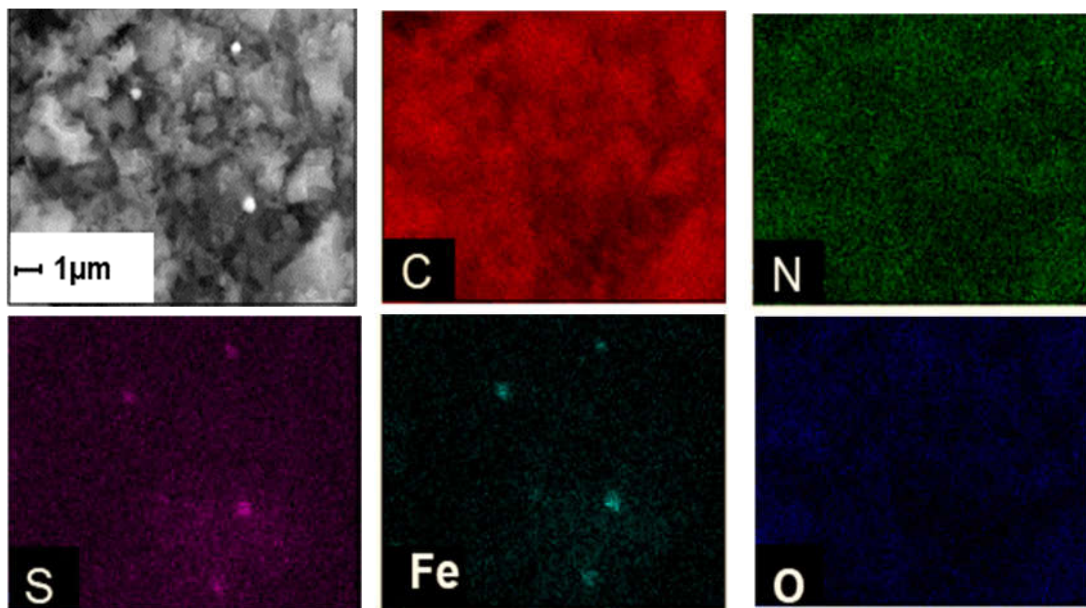
Figure 3.28: EDS elemental mapping for Fe@SNDC–2–950 sample.

.

The BET surface area of Fe@SNDC–2–950 as shown in Figure 3.30 depicted a mixture of Type I and Type IV isotherms which revealed it has both micro and mesoporosity. SHT in Fe@SNDC enhanced it surface area from 1101 to 1680 m^2g^{-1}. The QSDFT pore size distribution revealed the major pore size below 2 nm and minor pore sizes dispersed above 2 nm as shown in Figure 3.31. The XPS survey spectrum of Fe@SNDC–2–950 showed a slight decrease in the content of heteroatoms with moderate changes in the types of nitrogen and sulfur as depicted in the deconvoluted XPS spetra in Figure 3.32 and 3.33.
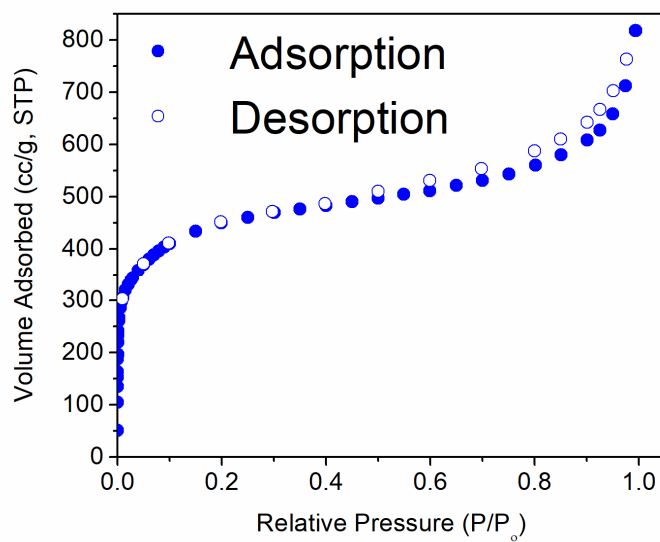
Figure 3.30: Nitrogen isotherms at 77 K of Fe@SNDC–2–950.
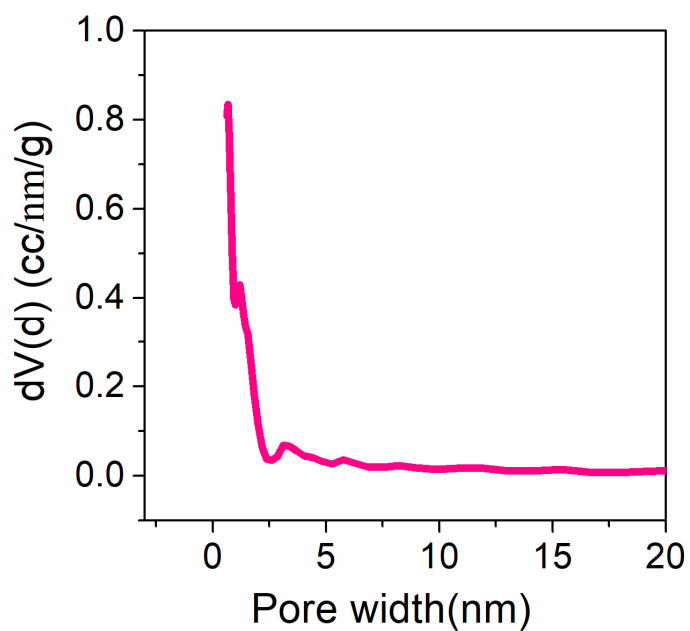
Figure 3.31: Pore size distribution (PSD) from QSDFT using N_2 at 77 K (Figure 3.30) of Fe@SNDC–2–950.
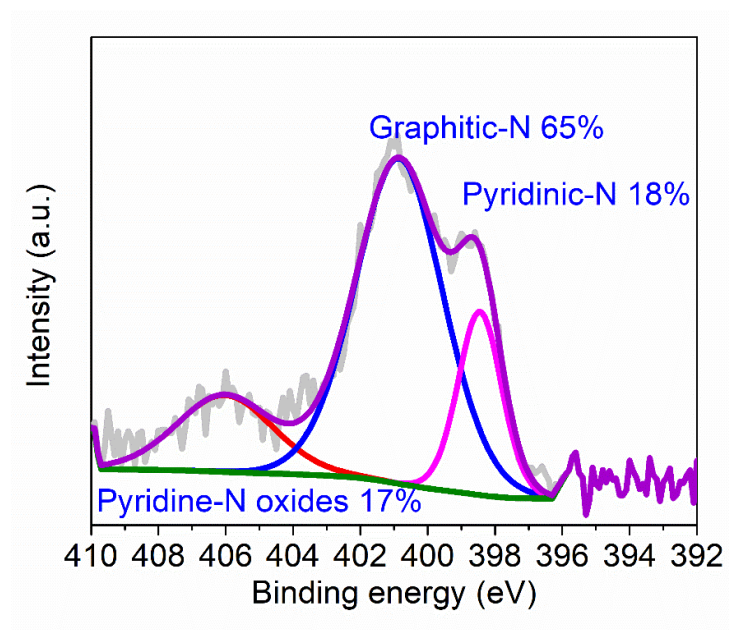
Figure 3.32: Deconvoluted N XPS spectrum of Fe@SNDC–2–950.
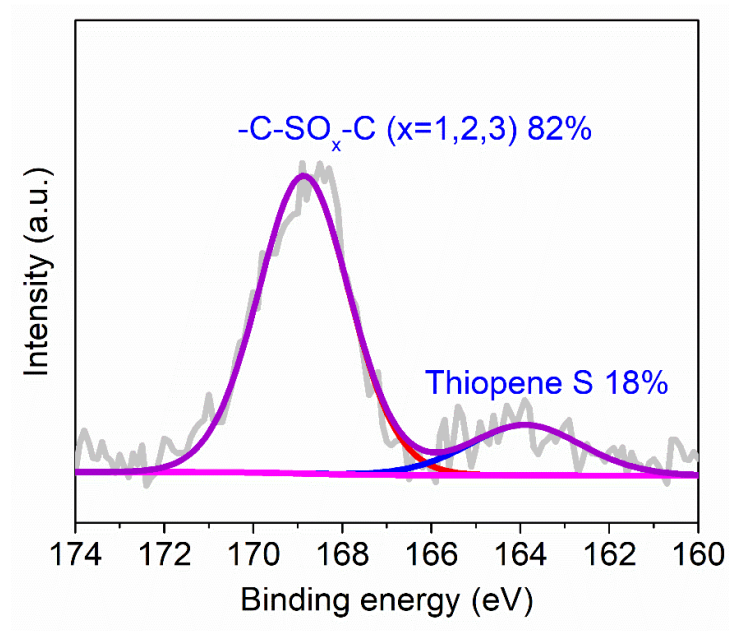
Figure 3.33: Deconvoluted S XPS spectrum of Fe@SNDC–2–950.

Figure 3.34: Linear sweep voltammogram of Fe@SNDC–2–950 in 0.1 M KOH solution.

Figure 3.35: Koutecky-Levich plot derived from the linear sweep voltammogram of Fe@SNDC–2–950 in 0.1 M KOH solution.

When the SHT was done on Fe@SNDC–2–950 samples, the surface area increased from 1101 to 1680 m^2g^{-1}. However, it was observed that Fe-N moieties decomposed forming ORR inactive iron sulfide. Due to the increase in surface area, the LSV showed higher limiting current density but the nu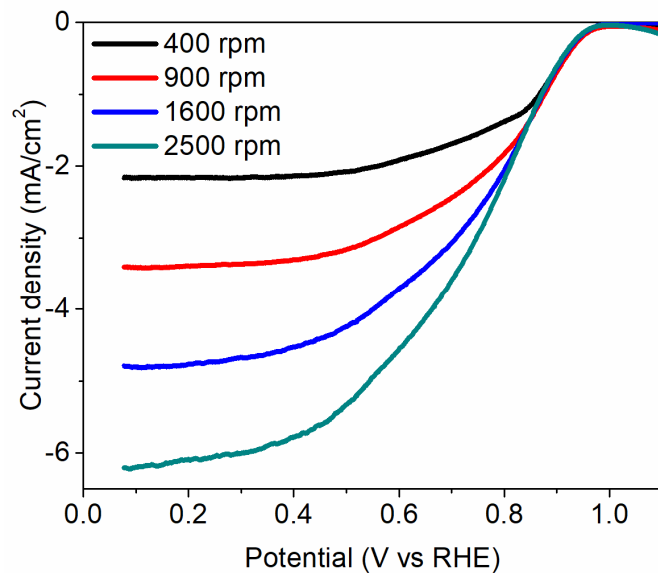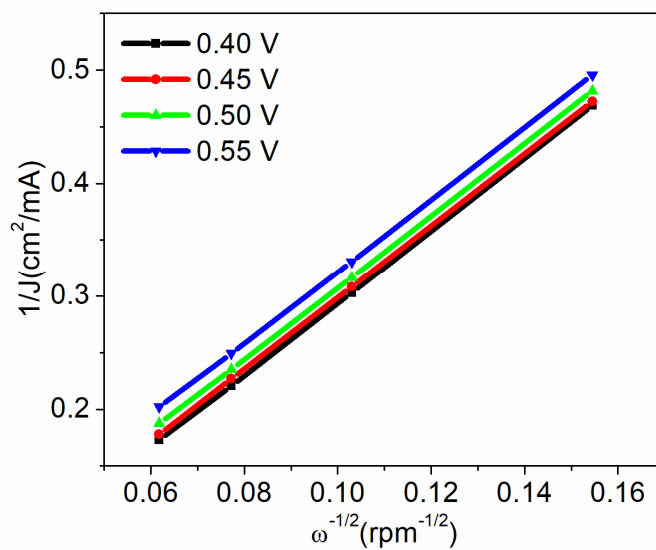mber of electrons in ORR was around 3 suggesting the catalyst preferred $2e^-$ pathway more than $4e^-$. The sample was also washed via Soxhlet extraction with 1M HCl at 80℃ which further reduced the ORR activity implying to the fact that higher surface area is important as long as there is enough active sites for ORR. So, in our case calcination in inert atmosphere for one time yielded a better ORR catalyst and SHT did not improve the electrocatlytic ORR perfromance.

3.5 Conclusions

In summary, we have developed a simple and corrosive template-free method for preparing Fe-based N and S doped porous carbon from an inexpensive commercially available monomer, benzimidazole and iron(III) thiocyanate. The surface area and pore size distribution of the catalyst are tuned by changing calcination temperature and 950 °C served as optimum calcination temperature producing high surface area and a wide pore size distribution ranging between 6 to 11 Å. The Fe@SNDC–1–950 catalyst comprising around 5 at% N mainly pyridinic and graphitic and a small amount of thiophene S exhibits an excellent ORR performance with an onset potential and half-wave potential of 0.98 and 0.83 V vs RHE, respectively. Both these values are only 0.01 V vs RHE less than commercial Pt/C (20 wt%). In addition, the number of electrons in ORR is averaged as 3.77 by RRDE technique with less than 20% HO_2^- generation. The presence of both S and N along with Fe-N in Fe@SNDC–1–950 enhances ORR performance in both acidic and alkaline media and provides superior stability and higher poison tolerance

3.6 References

1.   Ferrero, G. A.; Preuss, K.; Marinovic, A.; Jorge, A. B.; Mansor, N.; Brett, D. J. L.; Fuertes, A. B.; Sevilla, M.; Titirici, M. M., Fe-N-Doped Carbon Capsules with Outstanding Electrochemical Performance and Stability for the Oxygen Reduction Reaction in Both Acid and Alkaline Conditions. *Acs Nano* **2016,** *10* (6), 5922-5932.

2.   Li, Y. G.; Zhou, W.; Wang, H. L.; Xie, L. M.; Liang, Y. Y.; Wei, F.; Idrobo, J. C.; Pennycook, S. J.; Dai, H. J., An oxygen reduction electrocatalyst based on carbon nanotube-graphene complexes. *Nature Nanotechnology* **2012,** *7* (6), 394-400.

3.   Parvez, K.; Yang, S. B.; Hernandez, Y.; Winter, A.; Turchanin, A.; Feng, X. L.; Mullen, K., Nitrogen-Doped Graphene and Its Iron-Based Composite As Efficient Electrocatalysts for Oxygen Reduction Reaction. *Acs Nano* **2012,** *6* (11), 9541-9550.

4.   Wu, M. J.; Zhang, E. G.; Guo, Q. P.; Wang, Y. Z.; Qiao, J. L.; Li, K. X.; Pei, P. C., N/S-Me (Fe, Co, Ni) doped hierarchical porous carbons for fuel cell oxygen reduction reaction with high catalytic activity and long-term stability. *Applied Energy* **2016,** *175*, 468-478.

5.   Chang, Y. Q.; Hong, F.; He, C. X.; Zhang, Q. L.; Liu, J. H., Nitrogen and Sulfur Dual-Doped Non-Noble Catalyst Using Fluidic Acrylonitrile Telomer as Precursor for Efficient Oxygen Reduction. *Advanced Materials* **2013,** *25* (34), 4794-4799.

6.   Tian, W. J.; Zhang, H. Y.; Duan, X. G.; Sun, H. Q.; Tade, M. O.; Ang, H. M.; Wang, S. B., Nitrogen- and Sulfur-Codoped Hierarchically Porous Carbon for Adsorptive and Oxidative Removal of Pharmaceutical Contaminants. *Acs Applied Materials & Interfaces* **2016,** *8* (11), 7184-7193.

7.   Xiao, J.; Xia, Y. T.; Hu, C. C.; Xi, J. B.; Wang, S., Raisin bread-like iron sulfides/nitrogen and sulfur dual-doped mesoporous graphitic carbon spheres: a promising electrocatalyst for the oxygen reduction reaction in alkaline and acidic media. *Journal of Materials Chemistry A* **2017,** *5* (22), 11114-11123.

8.   Yu, H. J.; Shang, L.; Bian, T.; Shi, R.; Waterhouse, G. I. N.; Zhao, Y. F.; Zhou, C.; Wu, L. Z.; Tung, C. H.; Zhang, T. R., Nitrogen-Doped Porous Carbon Nanosheets Templated from g-C3N4 as Metal-Free Electrocatalysts for Efficient Oxygen Reduction Reaction. *Advanced Materials* **2016,** *28* (25), 5080-5086.

9.   Zhang, J. T.; Xia, Z. H.; Dai, L. M., Carbon-based electrocatalysts for advanced energy conversion and storage. *Science Advances* **2015,** *1* (7).

10.   Zhao, Z. H.; Li, M. T.; Zhang, L. P.; Dai, L. M.; Xia, Z. H., Design Principles for Heteroatom-Doped Carbon Nanomaterials as Highly Efficient Catalysts for Fuel Cells and Metal-Air Batteries. *Advanced Materials* **2015,** *27* (43), 6834-+.

11.   Masa, J.; Xia, W.; Muhler, M.; Schuhmann, W., On the Role of Metals in Nitrogen-Doped Carbon Electrocatalysts for Oxygen Reduction. *Angewandte Chemie-International Edition* **2015,** *54* (35), 10102-10120.

12.   Gewirth, A. A.; Varnell, J. A.; DiAscro, A. M., Nonprecious Metal Catalysts for Oxygen Reduction in Heterogeneous Aqueous Systems. *Chemical Reviews* **2018,** *118* (5), 2313-2339.

13.   Jaouen, F.; Proietti, E.; Lefevre, M.; Chenitz, R.; Dodelet, J. P.; Wu, G.; Chung, H. T.; Johnston, C. M.; Zelenay, P., Recent advances in non-precious metal catalysis for oxygen-reduction reaction in polymer electrolyte fuel cells. *Energy & Environmental Science* **2011,** *4* (1), 114-130.

14.   Liang, H. W.; Wei, W.; Wu, Z. S.; Feng, X. L.; Mullen, K., Mesoporous Metal-Nitrogen-Doped Carbon Electrocatalysts for Highly Efficient Oxygen Reduction Reaction. *Journal of the American Chemical Society* **2013,** *135* (43), 16002-16005.

15.   Oldacre, A. N.; Friedman, A. E.; Cook, T. R., A Self-Assembled Cofacial Cobalt Porphyrin Prism for Oxygen Reduction Catalysis. *Journal of the American Chemical Society* **2017,** *139* (4), 1424-1427.

16.   Tang, J.; Liu, J.; Li, C. L.; Li, Y. Q.; Tade, M. O.; Dai, S.; Yamauchi, Y., Synthesis of Nitrogen-Doped Mesoporous Carbon Spheres with Extra-Large Pores through Assembly of Diblock Copolymer Micelles. *Angewandte Chemie-International Edition* **2015,** *54* (2), 588-593.

17.   Wang, Y. C.; Lai, Y. J.; Song, L.; Zhou, Z. Y.; Liu, J. G.; Wang, Q.; Yang, X. D.; Chen, C.; Shi, W.; Zheng, Y. P.; Rauf, M.; Sun, S. G., S-Doping of an Fe/N/C ORR Catalyst for Polymer Electrolyte Membrane Fuel Cells with High Power Density. *Angewandte Chemie-International Edition* **2015,** *54* (34), 9907-9910.

18.   Men, B.; Sun, Y. Z.; Li, M. J.; Hu, C. Q.; Zhang, M.; Wang, L. N.; Tang, Y.; Chen, Y. M.;   Wan, P. Y.; Pan, J. Q., Hierarchical Metal-Free Nitrogen-Doped Porous Graphene/Carbon Composites as an Efficient Oxygen Reduction Reaction Catalyst. *Acs Applied Materials & Interfaces* **2016,** *8* (2), 1415-1423.

19.   Sheng, Z. H.; Shao, L.; Chen, J. J.; Bao, W. J.; Wang, F. B.; Xia, X. H., Catalyst-Free Synthesis of Nitrogen-Doped Graphene via Thermal Annealing Graphite Oxide with Melamine and Its Excellent Electrocatalysis. *Acs Nano* **2011,** *5* (6), 4350-4358.

20.   Wu, Z. Y.; Xu, X. X.; Hu, B. C.; Liang, H. W.; Lin, Y.; Chen, L. F.; Yu, S. H., Iron Carbide Nanoparticles Encapsulated in Mesoporous Fe-N-Doped Carbon Nanofibers for Efficient Electrocatalysis. *Angewandte Chemie-International Edition* **2015,** *54* (28), 8179-8183.

21.   Kone, I.; Xie, A.; Tang, Y.; Chen, Y.; Liu, J.; Chen, Y. M.; Sung, Y. Z.; Yang, X. J.; Want, P. Y., Hierarchical Porous Carbon Doped with Iron/Nitrogen/Sulfur for Efficient Oxygen Reduction Reaction. *Acs Applied Materials & Interfaces* **2017,** *9* (24), 20963-20973.

22.   Yuan, H. Y.; Hou, Y.; Wen, Z. H.; Guo, X. R.; Chen, J. H.; He, Z., Porous Carbon Nanosheets Codoped with Nitrogen and Sulfur for Oxygen Reduction Reaction in Microbial Fuel Cells. *Acs Applied Materials & Interfaces* **2015,** *7* (33), 18672-18678.

23. Zhang, J. W.; Xu, D.; Wang, C. C.; Guo, J. N.; Yan, F., Rational Design of Fe1-xS/Fe3O4/Nitrogen and Sulfur-Doped Porous Carbon with Enhanced Oxygen Reduction Reaction Catalytic Activity. *Advanced Materials Interfaces* **2018,** *5* (7).

24. Deng, D. H.; Pan, X. L.; Yu, L. A.; Cui, Y.; Jiang, Y. P.; Qi, J.; Li, W. X.; Fu, Q. A.; Ma, X. C.; Xue, Q. K.; Sun, G. Q.; Bao, X. H., Toward N-Doped Graphene via Solvothermal Synthesis. *Chemistry of Materials* **2011,** *23* (5), 1188-1193.

25. Guo, D. H.; Shibuya, R.; Akiba, C.; Saji, S.; Kondo, T.; Nakamura, J., Active sites of nitrogen-doped carbon materials for oxygen reduction reaction clarified using model catalysts. *Science* **2016,** *351* (6271), 361-365.

26. Daems, N.; Sheng, X.; Vankelecom, I. F. J.; Pescarmona, P. P., Metal-free doped carbon materials as electrocatalysts for the oxygen reduction reaction. *Journal of Materials Chemistry A* **2014,** *2* (12), 4085-4110.

27. Jeon, I. Y.; Zhang, S.; Zhang, L. P.; Choi, H. J.; Seo, J. M.; Xia, Z. H.; Dai, L. M.; Baek, J. B., Edge-Selectively Sulfurized Graphene Nanoplatelets as Efficient Metal-Free Electrocatalysts for Oxygen Reduction Reaction: The Electron Spin Effect. *Advanced Materials* **2013,** *25* (42), 6138-6145.

28. Zhu, J. B.; Li, K.; Xiao, M. L.; Liu, C. P.; Wu, Z. J.; Ge, J. J.; Xing, W., Significantly enhanced oxygen reduction reaction performance of N-doped carbon by heterogeneous sulfur incorporation: synergistic effect between the two dopants in metal-free catalysts. *Journal of Materials Chemistry A* **2016,** *4* (19), 7422-7429.

29. Yang, Z.; Yao, Z.; Li, G. F.; Fang, G. Y.; Nie, H. G.; Liu, Z.; Zhou, X. M.; Chen, X.; Huang, S. M., Sulfur-Doped Graphene as an Efficient Metal-free Cathode Catalyst for Oxygen Reduction. *Acs Nano* **2012,** *6* (1), 205-211.

30.   Wang, S. Y.; Zhang, L. P.; Xia, Z. H.; Roy, A.; Chang, D. W.; Baek, J. B.; Dai, L. M., BCN Graphene as Efficient Metal-Free Electrocatalyst for the Oxygen Reduction Reaction. *Angewandte Chemie-International Edition* **2012,** *51* (17), 4209-4212.

31.   Zhong, H. H.; Luo, Y.; He, S.; Tang, P. G.; Li, D. Q.; Alonso-Vante, N.; Feng, Y. J., Electrocatalytic Cobalt Nanoparticles Interacting with Nitrogen-Doped Carbon Nanotube in Situ Generated from a Metal-Organic Framework for the Oxygen Reduction Reaction. *Acs Applied Materials & Interfaces* **2017,** *9* (3), 2541-2549.

32.   Li, Y.; Zhao, Y.; Cheng, H. H.; Hu, Y.; Shi, G. Q.; Dai, L. M.; Qu, L. T., Nitrogen-Doped Graphene Quantum Dots with Oxygen-Rich Functional Groups. *Journal of the American Chemical Society* **2012,** *134* (1), 15-18.

33.   Yang, W.; Fellinger, T. P.; Antonietti, M., Efficient Metal-Free Oxygen Reduction in Alkaline Medium on High-Surface-Area Mesoporous Nitrogen-Doped Carbons Made from Ionic Liquids and Nucleobases. *Journal of the American Chemical Society* **2011,** *133* (2), 206-209.

34.   Liang, J.; Jiao, Y.; Jaroniec, M.; Qiao, S. Z., Sulfur and Nitrogen Dual-Doped Mesoporous Graphene Electrocatalyst for Oxygen Reduction with Synergistically Enhanced Performance. *Angewandte Chemie-International Edition* **2012,** *51* (46), 11496-11500.

35.   Zhu, Y. S.; Zhang, B. S.; Liu, X.; Wang, D. W.; Su, D. S., Unravelling the Structure of Electrocatalytically Active Fe-N Complexes in Carbon for the Oxygen Reduction Reaction. *Angewandte Chemie-International Edition* **2014,** *53* (40), 10673-10677.

36.   Liang, Y. Y.; Li, Y. G.; Wang, H. L.; Zhou, J. G.; Wang, J.; Regier, T.; Dai, H. J., Co3O4 nanocrystals on graphene as a synergistic catalyst for oxygen reduction reaction. *Nature Materials* **2011,** *10* (10), 780-786.

37.   Paulus, U. A.; Schmidt, T. J.; Gasteiger, H. A.; Behm, R. J., Oxygen reduction on a high-surface area Pt/Vulcan carbon catalyst: a thin-film rotating ring-disk electrode study. *Journal of Electroanalytical Chemistry* **2001,** *495* (2), 134-145.

38.   Wang, Q. C.; Chen, Z. Y.; Wu, N.; Wang, B.; He, W.; Lei, Y. P.; Wang, Y. D., N-Doped 3D Carbon Aerogel with Trace Fe as an Efficient Catalyst for the Oxygen Reduction Reaction. *Chemelectrochem* **2017,** *4* (3), 514-520.

39.   Hou, Y.; Huang, T. Z.; Wen, Z. H.; Mao, S.; Cui, S. M.; Chen, J. H., Metal-Organic Framework-Derived Nitrogen-Doped Core-Shell-Structured Porous Fe/Fe3C@C Nanoboxes Supported on Graphene Sheets for Efficient Oxygen Reduction Reactions. *Advanced Energy Materials* **2014,** *4* (11).

40.   Li, Z. H.; Shao, M. F.; Zhou, L.; Zhang, R. K.; Zhang, C.; Wei, M.; Evans, D. G.; Duan, X., Directed Growth of Metal-Organic Frameworks and Their Derived Carbon-Based Network for Efficient Electrocatalytic Oxygen Reduction. *Advanced Materials* **2016,** *28* (12), 2337-2344.

41.   Lin, L.; Zhu, Q.; Xu, A. W., Noble-Metal-Free Fe-N/C Catalyst for Highly Efficient Oxygen Reduction Reaction under Both Alkaline and Acidic Conditions. *Journal of the American Chemical Society* **2014,** *136* (31), 11027-11033.

42.   Men, B.; Sun, Y. Z.; Liu, J.; Tang, Y.; Chen, Y. M.; Wan, P. Y.; Pan, J. Q., Synergistically Enhanced Electrocatalytic Activity of Sandwich-like N-Doped Graphene/Carbon Nanosheets Decorated by Fe and S for Oxygen Reduction Reaction. *Acs Applied Materials & Interfaces* **2016,** *8* (30), 19533-19541.

43.   Hu, K.; Tao, L.; Liu, D. D.; Huo, J.; Wang, S. Y., Sulfur-Doped Fe/N/C Nanosheets as Highly Efficient Electrocatalysts for Oxygen Reduction Reaction. *Acs Applied Materials & Interfaces* **2016,** *8* (30), 19379-19385.

Chapter 4

Co$_3$O$_4$ deposited N doped Benzimidazole derived Porous Carbon for Electrocatalysis of Oxygen Reduction Reaction

4.1 Abstract

Development of an effective ORR catalyst is considered as the most important factor in wide commercialization of many renewable energy technologies including fuel cells and metal air batteries. Despite the report of several effective ORR catalysts, a cost-effective synthesis of ORR catalyst remains a great challenge. In this work, Co$_3$O$_4$ loaded on N doped benzimidazole derived porous carbon was prepared to evaluate its catalytic activity in oxygen reduction reaction. Initially, benzimidazole derived porous carbon was synthesized via chemical activation of benzimidazole at a high calcination temperature. Then Co$_3$O$_4$ crystals were grown on the surface of N doped carbon to develop the Co-BIDC samples. The pore size, nitrogen content and different types of nitrogen functionalities such as pyridinic, pyrrolic and graphitic in BIDC samples along with Co$_3$O$_4$ together enhanced the catalytic activity of Co-BIDC. Increasing the amount of Co$_3$O$_4$ further improved the performance of the catalyst. Even though the onset potential and limiting current density of Co-BIDC was slightly lower in comparison to the commercially available Pt/C (20 wt.%). However, the selectivity of ORR mechanism in case of Co-BIDC is four electron pathway which is energy efficient with minimum or nearly zero formation of hydrogen peroxide. In addition, the catalyst displayed excellent poison tolerance in case of methanol crossover, as well as high durability and stability in oxygen saturated alkaline electrolyte.

4.2 Introduction

Oxygen reduction reaction catalyst can significantly affect the wide practical application of many renewable energy technologies such as fuel cells and metal-air batteries. The most common catalysts that have been used in such technologies are either Pt or Pt dispersed on activated carbon. However, the cost and scarcity of Pt together with its poison intolerance and long-term durability issue hinder the development of such environment friendly devices. To date, many studies have been conducted to develop nonprecious transition metal oxides supported on either graphene or N doped carbon-based materials as effective ORR catalysts,[1-4] nitrogen coordinated metal on carbon,[5, 6] and also metal free heteroatom doped carbon.[7] The metal or the oxide catalysts without graphene support displayed lower durability as these catalysts suffer from dissolution, sintering, and agglomeration while operating in fuel cell condition.[8] In order to overcome this issue, graphene has been used extensively by several researchers because it increases the electroactive surface area of the catalyst and also prevents catalysts degradation by attaching the metal or metal oxide to its surface.[4, 8-11]

Here we report a simple and cost-effective synthetic procedure for growing Co_3O_4 on the surface of N doped porous carbon via hydrothermal treatment. Recently, we reported a facile synthetic procedure to obtain N doped porous carbon via KOH activation of benzimidazole at elevated temperature.[12] This synthetic route is environment friendly as it eliminates the use of templates or harsh solvents. We have varied the amount of Co_3O_4 and evaluated its impact as ORR catalysts. The CoBIDC catalyst demonstrated an outstanding ORR performance in alkaline medium due to the synergistic effect of Co_3O_4 and N doped carbon. The superior long-term durability and excellent methanol tolerance of the synthesized catalysts in comparison to commercial Pt/C (20 wt%) suggested that CoBIDC have the potential to serve as cost-effective ORR catalysts.

4.3 Experimental Section

4.3.1 Materials and Methods

All chemicals were purchased from commercial suppliers (Alfa Aesar, Acros Organics, TCI America) and used without further modification. The nitrogen doped porous carbon was synthesized by a procedure reported by El-Kaderi *et al*.[12] Initially, the benzimidazole (BI) and potassium hydroxide (KOH) (BI:KOH ratio of 1:3) were grinded into homogeneous mixture with mortar and pestle inside a glovebox. Then the solid mixture was poured into a porcelain boat and transferred to a temperature-programmed tube furnace. Prior to calcination, the sealed tube furnace was purged by passing inert argon gas at room temperature to remove traces of air. Calcination was done at 700°C at a ramp rate of 5°C for 1 hour under continuous flow of argon. The calcined sample was then soaked in 20 mL of 1 M HCl and the volume of the acid solution was replenished three times, followed by washing with plenty of distilled water and ethanol. This washing procedure is done to remove metallic potassium, residual salts etc. According to the above citation, the benzimidazole derived carbons were named as "BIDC-x-y", where the "x" indicates the KOH to BI mass ratio and "y" represents the calcination temperature. The resulting BIDC-3-700 was degassed under vacuum at 100°C for 6 hours.

About 50 mg of the BIDC-3-700 was then stirred continuously in around 151 ml of ethanol to form a highly dispersed solution. After 30 min, in order to grow Co_3O_4 on the surface of BIDC-3-700, 8 ml of 0.2 M cobalt acetate tetrahydrate solution was added followed by 3 ml of NH_4OH solution. The whole mixture was stirred continuously for 10 hours at 80°C. Then the reaction mixture was transferred in a 200 mL autoclave for hydrothermal reaction at 150°C for 3 h. After this hydrothermal treatment, the solvent was removed via rotary evaporation followed by washing with water and ethanol. This experiment was repeated by doubling the amount of cobalt acetate tetrahydrate keeping the rest of the parameters same.

4.3.2 Physical Characterization

Before collecting the adsorption/desorption isotherms of CoBIDC samples, the samples were degassed at 100 °C for 6 h. After that, N_2 isotherms at 77 K were collected using Autosorb-iQ2 volumetric adsorption analyzer (Quantachrome Instruments) and Brunauer−Emmett−Teller (BET) method was used to calculate the specific surface area of the samples. From the equilibrium branch of N_2 (77 K) adsorption isotherms, the pore size distributions (PSD) of the samples were determined. Quench solid density functional theory (QSDFT) model assuming that the carbon material has slit-pore geometry was applied for PSD calculations.

To obtain the scanning electron microscopy (SEM) images of the synthesized samples, Hitachi SU-70 scanning electron microscope was used. The samples were prepared by dispersing each specimen onto the surface of a flat aluminum sample holder with silver paste. Prior to SEM imaging, the conductive samples were coated with platinum at a pressure of 1.0 x 10^{-5} bar in a N_2 atmosphere for 60s. Energy-dispersive X-ray spectroscopy (EDX) was used to collect elemental mapping for visual demonstration of elemental distribution.

Thermo Fisher Scientific ESCALAB 250 spectrometer employing an Al Kα (1486.68 eV) X-ray source equipped with a hemispherical analyzer was used for X-ray photoelectron spectroscopy (XPS) analysis. For XPS measurements, the samples were pressed on a small piece of indium foil and mounted onto the sample holder using double-sided sticky carbon tape. In order to compensate for the charge while performing XPS analysis, a combination of a low-energy electron flood gun and an argon ion flood gun was utilized. The C 1s peak was set at 285.0 eV and thus the binding energy scale was calibrated. Thermo Avantage software (v4.84) was used to analyze the XPS spectra.

A Panalytical X'Pert Pro Multipurpose Diffractometer (MPD) was used to collect the Powder X-ray diffraction (P-XRD) patterns of the dried samples at room temperature. The

samples were mounted on a zero-background sample holder measured in transmission mode using Cu Kα radiation with a 2θ range of 20 to 70.

4.3.3 Electrochemical Characterization

The electrochemical measurements were conducted using a conventional three electrode setup with Ag/AgCl in 3 M KCl (reference electrode), glassy carbon electrode (working electrode) and Pt wire (counter electrode) in a Bipotentiostat (Model 760E Series, CH Instruments). The catalyst ink was prepared by ultrasonically dispersing 3.0 mg of the catalyst in a solution containing 25 μL of Nafion per fluorinated resin (5 wt %, Sigma-Aldrich) and 400 μL of isopropanol. About 10 μL of the catalyst ink was pipetted onto a polished glassy carbon electrode and dried in an oven for half an hour. The loading of the catalyst was 0.36 mg/cm^2. The electrochemical performance of the catalyst was compared to commercial Pt/C (20 wt % Pt on graphitized carbon, Sigma-Aldrich) with similar catalyst loading. The electrolytes for alkaline medium was 0.1 M KOH. At the beginning of the electrochemical testing procedures, the electrolytes were saturated with either nitrogen or ultra-high purity oxygen by bubbling the gas in the electrolyte for an hour and a continuous supply of either nitrogen or oxygen gases were maintained throughout the experiment in order to create a blanket over the solution.

According to Nernst equation, the measured potential vs Ag/AgCl (3M KCl) can be converted to the reversible Hydrogen electrode (RHE) scale following:

$$E_{RHE} = E_{Ag/AgCl} + 0.059\, pH + E^{\circ}_{Ag/AgCl} \quad (1)$$

where $E_{Ag/AgCl}$ is the experimentally measured potential vs Ag/AgCl, $E^{\circ}_{Ag/AgCl}$ is 0.210 V at 25 °C.

The ORR performance was evaluated by cyclic voltammetry (CV) in N_2 or O_2 saturated 0.1 M KOH and 0.5 M H_2SO_4 in a potential window 0 to 1.0 V vs RHE at varying sweep rates from 5 to 50 mV. The ORR kinetics were evaluated by linear sweep voltammetry (LSV) at various rotations rates per minute ranging from 400 to 2500 rpm. The Koutecky-Levich equation was used to determine the number of electrons in oxygen reduction reactions.

$$1/J = 1/J_L + 1/J_K$$

$$= 1/B\omega^{1/2} + 1/J_K$$

$$B = 0.2nFC_o(D_o)^{2/3} v^{-1/6}$$

where J = Measured current density, J_K = Kinetic current density, J_L = Diffusion limiting current density, ω = Rotation per minute, n = Transferred number of electrons, F= Faraday's constant, C_o = Bulk concentration of O_2, D_o = Diffusion coefficient of O_2, v = Kinematic viscosity.

Rotating ring disk voltammetry (RRDE) was used to determine the apparent number of electrons (n_e-) involved in ORR using the following equation:

$$n_{e^-} = \frac{4I_D}{I_D + {I_R}/{N}}$$

where I_D is the disk current, I_R is the ring current and N is the collection efficiency.

The collection efficiency of RRDE was measured using 10 mM potassium ferrocyanide in 1.0 M KNO_3 and calculated to be 0.36. The durability test of the catalyst was done using the chronoamperometric i-t technique at 0.88 V vs RHE in O_2 saturated 0.1 M KOH solution with a rotation of 1600 rpm for 12 hours. The methanol tolerance test was also evaluated by both cyclic voltammetry and chronoamperometric i-t technique with the introduction of 3 M methanol solution.

4.4. Results and Discussion

4.4.1 Synthetic route for loading Co_3O_4 on N doped porous carbon

Initially chemical activation using KOH was used to synthesize N doped porous carbon. This KOH activation of chars, coals, cokes, or various structured carbons has been done extensively in the literature to generate porous network in the carbon material. Firstly, the carbon material reacts with KOH via solid–solid reactions but later it proceeds via solid–liquid reactions.[13,14] Our group has recently reported KOH activation of N and C single source precursors like benzimidazole, pyrazole which are enriched with nitrogen to produce N-doped porous carbons.[12, 15] These precursors have low sublimation temperature and sublime during thermal treatment at elevated temperature. However, when KOH and BI are calcined together, KOH reacts with the acidic NH in BI forming potassium–benzimidazole salts. This salt has higher thermal stability and can withstand higher temperatures without decomposing. When the heating is continued, the excess KOH at higher temperature reacts with carbon and form either potassium oxide, potassium carbonate or metallic potassium. These intermediates can cause etching (by redox reactions), gasification (by evolving gaseous species such as H_2O and CO_2 and expansion (by metallic potassium) of the carbon framework.[13] As a result, KOH activation can lead to the formation of porous material. Once the N-doped carbon was prepared, it was then used as a base to grow Co_3O_4. The cobalt oxide crystals were grown by two step method reported by Liang *et al.*[3] In the first step, the mixture of BIDC-2-700 and cobalt (II) acetate tetrahydrate was stirred continuously maintaining a temperature of 80°C in order to hydrolyze and oxidize cobalt acetate. An appropriate ratio of ethanol/water and reaction temperature of 80°C was maintained to control the rate of hydrolysis for the nucleation of Co_3O_4. The second step involved hydrothermal treatment at 150°C which allowed crystallization of Co_3O_4 to form the CoBIDC samples. The ammonium hydroxide solution was

added to facilitate hydrolysis of Co^{2+} and oxidation of cobalt acetate tetrahydrate.[16] Figure 4.1 illustrates the synthesis of CoBIDC samples.
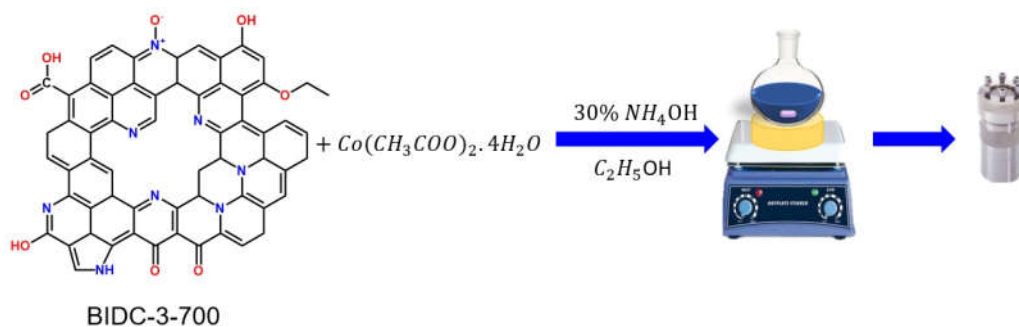

Figure 4.1: Synthesis of Co_3O_4 on the surface of benzimidazole derived porous carbon.

4.4.2 Physical Characterization of CoBIDC samples

In order to study the effect of Co_3O_4 on the porosity parameters of BIDC-3-700, N_2 adsorption and desorption isotherms of CoBIDC samples were analyzed (Figure 4.2). The important porosity parameters are summarized in Table 4.1. It was observed that the growth of Co_3O_4 on the BIDC–3–700 sample led to a remarkable decrease in its surface area and pore volume. In case of CoBIDC–1, the isotherm showed a rapid uptake up to a relative pressure of 0.003 and then the gas uptake continued to increase slowly. This suggested that it had both micro-/meso-pores, but the dominant pores were small micropores with a pore width of 6Å. When the amount of Co precursors was doubled, the isotherm of CoBIDC–2 displayed relatively smaller increase in gas uptake at low relative pressure followed by a significantly increased gas uptake at higher relative pressure. It showed a more enhanced hysteresis suggesting the presence of mesopores. The PSD of CoBIDC–2 revealed that it had a broad pore size distribution with pore sizes ranging from 6~48Å. Higher surface area facilitates the

effective transport of reactive species to the active site of catalyst. In this study, it was observed that high surface area of BIDC–3–700 sample alone was not able to catalyze the reduction of oxygen effectively. However, when Co_3O_4 was incorporated in the structure the selectivity and performance of the catalyst improved significantly. CoBIDC–2 displayed better ORR catalytic activity in comparison CoBIDC–1 owing to the presence of wider pores which served as low resistant diffusion channels allowing rapid flow of oxygen and electrolytes without accumulating the reactant, product or any intermediate species and thus ensure efficient mass transfer.[17]
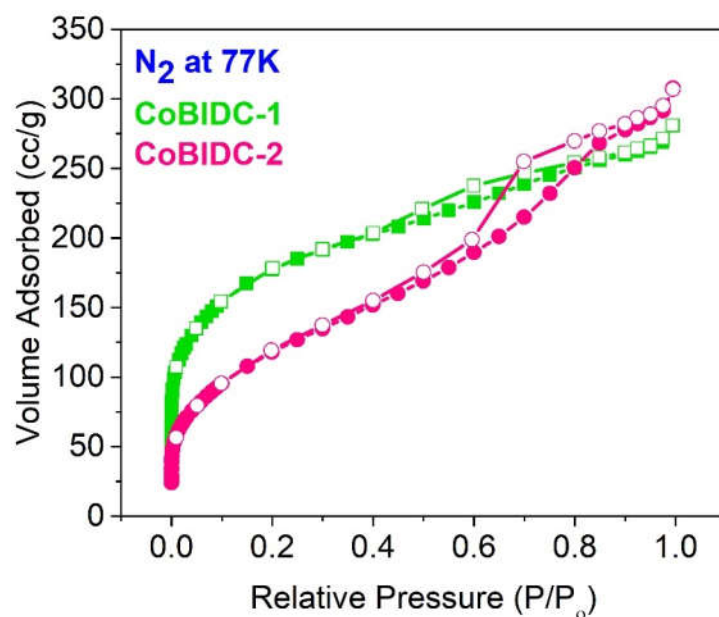
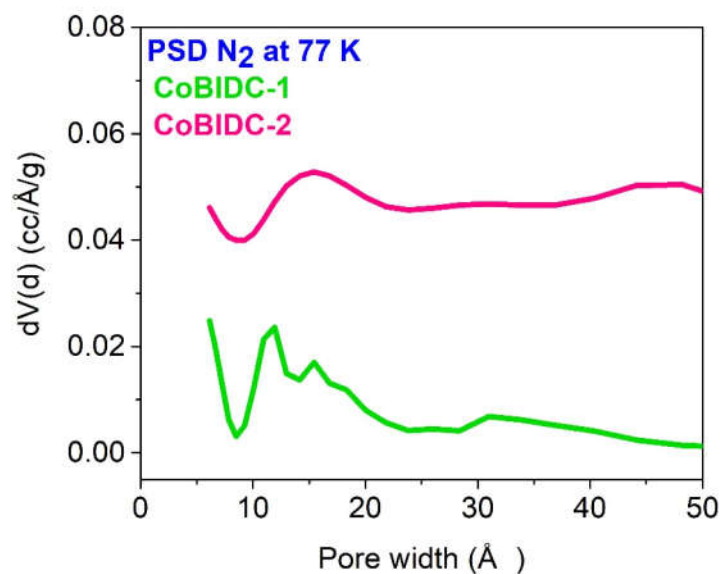**Figure 4.2:** Nitrogen isotherms at 77 K of CoBIDC–1 and CoBIDC–2 samples.

Figure 4.3: Pore size distribution (PSD) obtained from Figure 4.2 using QSDFT model. For clarity, PSD of CoBIDC–2 is offset by 0.04.

Table 4.1: Surface area and pore volume of BIDC–3–700, CoBIDC–1, and CoBIDC–2.

Samples	Surface Area[a] $(m^2\,g^{-1})$	Total Pore Volume[b] $(cm^3\,g^{-1})$	Pore Size Distribution[c] (Å)
BIDC–3– 700[12]	2530	1.89	4.7/**9.6**/19.1/25
CoBIDC–1	651	0.41	**6**/11.9/15/31
CoBIDC–2	440	0.44	6/**15.4**/30/48

[a]BET surface area. [b]Total pore volume determined from single point N_2 uptake at $P/P_o = 0.95$. [c]Pore size distribution range calculated from quenched solid-state density functional theory (QSDFT).

In order to evaluate the morphology of the BIDC–3–700, CoBIDC–1 and CoBIDC–2 samples, SEM images were collected as shown in Figure 4.3~4.5. The BIDC–3–700 showed sheet-like morphologies with diverse thicknesses and rough topography as reported earlier.[12] Since this sample was calcined at 700 ℃, so the BIDC samples structure remained fairly stable when the hydrothermal treatment was performed to grow Co_3O_4.
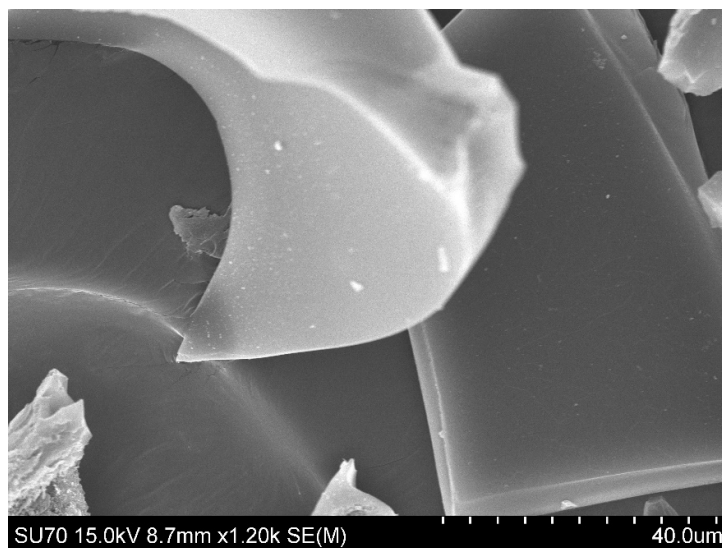

Figure 4.4: SEM image of BIDC–3–700 sample.

Both the CoBIDC samples displayed similar rough and sheet like morphologies with irregularly small particles deposited over it. In case of CoBIDC–2, there was more small clusters of Co_3O_4 than in CoBIDC–1.
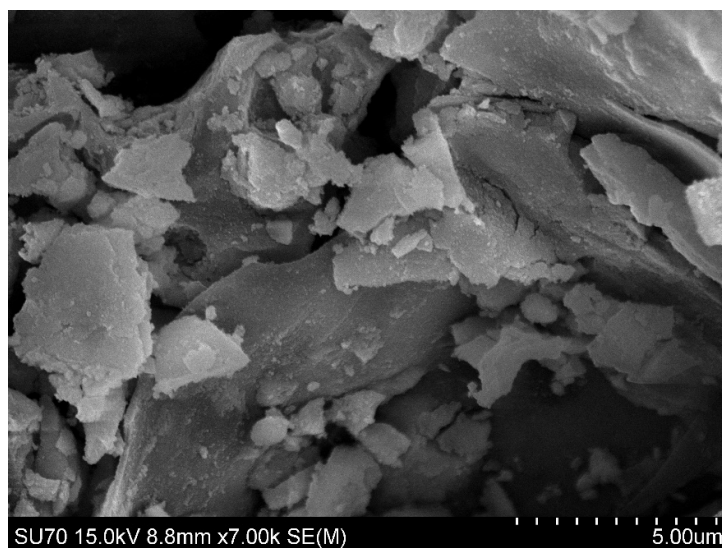

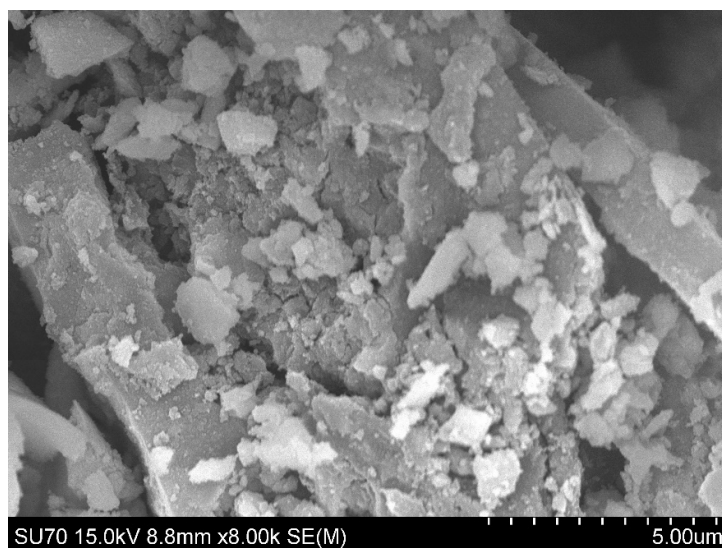**Figure 4.5:** SEM image of CoBIDC–1 sample.

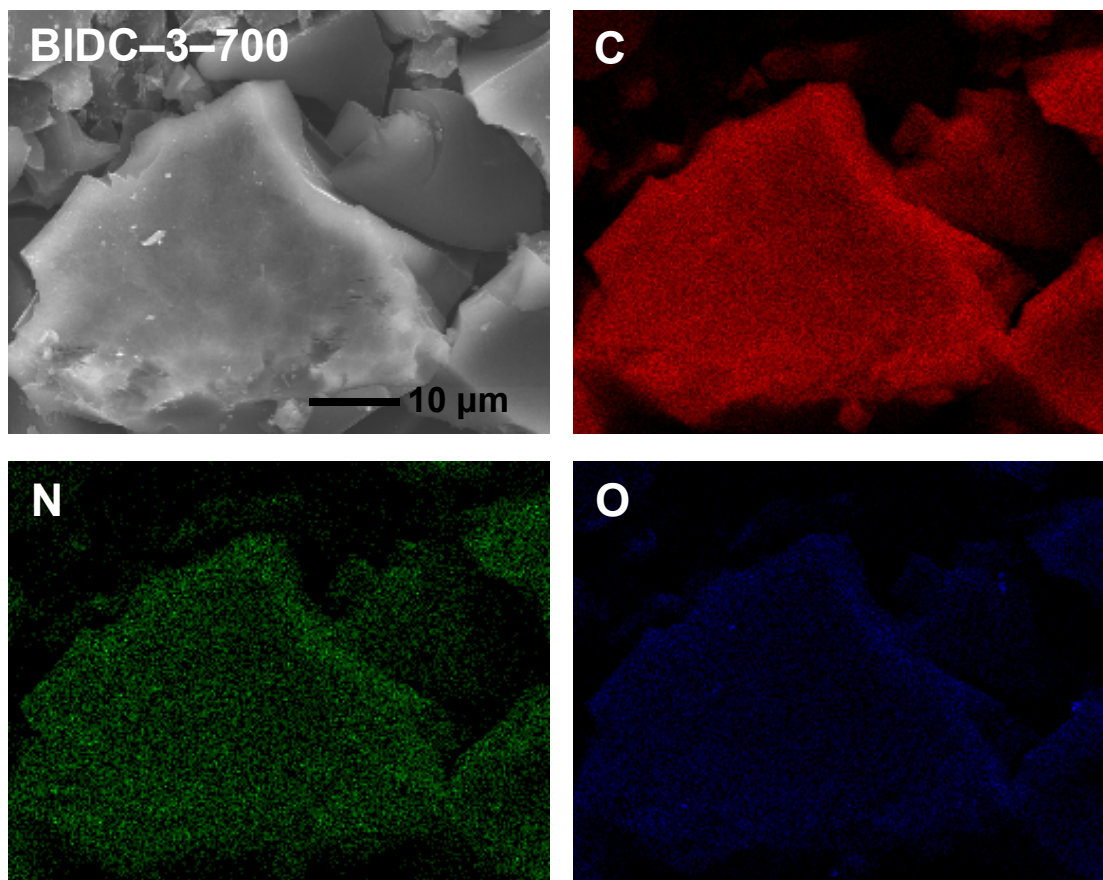**Figure 4.6:** SEM image of CoBIDC–2 sample.

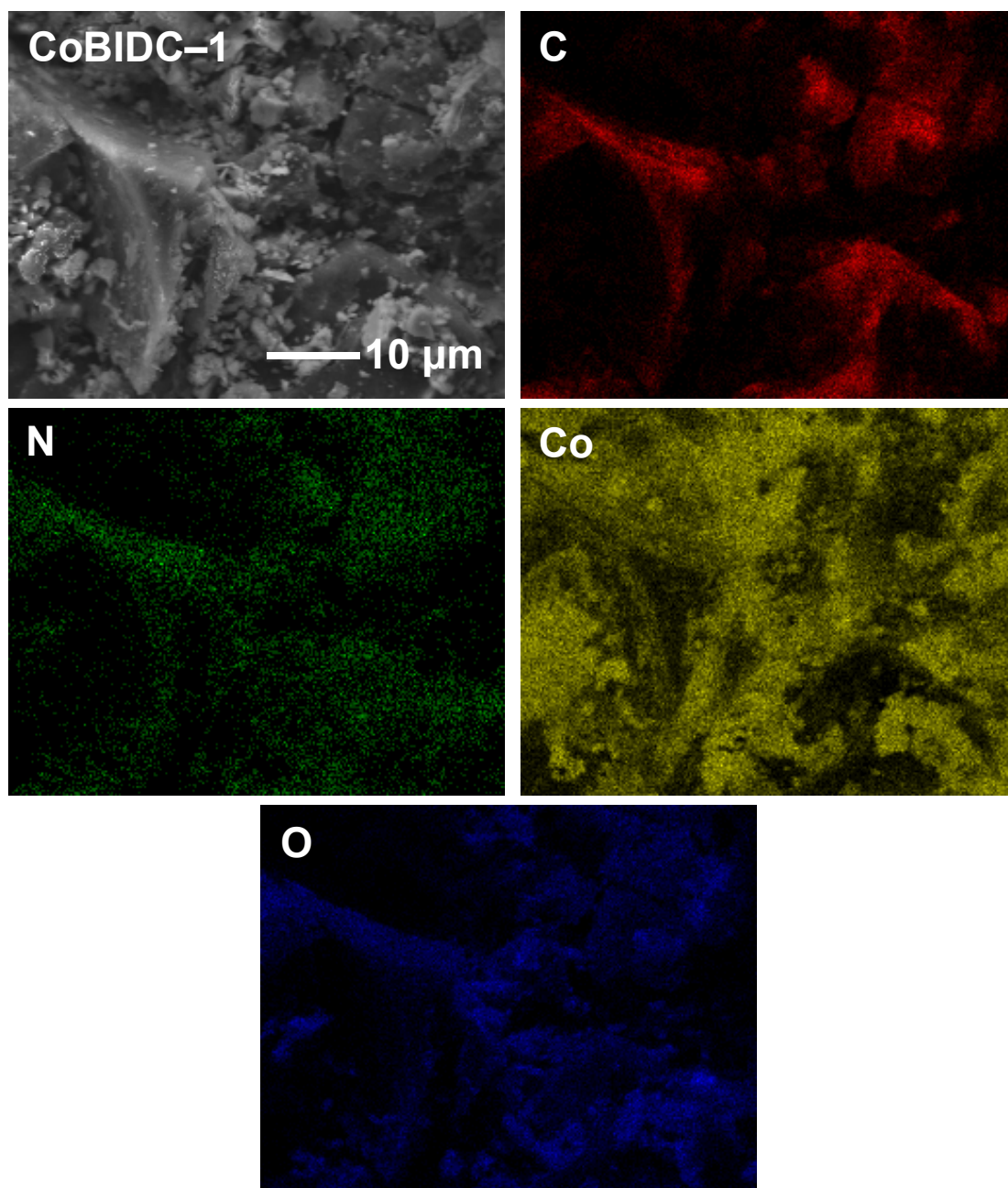**Figure 4.7:** EDX elemental mapping of BIDC–3–700 sample.

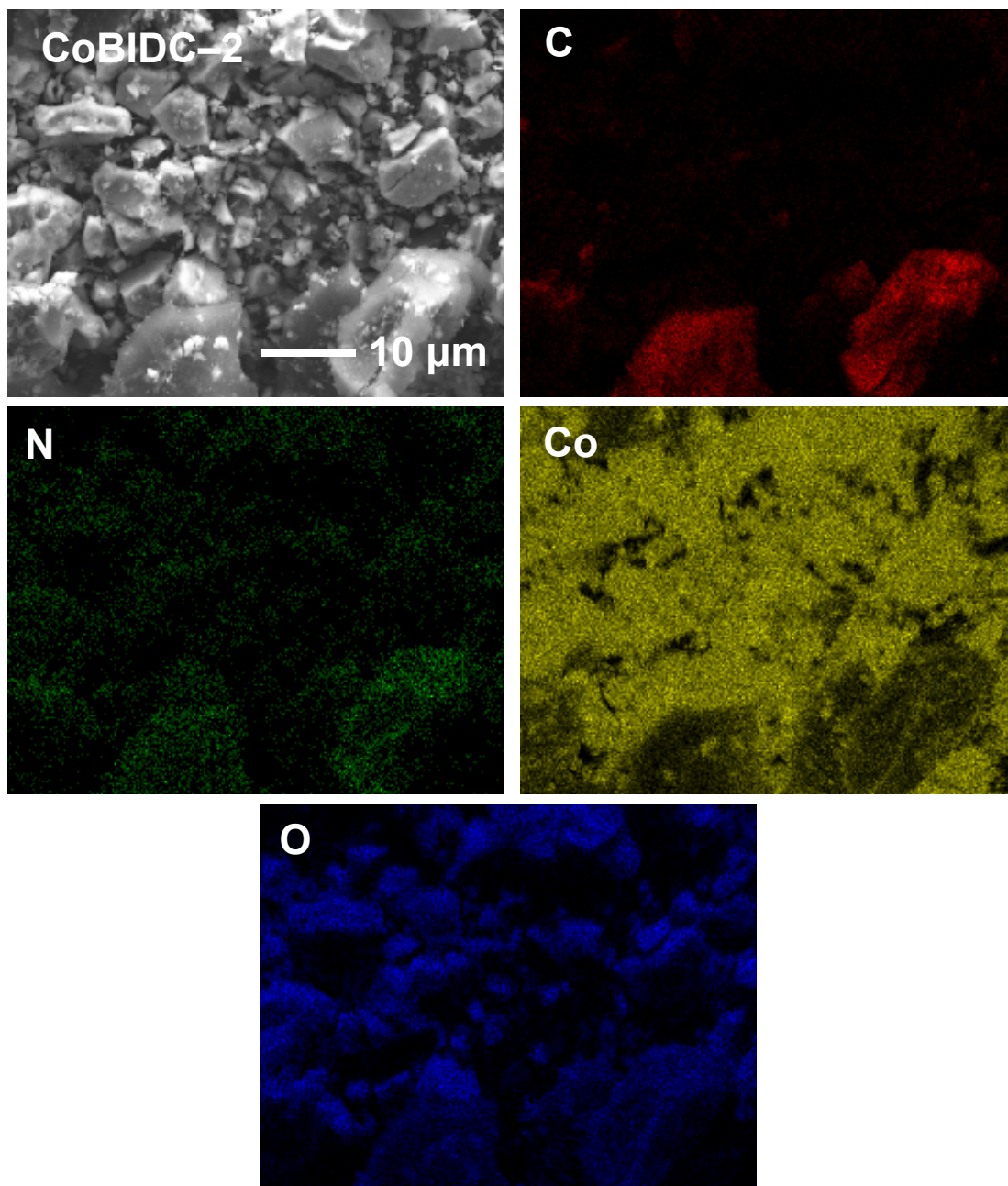**Figure 4.8:** EDX elemental mapping of CoBIDC–1 sample.

Figure 4.9: EDX elemental mapping of CoBIDC–2 sample.

TGA determined the amount of Co_3O_4 loaded on BIDC-3-700. The amount of Co_3O_4 was around 20 and 40 wt% for both CoBIDC–1 and CoBIDC–2 samples respectively.
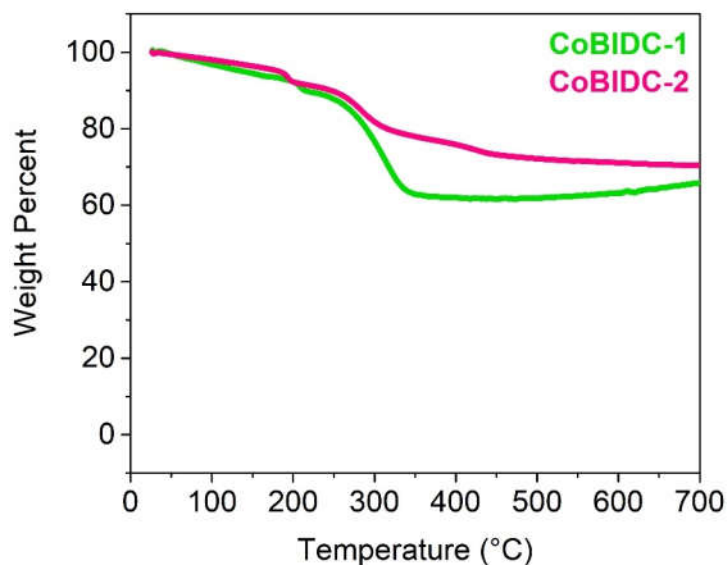

Figure 4.10: TGA of CoBIDC–1 and CoBIDC–2 samples.

The PXRD spectra confirmed that the crystals of Co_3O_4 were successfully produced on the surface of amorphous BIDC-3-700. The hkl indexes of each peak as shown in Figure 4.8 matched the one reported by Liang *et al.*[3] When XPS was performed on CoBIDC samples, the N spectrum was quite noisy which suggested that Co_3O_4 covered the surface of BIDC-3-700. When the XPS spectra of both cobalt based samples were collected, they showed similar deconvoluted XPS spectra. The deconvoluted Co 2p core spectrum in Figure 4.7 showed two strong peaks of Co $2p_{3/2}$ and Co $2p_{1/2}$ at 780.5 and 795.7 eV binding energy. These peaks are considered as the characteristic of the Co_3O_4 phase.[18]
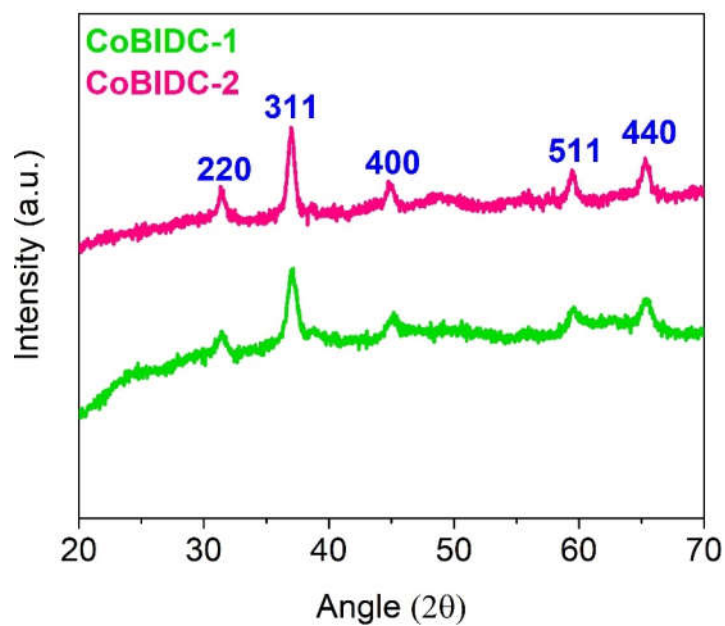
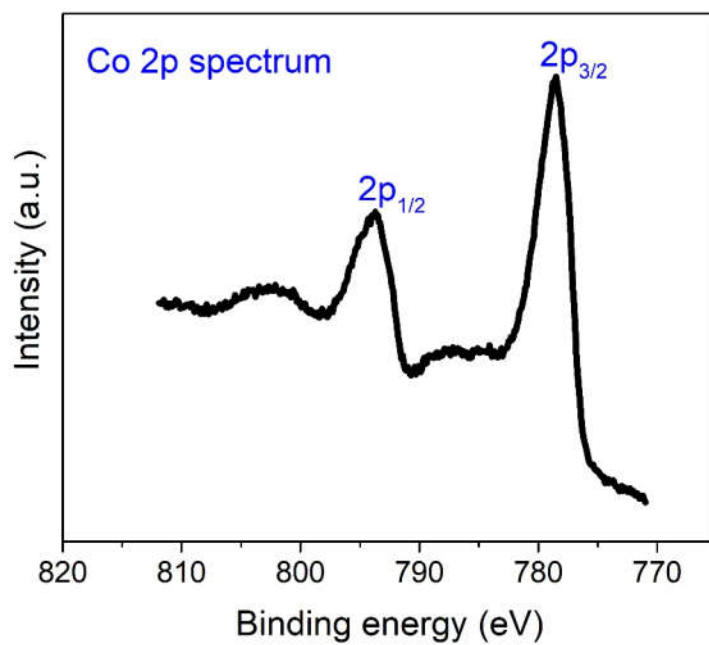**Figure 4.11:** PXRD spectra of CoBIDC–1 and CoBIDC–2 samples.

Figure 4.12: Deconvoluted cobalt XPS CoBIDC samples.

4.4.3 Electrochemical Characterization of CoBIDC samples

Cyclic voltammetry was initially used to evaluate the electrochemical performance of CoBIDC samples in ORR as shown in Figure 4.8 and 4.9. In nitrogen saturated 0.1 M KOH, the cyclic voltammograms displayed a quasi-rectangular voltammogram without any redox peak due to the typical supercapacitance effect on porous carbon materials.[19, 20] Both CoBIDC samples displayed a characteristic ORR peak centered at 0.6 V vs RHE, when the 0.1 M KOH solution was saturated with O_2. Rotating disk voltammetry was performed using RDE to illucidate the kinetics and mechanism of ORR and corresponding linear sweep voltammograms (LSVs) were collected at different rpm starting from 400 to 2500 rpm in O_2 saturated 0.1 M KOH. As the scan rate increased, the influx of oxygen molecule to the electrode surface increases due to forced convection. Due to this, a corresponding increase in the limiting current density was observed with the increase in scan rate from 400 to 2500 rpm depicted in Figure 4.11. The onset potential was observed at around 0.8 V vs RHE for CoBIDC-2 sample and the other important parameters are summarized in Table 1. The first order reaction kinetics toward the concentration of dissolved oxygen was confirmed by good linearity of the Koutecky Levich plot derived from the LSVs at a scan rate of 10 mV in O_2 saturated electrolyte.[3] The number of electrons (n) in ORR was determined from the linear sweep voltammograms obtained by RDE as 4.04 at the potential ranging from 0.2 ~ 0.6 V vs RHE. RRDE was also used to calculate the value of n illustrated in Figure 4.12 and 4.13. From RRDE, the n value was averaged to be 3.7~3.95 and the percentage peroxide species generated during the ORR remained below 20% between 0.2 to 0.8 V vs RHE. Even though the limiting current density of the synthesized CoBIDC-2 catalyst was almost half in comparison to 20 wt% Pt/C and relatively low and half wave potential, but yet this catalyst showed promising 4 electron ORR pathway selectivity.
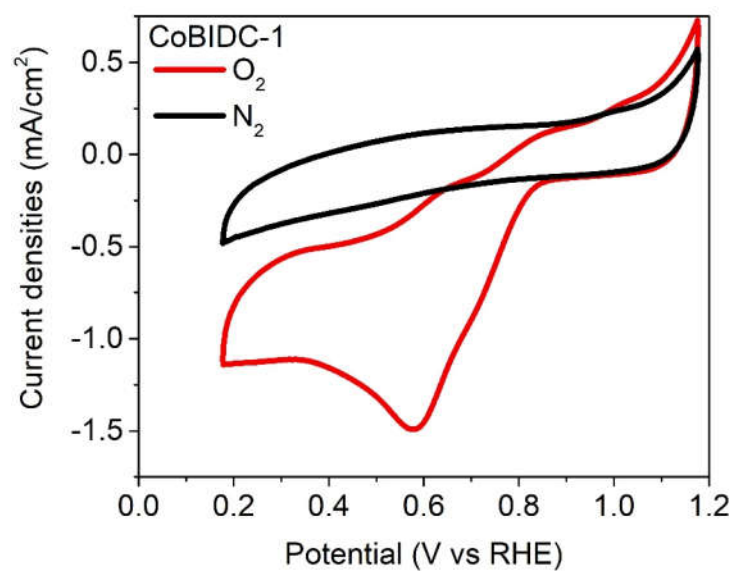
Figure 4.13: Cyclic voltammogram of CoBIDC–1 in both oxygen and nitrogen saturated 0.1 M KOH.
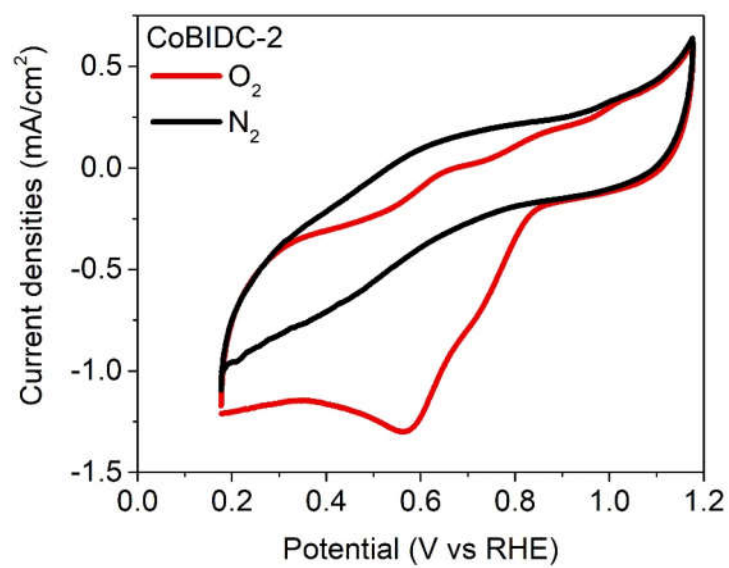

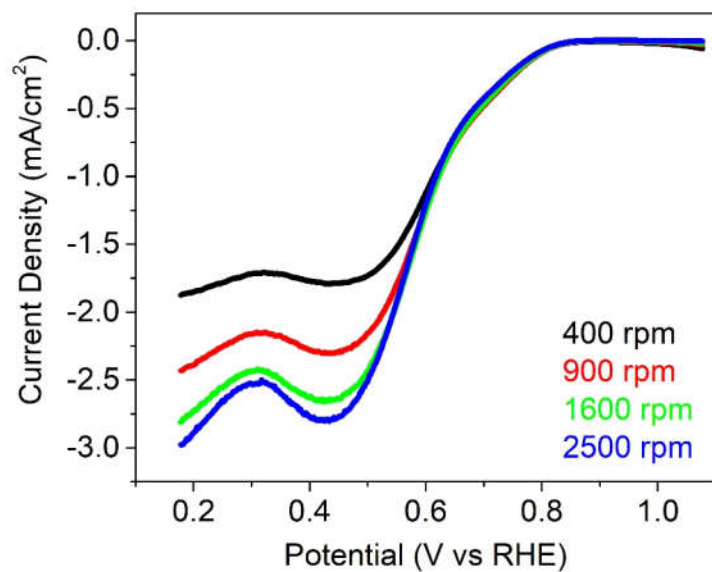**Figure 4.14:** Cyclic voltammogram of CoBIDC–2 in both oxygen and nitrogen saturated 0.1 M KOH.

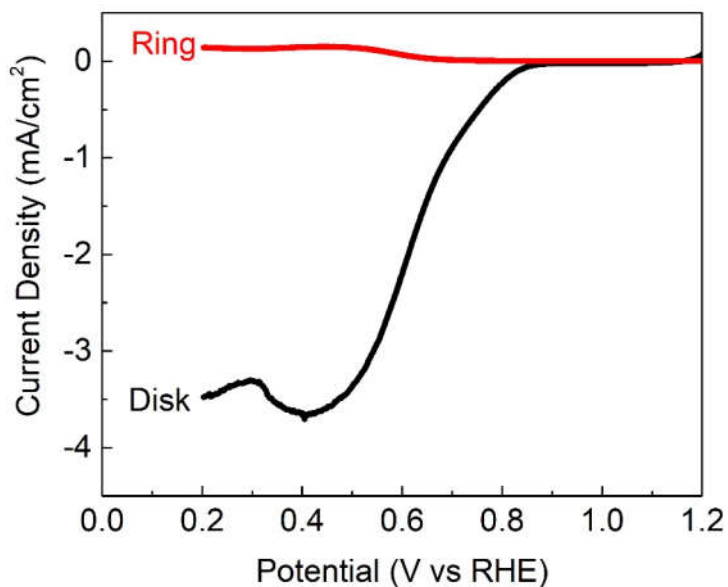**Figure 4.15:** Linear sweep voltammogram of CoBIDC–2 in oxygen saturated 0.1 M KOH.

Figure 4.16: Linear sweep voltammogram of CoBIDC–2 in oxygen saturated 0.1 M KOH obtained using RRDE.
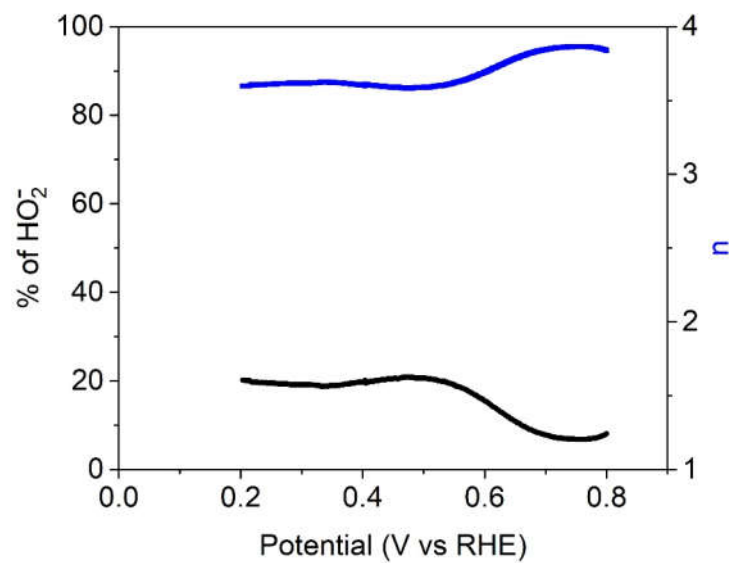
Figure 4.17: The number of electrons involve in ORR and the percentage of side product for CoBIDC–2 in oxygen saturated 0.1 M KOH calculated from Figure 4.12.

Table 4.2: The different parameters important for ORR in oxygen saturated 0.1 M KOH for all the cobalt samples in addition to BIDC-3-700 and 20 wt% Pt/C catalysts are summarized.

Samples	Onset Potential (V vs RHE)	Limiting current density (mA/cm²)	Half wave Potential (V vs RHE)	Electron Transfer number
BIDC-3-700	0.80	-1.33	0.61	2.6-3.1
CoBIDC-1	0.85	-2.24	0.57	3.45-3.50
CoBIDC-2	0.85	-2.94	0.58	4.04-4.25
20 wt% Pt/C	1.03	-5.43	0.86	3.86-4.23

Two other important parameters for ORR catalysts include poison tolerance and long-term stability. Both of these factors were evaluated by chronoamperometric i-t technique in 0.1 M KOH at 1600 rpm. Over the period of 12 hours, CoBIDC-2 catalyst displayed gradual decrease in the current. However, at the end of the amperometric experiment, it was able to show around 80% of current retention. This result suggested that the CoBIDC-2 can exhibit ORR performance for a longer time and does not undergo massive dissolution of metal oxides.

Methanol is considered as a contaminant particularly when it crosses the separatory membrane and passes from anodic chamber to cathodic chamber. As mentioned earlier, Pt or Pt/C are the most common ORR catalyst in fuel cells. However, when such fuel cross over occurs, only a minute amount of methanol can dramatically poison the Pt or Pt based catalyst. So, poison intolerance of the catalyst is an essential requirement. To study the poison tolerance of CoBIDC-2 catalyst, chronoamperometric test was done followed by an addition of 3 M methanol solution in O_2 saturated 0.1 M KOH solution. Once methanol was introduced in the solution, the current dropped rapidly but it recovered quickly showing only 11% loss in current.

Figure 4.18: The durability of CoBIDC–2 in oxygen saturated 0.1 M KOH.

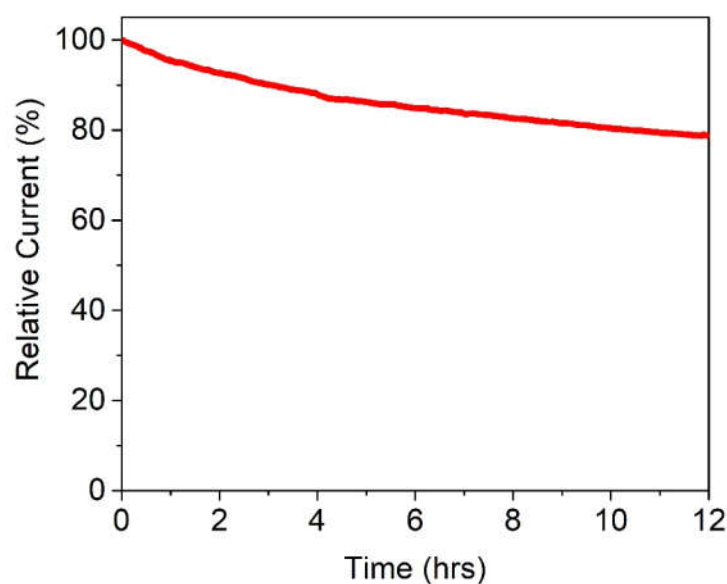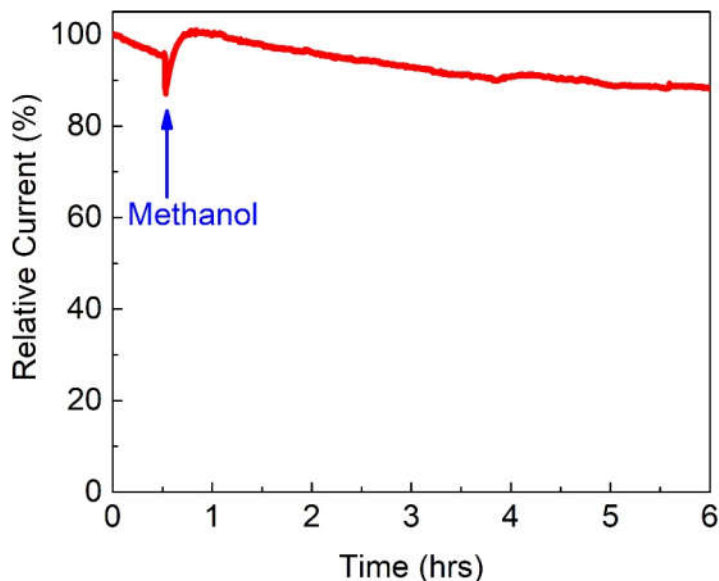**Figure 4.19:** The methanol tolerance of CoBIDC–2 in oxygen saturated 0.1 M KOH.

4.5 Conclusion

In summary, Co_3O_4 was successfully synthesized on the surface of BIDC-3-700 through hydrolysis and consequent hydrothermal treatment. The controlled nucleation and appropriate temperature during hydrothermal treatment allowed formation of covalent coupling between metal oxide and N-doped porous carbon. The fabricated catalyst showed promising ORR performance in alkaline solution. The ORR activity and selectivity of the catalyst changed significantly when Co_3O_4 was incorporated on the N doped carbon. CoBIDC-2 catalyst displayed highest onset potential and four electron ORR mechanism in comparison to BIDC-3-700 suggesting higher surface area of the catalyst is important as long as there are sufficient active sites for the substrates. Moreover, CoBIDC-2 displayed excellent durability and poison tolerance in oxygen saturated KOH solution. This overall improved performance of the CoBIDC-2 catalyst can be considered as a step towards the progress for cost-effective ORR catalyst.

4.6 References

1.   Liang, Y. Y.; Wang, H. L.; Zhou, J. G.; Li, Y. G.; Wang, J.; Regier, T.; Dai, H. J., Covalent Hybrid of Spinel Manganese-Cobalt Oxide and Graphene as Advanced Oxygen Reduction Electrocatalysts. *Journal of the American Chemical Society* **2012,** *134* (7), 3517-3523.

2.   Guo, S. J.; Zhang, S.; Wu, L. H.; Sun, S. H., Co/CoO Nanoparticles Assembled on Graphene for Electrochemical Reduction of Oxygen. *Angewandte Chemie-International Edition* **2012,** *51* (47), 11770-11773.

3.   Liang, Y. Y.; Li, Y. G.; Wang, H. L.; Zhou, J. G.; Wang, J.; Regier, T.; Dai, H. J., Co3O4 nanocrystals on graphene as a synergistic catalyst for oxygen reduction reaction. *Nature Materials* **2011,** *10* (10), 780-786.

4.   Wu, Z. S.; Yang, S. B.; Sun, Y.; Parvez, K.; Feng, X. L.; Mullen, K., 3D Nitrogen-Doped Graphene Aerogel-Supported Fe3O4 Nanoparticles as Efficient Eletrocatalysts for the Oxygen Reduction Reaction. *Journal of the American Chemical Society* **2012,** *134* (22), 9082-9085.

5.   Lin, L.; Zhu, Q.; Xu, A. W., Noble-Metal-Free Fe-N/C Catalyst for Highly Efficient Oxygen Reduction Reaction under Both Alkaline and Acidic Conditions. *Journal of the American Chemical Society* **2014,** *136* (31), 11027-11033.

6.   Gu, W. L.; Hu, L. Y.; Li, J.; Wang, E. K., Iron and nitrogen co-doped hierarchical porous graphitic carbon for a high-efficiency oxygen reduction reaction in a wide range of pH. *Journal of Materials Chemistry A* **2016,** *4* (37), 14364-14370.

7.   Yang, Z.; Yao, Z.; Li, G. F.; Fang, G. Y.; Nie, H. G.; Liu, Z.; Zhou, X. M.; Chen, X.; Huang, S. M., Sulfur-Doped Graphene as an Efficient Metal-free Cathode Catalyst for Oxygen Reduction. *Acs Nano* **2012,** *6* (1), 205-211.

8.   Wang, Y. J.; Wilkinson, D. P.; Zhang, J. J., Noncarbon Support Materials for Polymer Electrolyte Membrane Fuel Cell Electrocatalysts. *Chemical Reviews* **2011,** *111* (12), 7625-7651.

9.   Dai, H. J., Strongly coupled inorganic/nanocarbon hybrid materials for advanced electrocatalysis. *Abstracts of Papers of the American Chemical Society* **2013,** *245*.

10.   Jafri, R. I.; Rajalakshmi, N.; Ramaprabhu, S., Nitrogen doped graphene nanoplatelets as catalyst support for oxygen reduction reaction in proton exchange membrane fuel cell. *Journal of Materials Chemistry* **2010,** *20* (34), 7114-7117.

11.   Guo, S. J.; Sun, S. H., FePt Nanoparticles Assembled on Graphene as Enhanced Catalyst for Oxygen Reduction Reaction. *Journal of the American Chemical Society* **2012,** *134* (5), 2492-2495.

12.   Ashourirad, B.; Arab, P.; Islamoglu, T.; Cychosz, K. A.; Thommes, M.; El-Kaderi, H. M., A cost-effective synthesis of heteroatom-doped porous carbons as efficient CO_2 sorbents. *Journal of Materials Chemistry A* **2016,** *4* (38), 14693-14702.

13.   Wang, J. C.; Kaskel, S., KOH activation of carbon-based materials for energy storage. *Journal of Materials Chemistry* **2012,** *22* (45), 23710-23725.

14.   Lozano-Castello, D.; Calo, J. M.; Cazorla-Amoros, D.; Linares-Solano, A., Carbon activation with KOH as explored by temperature programmed techniques, and the effects of hydrogen. *Carbon* **2007,** *45* (13), 2529-2536.

15.   Abdelmoaty, Y. H.; Tessema, T. D.; Norouzi, N.; El-Kadri, O. M.; Turner, J. B. M.; E-Kaderi, H. M., Effective Approach for Increasing the Heteroatom Doping Levels of Porous Carbons for Superior CO_2 Capture and Separation Performance. *Acs Applied Materials & Interfaces* **2017,** *9* (41), 35802-35810.

16.   Dong, Y. M.; He, K.; Yin, L.; Zhang, A. M., A facile route to controlled synthesis of Co3O4 nanoparticles and their environmental catalytic properties. *Nanotechnology* **2007,** *18* (43).

17.   He, W. H.; Jiang, C. H.; Wang, J. B.; Lu, L. H., High-Rate Oxygen Electroreduction over Graphitic-N Species Exposed on 3D Hierarchically Porous Nitrogen-Doped Carbons. *Angewandte Chemie-International Edition* **2014,** *53* (36), 9503-9507.

18.   Jimenez, V. M.; Fernandez, A.; Espinos, J. P.; Gonzalezelipe, A. R., THE STATE OF THE OXYGEN AT THE SURFACE OF POLYCRYSTALLINE COBALT OXIDE. *Journal of Electron Spectroscopy and Related Phenomena* **1995,** *71* (1), 61-71.

19.   Yang, W.; Fellinger, T. P.; Antonietti, M., Efficient Metal-Free Oxygen Reduction in Alkaline Medium on High-Surface-Area Mesoporous Nitrogen-Doped Carbons Made from Ionic Liquids and Nucleobases. *Journal of the American Chemical Society* **2011,** *133* (2), 206-209.

20.   Liang, J.; Jiao, Y.; Jaroniec, M.; Qiao, S. Z., Sulfur and Nitrogen Dual-Doped Mesoporous Graphene Electrocatalyst for Oxygen Reduction with Synergistically Enhanced Performance. *Angewandte Chemie-International Edition* **2012,** *51* (46), 11496-11500.

Chapter 5

Conclusions and Outlook

In this dissertation, two novel approaches were introduced to synthesize transition metal-based heteroatom doped porous carbon from pyrolysis of nitrogen rich monomers. To optimize the physical properties of the synthesized material, various parameters such as dopant ratio, activating agent, soluble templates, calcination temperature and the precursor ratio had been studied thoroughly. The catalytic performance of the synthesized materials was investigated in oxygen reduction reactions. A set of experimental techniques such as CV, LSV with RDE and RRDE, chronomperometry were implied to get insights into the different parameters of the catalysts. A comparative study was also conducted with a commercial catalyst, Pt/C in order to assess the applicability of such materials as potential ORR catalysts.

In the first project, we reported a facile synthetic route to prepare iron-based sulfur and nitrogen dual doped porous carbon (Fe@SNDC). It was synthesized by pyrolyzing cheap, commercially available monomer i.e. benzimidazole with potassium thiocyanate. Different parameters such as calcination temperature, precursor ratio, soluble salt templates, synthesis without involving transition metal, secondary heat treatment were studied. The consequent effect on the surface area, pore size distribution, heteroatom content and nitrogen and sulfur functionalities (pyridinic, pyrrolic and graphitic) and catalytic activity led to the development of Fe based catalyst. Among the different synthesized catalysts, Fe@SNDC–1–950 displayed high surface area, optimum N content of about 5 at% and high amount of pyridinic and graphitic N along with thiophenic S. The ICP OES was used to determine the amount of iron present in the synthesized materials.

The catalytic activity of the synthesized catalyst was evaluated along with the performance of commercial catalyst i.e. 20 wt% Pt/C in similar conditions. This served as a

reference to distinguish the significance of the synthesized materials as potential ORR catalyst. Preliminary cyclic voltammetry was used to observe the characteristic peaks responsible for ORR. It provided information regarding cathodic peak potential and peak current. Since ORR is an irreversible reaction, so it was quite impossible to obtain further information from cyclic voltammogram. However, LSV from both RDE and RRDE provide more insights into the mechanisms of ORR in both alkaline and acidic medium. Based on those LSVs and Koutecky -Levich calculations, various important catalyst parameters including onset potential, half wave potential, limiting current density, number of electrons involved in ORR, percentage of byproducts formed can be obtained. Our best catalyst, Fe@SNDC–1–950 displayed an onset potential and half-wave potential of 0.98 and 0.83 V vs RHE, respectively, in 0.1 M KOH solution and enhanced ORR performance in acidic media. In addition, other important aspect of catalyst in terms poison tolerance and long-term durability was studied and compared to commercially available Pt/C (20 wt.%). Pt/C is very susceptible to methanol poisoning and also undergoes dissolution, sintering and agglomeration at fuel cell condition. However, Fe@SNDC–1–950 outperformed Pt/C catalyst by exhibiting excellent poison tolerance in case of methanol crossover and high stability in oxygen saturated alkaline electrolyte. It has been presumed that the outstanding catalytic performance of Fe@SNDC–1–950 was due to the heteroatoms (N & S) along with Fe-N moieties and the high surface area with a wide pore size distribution. The heteroatoms can tune the charge density and spin density of the material and form the active sites for ORR. The porous nature of the synthesized material can facilitate efficient mass transfer and interaction of oxygen molecule to the active sites and also efficiently remove the products formed during ORR, thus exposing the active sites for further interaction.

Another approach was used to synthesize transition metal oxides on the surface of N-doped porous carbon. Usually these metal oxides are ORR active but without any support they tend to dissolute and thereby undergo catalyst degradation. Many researchers have been

working on to develop a base which can support the metal oxides and thus, prevent catalyst degradation. So far in the literature graphene and reduced graphene oxides had been employed for such purpose. In order to improve the catalytic activity, researchers were incorporating different heteroatoms after synthesizing the oxides on graphene. Our approach was to minimize the post treatment and to grow metal oxides on already doped carbon. In this project, Co_3O_4 loaded on N doped benzimidazole derived porous carbon was prepared. As mentioned earlier, chemical activation of benzimidazole at elevated temperature led to the formation of N doped porous carbon. Co_3O_4 crystals were grown on the surface of N doped carbon via hydrolysis and hydrothermal treatment which incorporated the metal oxide with the N doped porous carbon to yield Co-BIDC samples. These Co_3O_4 samples displayed better ORR activity in comparison to only N doped carbon. Loading Co_3O_4 on the surface of the BIDC decreased the surface area of N doped carbon suggesting that higher surface area facilitate the mass transfer of reactant to the active sites, but besides increased surface area there should be enough active sites. In comparison to the commercially available Pt/C (20 wt.%), the onset potential and limiting current density of Co-BIDC was slightly lower. Despite that the selectivity of ORR mechanism in case of Co-BIDC is four electron ORR mechanism. The CoBIDC-2 catalyst was the best in comparison to the BIDC-3-700 and CoBIDC-1 samples. It also displayed excellent poison tolerance and high stability in oxygen saturated alkaline electrolyte. As a result, these materials can have a vast number of applications in different fields such as catalysts for oxygen evolution reaction, water splitting, and also as supercapacitors, electrodes in both lithium ion batteries and metal-air batteries.